2015

A Full Coverage Film Cooling Study: The Effect of an Alternating Compound Angle

Justin Hodges
University of Central Florida

A FULL COVERAGE FILM COOLING STUDY: THE EFFECT OF AN ALTERNATING COMPOUND ANGLE

by
JUSTIN HODGES
B.S. Mechanical Engineering, University of Central Florida, 2012

A thesis submitted in partial fulfillment of the requirements
for the degree of Master of Science
in the Department of Mechanical, Materials and Aerospace Engineering
in the College of Engineering and Computer Science
at the University of Central Florida
Orlando, Florida

Spring Term
2015

Major Professor: Jayanta Kapat

ABSTRACT

This thesis is an experimental and numerical full-coverage film cooling study. The objective of this work is the quantification of local heat transfer augmentation and adiabatic film cooling effectiveness for two full-coverage film cooling geometries. Experimental data was acquired with a scientific grade CCD camera, where images are taken over the heat transfer surface, which is painted with a temperature sensitive paint. The CFD component of this study served to evaluate how well the v^2-f turbulence model predicted film cooling effectiveness throughout the array, as compared with experimental data.

The two staggered arrays tested are different from one another through a compound angle shift after 12 rows of holes. The compound angle shifts from β=-45° to β=+45° at row 13. Each geometry had 22 rows of cylindrical film cooling holes with identical axial and lateral spacing (X/D=P/D=23).

Levels of laterally averaged film cooling effectiveness for the superior geometry approach 0.20, where the compound angle shift causes a decrease in film cooling effectiveness. Levels of heat transfer augmentation maintain values of nearly $h/h0$=1.2. There is no effect of compound angle shift on heat transfer augmentation observed. The CFD results are used to investigate the detrimental effect of the compound angle shift, while the SST k-ω turbulence model shows to provide the best agreement with experimental results.

For my Dad. You dedicated years of your life selflessly to show me what it means to be a man. From you, I have been afforded an amazing gift; I have become a man I am very proud to be. Any result I may produce is poorly represented without attribution to your influence in my life.

For my Mom. You have shown me the power and benefit of steadfast commitment to an idea, a set of ethics, and tireless patience. You have instilled in me a non-temporal conviction to treat others with respect, and have raised me to value a relationship with Christ.

To Jordan, Glen, Tegan, and Amy. Every friendship pales in comparison, the last 7 years describe what most would define as 'what it means to feel alive'.

ACKNOWLEDGMENTS

My sincere gratitude extends to my adviser, Dr. Jayanta Kapat. Years ago I was required to meet with a faculty member in the Engineering department, as per the curriculum, and 'happened' to meet with you. From the moment I sat in your office and listened to you talk about your lab and describe your students work, I knew I had to be a part of it. Since that hour, working in your group has been one of the best experiences I have had. I have thoroughly enjoyed the challenging moments, the rewarding moments, the friendships that have ensued, the doors that have opened for me professionally, and most certainly the struggle. Thank you for all that you have done, I look to the future with great excitement and anticipation!

I am happy to have the opportunity to thank Dr. Michael Crawford for his incredible knowledge and leadership throughout the years. It has been an absolute blessing to work with such a name. I attribute much of my professional growth to the projects we collaborated on. Also, I would like to especially thank Ken Landis, Glenn Brown, Dr. Rodriguez, and Dr. DeSilva from Siemens for the knowledge I have received, by virtue of our work together!

I would also like to greatly thank Dr. Ali Gordon and Dr. Subith Vasu for being on my thesis committee. I sincerely appreciate your guidance through this process.

I must also strongly thank Greg Natsui for his outstanding leadership as my direct mentor over the past few years. We have spent countless hours working together, and I am very lucky to have had such great development professionally, intellectually, and as a

person because of you. Some of the best moments of understanding were with you, a textbook, some scratch paper and a felt pen, and MATLAB.

Thank you Mark Ricklick for the most embarrassing, humiliating, and character building moment in my professional career, as you grilled me for about 15 minutes straight in front of everybody at the lab, just after I started working there. That moment was quite a turning point for my professional attitude, as I have never been so strict on myself for understanding fundamentals and holding myself to a higher standard. I am genuinely grateful for that moment and our friendship. Also, thank you for being so awful at fishing that I get the chance to teach you and hold countless discussions with you on how to not be so awful at fishing.

To the world's best lab mates - Matt Golsen, Roberto, Anthony Bravato, Lucky, Patrick, Jahed (you can do anything), Brandon, Malay (GW2 champion), Constantine, Josh Schmitt, Josh Bernstein, Sri, Barkin (worst soccer player of all time), Marcel, Dr. Wang, Lumaya, Marc Medina (forever weak), Lauren, Chris V, Rachel, Perry, Christian Garrett (best work study student of all time), Joe, Craig, Daniel Gonzalez, Ahmed, Sergio, Bryan Bernier, Luke, John Harrington, and many others. You all made it very easy to spend so much time in a LABORatory!

I am also very thankful to work with Tyler Voet and Stephen Stafstrom. Two great jedi padawan learners who make work less stressful and even more fulfilling.

I have made a lot of great friendships through work in the past few years, but I would like to particularly show appreciation for the friendship and collaborative work

Zach Little and I have experienced. I really appreciate all the support from you, you are a great friend and colleague!

A big thanks belongs to Cassandra Carpenter for also being an amazing mentor. Your kindness, knowledge, guidance, and enthusiasm did/does not go unappreciated. You are an ideal breed for working with and managing people, and also a great friend. I hold great value in my newly found love for CFD, and I cannot go without thanking you for everything you have taught me while starting out.

TABLE OF CONTENTS

LIST OF FIGURES

LIST OF TABLES

LIST OF EQUATIONS

NOMENCLATURE

Symbols

A_c	Cross-sectional area
A_s	Surface area
D	Hole diameter
DR	Density ratio; $DR = \rho_c/\rho_\infty = T_\infty/T_c$ $(for\ two\ similar\ ideal\ gases)$
$EBKE$	Elliptic Blending k-ε turbulence model
h_u	Uncorrected heat transfer coefficient
h_f	Corrected heat transfer coefficient (corrected for film temperature)
h_0	Heat transfer coefficient without blowing
i	Current
I	Momentum flux ratio; $I = (\rho u^2)_c/(\rho u^2)_\infty = M^2/DR$
k	Thermal conductivity
k_f	Thermal conductivity of air
L	Hole axis length
M	Blowing ratio; $M = (\rho u)_c/(\rho u)_\infty$
Nu_x	Nusselt number; $Nu_x = h_0 x/k_f$
N_x	Number of streamwise rows
N_z	Number of spanwise holes
P	Lateral pitch between holes, measured exit breakout to adjacent exit breakout
Pr	Prandtl number
q''_f	Heat flux in the presence of film cooling
q''_{conv}	Heat flux loss by convection
q''_{cond}	Heat flux loss by conduction
q''_{rad}	Heat flux loss by radiation
q''_{gen}	Heat flux generated by joule heating
R	Resistance
Re	Film cooling Reynolds number; $Re = U_\infty D/\nu$
Re_x	Reynolds number based on x; $Re = U_\infty x/\nu$
s	Equivalent slot width; $s = \pi D/4(P/D)$
SST	Menter's Shear Stress Transport turbulence model
t	Thickness
T	Temperature
T_{aw}	Adiabatic wall temperature
T_b	Backside temperature driving conduction
T_c	Coolant temperature
T_{ref}	Temperature of reference picture
T_w	Wall temperature
T_∞	Freestream temperature
TI	Turbulence intensity; TI=u'2rms/U
$u[\ ]$	Total uncertainty of [ ]
u, v, w	Corresponding stream, wall normal, and lateral velocities
U	Velocity magnitude
U_∞	Freestream velocity magnitude
$V2f$	The V2-f turbulence model, an extension of the standard k-ε model

x, y, z	Stream, wall normal, lateral (spanwise)
X	Streamwise pitch, measured exit breakout to projected exit breakout
y^+	Inner scaled wall normal coordinate;$y^+ = \left(y\sqrt{\tau_0/\rho}\right)/\nu$

Greek

α	Inclination angle
β	Compound angle
η	Adiabatic film cooling effectiveness; $\eta = (T_\infty - T_{aw})/(T_\infty - T_c)$
θ	Non-dimensional temperature between coolant, freestream and heater
ξ_i	Unheated starting length distance 'i' for calculation of h_0
ρ_{el}	Electrical resistivity
ρ_c	Coolant density
ρ_∞	Freestream density
σ	Stephan Boltzmann constant

Acronyms

CATER	Center for Advanced Turbines and Energy Research
CFD	Computational fluid dynamics
CCD	Charged coupled device
CTA	Constant temperature anemometer (hot-wire)
FCFC	Full coverage film cooling (followed by; I – FY2010, II – FY2011)
FPG	Favorable pressure gradient
IR	Infrared
RANS	Reynolds Averaged Navier Stokes
RR	Recovery region
TKE	Turbulent kinetic energy
TSP	Temperature sensitive paint

CHAPTER 1: INTRODUCTION AND LITERATURE REVIEW

1.1 The Motivation to Study Gas Turbines

Gas turbine technology is widely used throughout many applications, most notably in land based power generation, aviation, and marine applications. The design of gas turbines represents one of the most exciting and challenging problems of the current age, utilizing experts of many disciplines. Research in gas turbine systems is driven by their economic and environmental impact, these machines which produce over 90% of the world's power and propel near 100% of commercial aviation [1]. Even though completely renewable energy has been given significant attention in recent years, gas turbines fired from coal and natural gas will continue to produce the majority of the world's power into the foreseeable future. This suggests that a natural step towards efficiently utilizing our natural resources is improving gas turbine technology, both for land based power generation and aviation. Such statements warrant the need for study and motivation to study.

1.2 Basis of Gas Turbine Operation

The basis of a gas turbine is to provide a thermodynamic system which results in a positive of transfer of work using air and fuel mixtures for combustion. This positive work transfer is used in combination with generators for generating electricity, then distributed to the where the needs exists within the electrical grid network (e.g. houses, buildings, etc.). The main components in a general, basic (open) gas turbine are a compressor, combustor, and turbine. Work input is required by the compressor, as ambient air enters the gas turbine system through the compressor. After carefully compressed, the air is introduced into combustion chambers with a foreign species (fuel) for combustion. Upon combustion, the air-fuel mixture has a significant increase in temperature and

volume per unit mass, where it then enters and expands throughout the turbine section. This expansion process through the turbine is the process by which the fluid does work on the turbine blades, thus creating a positive transfer of work. Resources (e.g. work input to compressor, fuel, etc.) are successfully leveraged when the work provided through the turbine section exceeds the work required to elsewhere in the gas turbine configuration.

This process describing gas turbine operation is known as the Brayton cycle. The ideal Brayton cycle consists of: 1. isentropic compression, 2. isobaric heat addition, 3. isentropic expansion, and 4. isobaric heat extraction.

An increase in thermodynamic efficiency of the engine is dominated by engine pressure ratio and increasing the firing temperature. It is the goal of gas turbine heat transfer research to enable this firing temperature to rise even higher than the already greater than melting temperature of the gas turbine components, such that higher efficiencies can be achieved. This is a multi-discipline effort however, where many groups of experts are working to safely increase turbine firing temperatures with different technologies; new material technologies which better protect turbine walls/blades (e.g. thermal barrier coatings), various internal cooling techniques throughout turbine blade passages (e.g. impingement cooling), and several external cooling techniques over the blades (e.g. film cooling), to name a few.

1.3 Gas Turbine Cooling and Heat Transfer

As described previously, there is a clear need to increase firing temperatures in gas turbines such that higher efficiencies can be achieved, and thus human resources can be spent slower at more sustainable rates. As a result, the effort to increase firing temperatures in gas turbines is relentless and ever-growing.

Earlier in the 20th century, gas turbine technology was such that operation could presume without the dedicated, elegant cooling systems that exist today. At that time, the capabilities in high firing temperatures were lacking such that the alloys used in combustor and turbine sections could withstand thermal loads driven by the hot gas path. Given the multidisciplinary effort of increasing gas turbine efficiency, and thus increasing combustion and hot gas path temperatures, eventually more advanced and dedicated cooling systems (in cooperation with metallurgical advances) were required to maintain the integrity of the components within gas turbines.

Several popular cooling schemes are used for protecting critical regions subject to high temperatures; turbine blades, vanes, end walls, shroud, etc. [2].

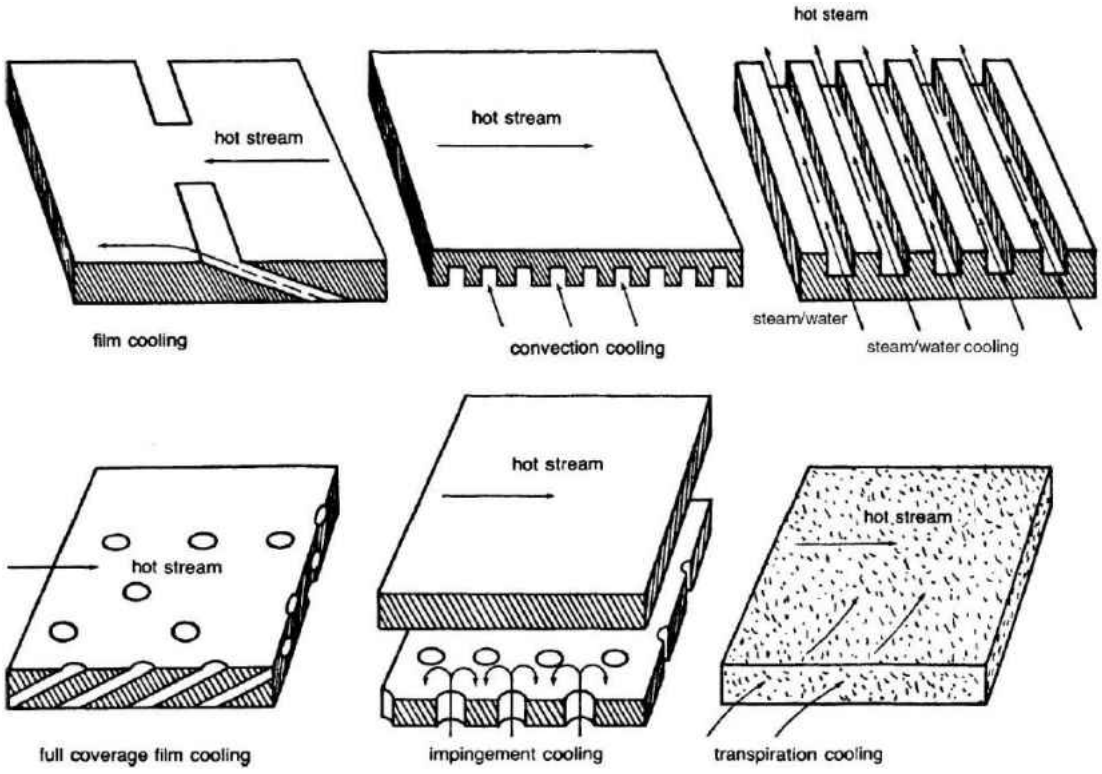

Figure 1: Various popular cooling schemes in gas turbines [2]

1.3.1 Convective Cooling

Until the late 1960's, one of the most popular and few cooling systems in place for gas turbines was convective cooling systems [2]. Convective cooling is still in place and vital in modern gas turbine designs. The basis of convective cooling is that air is bled from the compressor section, and forced into spaces within blades and/or vanes. While this air from the compressor section is still hot relative to ambient conditions, it is still relatively cold compared to the hot gas path. To maximize the convective cooling, it is needed to design the internal cavities in the blades/vanes in such a way that maximizes heat transfer from this cool air to the hot metal alloy within the blade/vane. Such a situation yields an intuitive solution: to increase the convective heat transfer one can increase the cooled area. To serve this purpose, narrow and winding passages (i.e. serpentine passages) are created within the blades to allow for a larger area being cooled, increasing the heat transfer from the cool air to the blades. To further increase heat transfer from the cool air to the metal allow in the internal blade passages, designs have utilized features within the internal serpentine passages which 'trip' or disturb the flow such that the heat transfer coefficient is further increased.

1.3.2 Impingement Cooling

Impingement cooling is used to cool several sections in gas turbine engines, such as the walls in the combustion section, the case and lining throughout the turbine section, with special attention to cooling the turbine blades subject to critically high temperatures [3]. Air is bled from the compressor section and fed to the turbine and combustor for impingement cooling, its high source pressure and relatively cool temperature makes it useful for this application. Impingement cooling occurs within the blades when the coolant is forced through the internal blade wall, where the flow thereafter impinges on the outside walls of the blade. Impinging jets are used typically in arrays, in order to cover large surfaces, usually to cool mid chord areas within turbine blades.

Impingement cooling is not capable of cooling the external surfaces of turbine blades, as film cooling does, which provides an immediate buffer of protection against hot gas path thermal loads.

1.3.3 Film Cooling

Goldstein defines film cooling as the introduction of a secondary fluid (coolant or injected fluid) at one or more discrete locations along a surface exposed to a high temperature environment to protect that surface not only in the immediate region of injection but also in the downstream region [4]. In the last three decades, film cooling has received a large amount of attention in research and industrial application, due to its complexity and usefulness. Well over 2,000 publications have been made on film cooling since its inception.

The film injected for cooling acts as an enthalpy sink to the hot main-flow and reduces the temperature potential driving heat into the part, thereby reducing the heat flux into the blade and maintaining the blade surface at safe operating temperatures. In the near wake of a film cooling jet, there is a separation region which is a factory of turbulent kinetic energy. In gas turbines the main stream is already highly turbulent. The challenge is to predict the interaction of a stream jetting into a turbulent boundary layer and generating more turbulence. One thing that is needed to better understand the complex nature of film cooling is more insight into the role of turbulence. Pietrzyk [5] insists the fundamental limitation to improving film cooling performance is a lack of understanding of the fluid mechanisms (and turbulence) governing the flow. This issue remains, as Kohli [6] asserts additionally that our current knowledge still lacks a fundamental understanding of the mechanisms governing transport of heat and momentum. The complexity of film cooling is well agreed accepted, thus warranting the need for study.

This study is on a full coverage film cooling array, which will be defined in later sections of this report. This introductory and literature review chapter will be structured such that different aspects of film cooling will be discussed and compared with literature explicitly. Such upcoming sections introducing concepts and reviewing literature are:

- Geometric Parameters Influencing Film Cooling
- Independent Parameters Used in Film Cooling
- Full Coverage Film Cooling

1.4 Film Cooling Basics and Literature Review

1.4.1 Geometric Parameters Influencing Film Cooling

Before considering parameters specific to different test cases of the same geometric configuration, such as those parameters which may describe the thermal state or flow field in a film cooling study, let the discussion focus on geometric parameters which influence film cooling.

It is very common in film cooling studies published in literature to nondimensionalize the testing parameters which describe the study performed. Such scaling allows for comparison of a real design used in industrial application to a study performed elsewhere (e.g. a research lab) on a smaller scale. It is not feasible that a group creating a film cooling design for industrial application would find studies in literature conducted for their exact geometries and testing conditions (e.g. hole diameters used, Reynolds number present, etc.). Therefore, this nondimensionlization of testing parameters allows for greater sharing of knowledge attained through study to those surveying literature.

The first important geometric parameter to discuss is hole diameter, D. One popular metric to scale an experimental study by is the metering hole diameter, D. The word metering refers to the round hole diameter of a film cooling hole, prior to any cross sectional area change

(e.g. a diffuser, a trench, a conical section, etc.). This is a popular parameter to use in CFD for the relevant length scale of the flow field surrounding the film cooling holes.

Another important geometric parameter is hole length, L. The total hole length, L, is described as the distance along the film cooling axis from the inlet hole area (plenum side) to the exit hole area (hot gas path, or primary flow side). Shaped film cooling holes are not pertinent in this study; therefore all geometrical considerations for shaped holes will not be included in this work.

One large motivation to consider the length of a film cooling hole (i.e. in L/D) is the impact such length has on the sensitivity of the flow field at the exit of the film cooling to the entrance effects presents. More specifically, a longer hole length will cause any flow disturbances at the entrance (plenum side) of the film hole to dampen out by the exit of the film hole. Such disturbances can be things such as the vena-contracta effect, imperfections in the hole geometry due to machining, blockages near the film hole entrance, etc. Motivation for study of the film hole length is also helpful when considering the specified wall thickness in a design application, through which the film holes will be machined. Also, the momentum of the coolant jet leaving the film is hole is dependent on the length of the hole (i.e. wetted area and friction).

Burd [6] performed a study investigating how different hole lengths and plenum configurations influenced the flow field throughout and leaving a film hole. The main results of the study are energy content of the flow (through spectral distributions presented), dominant frequencies present in the exit plane of the film holes, dissipation frequency bandwidths of the flow, and length scale calculations for different L/D ratios. A major conclusion for this work was that the length scales calculated were only marginally affected by the variation in L/D ($2.3 < L/D < 7.0$). Also, in general, the longer L/D cases exhibited smoother spectra data, where the short holes had more pronounced peaks corresponding to energy carried in the flow at certain wavelengths.

A very large number of studies in film cooling literature involve variations of L/D in their test matrix. Harrington [7] for example, conducts a study with short injection holes (both an experimental and CFD study), showing how short injection lengths affect correlations (e.g. Sellers superposition) agreement with data, how mainstream turbulence content interacts with the near hole flow field, and other characterizations of heat transfer throughout the film cooled surface. There are a large range of topics investigated in said literature, thus, all of which will not be included here for discussion on the impact of the L/D chosen for a film cooling design. It is also common to include some L/D analysis in many CFD film cooling studies, as such data is already available in the flow field solution. Examples of flow fields investigated with varying L/D include (extremely incomplete, just examples); Leylek [8, 11], and Thole [9].

The next geometric parameter to discuss is the inclination angle. This is the angle that is also referred to as surface angle, where the angle that the axis of the film cooling hole makes with the heat transfer surface is defined as the inclination angle. An inclination angle of 90° corresponds to a film cooling hole that is injecting perpendicular to plane of the heat transfer surface, and an inclination angle of 0° corresponds to the theoretical case of the hole axis being in-line (parallel) to the heat transfer surface. Much of the research community's intent to studying the inclination angle is for determining the tendency of a film cooling hole to produce a film jet that may or may not be attached (or covering) the heat transfer surface, based on the inclination angle. This corresponds to the principle of 'jet lift off', where a film cooling jet may pass through the coolant hole and be discharged into the primary flow (hot gas path) without ever touching the heat transfer surface. It is important in most design situations to avoid this result, as no additional protection is offered by this injected film, yielding a waste of coolant routed from the compressor to the turbine section for cooling.

Common inclination angles documented in literature typically range between 25° - 90°. Some studies, as in Metzger [10], generate comparisons of angled vs. normal injection, but most studies focus solely on injection cases with an acute inclination angle. Although documenting shaped film cooling holes, Bunker [12] presents a technology review on shaped film cooling hole studies. Bunker's [12] review finds its place in this work (pertaining to cylindrical holes only) by documenting popular shaped geometries (i.e. their inclination angles). Most of the shaped geometries in this review have more significant lateral diffusion than wall normal diffusion. Therefore, crudely, one can consider the shaped hole inclination angles as 'upper bounds' on prospective inclination angles to be used. This is justified given that any wall normal diffusion (through the use of trenches or diffusion in the shaped geometries) will provide better coverage and less jet lift off than in the cylindrical hole case at the same inclination angle. That being said, Table 1 shows inclination angles presented in the technology review.

Table 1: Inclination angles used in studies compiled in Bunker's [12] review

α	Occurances in Bunker [10]
30	12
35	10
45	2
50	2
55	1

The next geometric parameter to discuss is the compound angle. This last geometric parameter needed to fully define a single cylindrical hole, the compound angle, is defined as the angle the hole axis makes (projected onto the heat transfer surface) with the mean flow direction (primary flow, or hot gas path). For this reason, the compound angle is commonly known as the flow angle. Introducing a compound angle causes augmented spreading of the jet laterally, and significantly changes the local flow field. This deviation from in-line injection causes further

induced turbulence, causing an immediately larger buffer of film. Also, it is seen that the traditional (symmetric) counter rotating vortex pairs present in jet in crossflow (JICF) situations becomes highly asymmetric when a compound angle shift is used.

Certain attributes to the flow field are distinct once a compound angle shift is implemented. Leylek [13] provides a novel computational technique documented and evaluated for film cooling holes over a range of compound angles. Velocity contours are shown in a plane through the center axis of the film cooling hole, as well as in the exit plane of the film cooling hole. Contours of turbulence intensity just above (Y/D~.2) are documented for each compound angle tested. With coefficients of pressure distribution over the surface near injection, this publication provides good physical insight into the change in flow field with respect to different compound angles.

An experimental study displaying the consequence of introducing a compound angle, in terms of resulting flow field, is provided by Lee [14]. This study utilizes heat transfer measurements and flow visualization techniques to characterization the flow field around compounded hole configurations. This can be compared to the flow field resulting from inline injection. From the flow visualization results, it is clear that the compound angle contributes to when the hot gas path (primary flow) is ingested into the film cooling hole (secondary flow). More discussion will follow later on the results expected from introducing a compound angle shift.

Figure 2 shows the sign convention and description for inclination and compound angle.

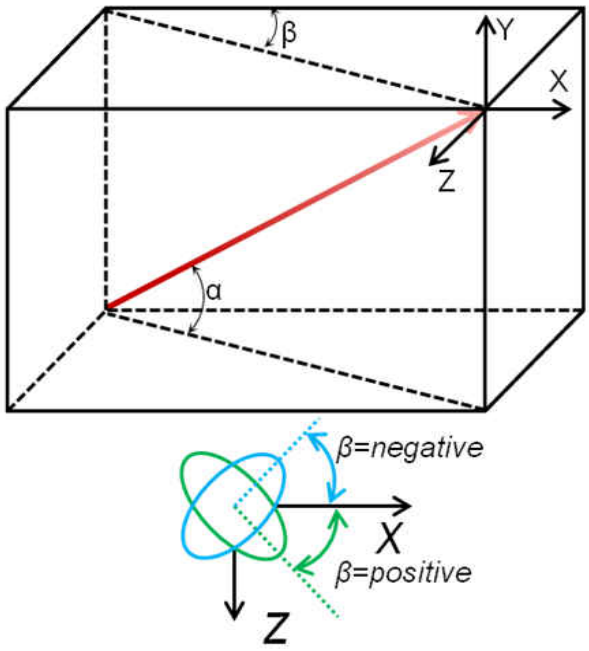

Figure 2: Description of inclination and compound angle with sign convention

Two geometric parameters are discussed here to describe the spacing of film holes within a large array or grid of film holes. The lateral (or transverse) spacing between holes is called the lateral pitch, P. The streamwise (or axial) spacing is known as the streamwise pitch, X. Each spacing is measured from the center of one hole exit area (breakout) to another, whether lateral or streamwise. Both spacing's are traditionally nondimensionalized by hole diameter, such that comparisons can be made between studies with differing hole diameters. Figure 3 below shows a description of the lateral and transverse spacing's described.

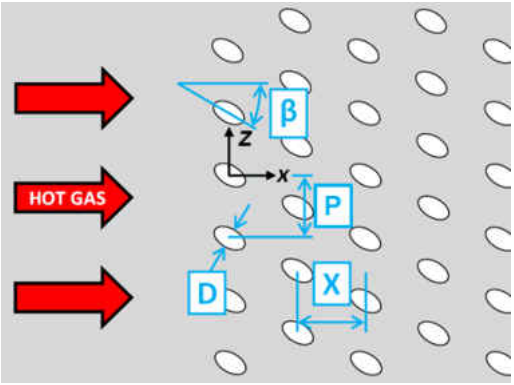

Figure 3: Description of lateral pitch (P) and streamwise pitch (X)

1.4.2 Independent Parameters Used in Film Cooling

The first film cooling parameter to discuss is the density ratio. The term density ratio signifies the ratio of the secondary flow (coolant) density to that of the primary flow (crossflow), as in Equation 1 . Typically laboratory film cooling studies utilize heated coolant due to convenience of test setup. Such an action results in an inverted density ratio, where it is common that these studies have a density ratio of less than unity. Although this is opposite from the situation found industrial application, this is a common practice in the experimental research setting. This study uses heated air as the secondary fluid, maintaining an approximate density ratio of 0.8. One noteworthy precaution to take with using air as both the primary and secondary fluid while heating the secondary flow is that conduction effects on the heat transfer surface become significant. Wright et al. [15] investigates this occurrence with several different measurement techniques, the result being that PSP is the favorable technique to avoid conducting on the heat transfer surface. To minimize this effect, this study utilizes a very low thermal conductivity material as the heat transfer surface. The characteristics of which will be documented later in this report.

Equation 1: Density Ratio

$$DR = \frac{\rho_c}{\rho_\infty} = \frac{T_\infty}{T_c} \quad (1)$$

The next film cooling parameter to discuss is the blowing ratio. The term blowing ratio signifies the ratio of the secondary flow (coolant) mass flux to the primary flow (crossflow) mass flux, as in Equation 2 . This term accounts for the amount of coolant mass injected for cooling the heat transfer surface, relative to the mainstream flow (or hot gas path). This term involves the relative densities of the fluids, as well as the relative velocities of the fluid streams. Velocity ratio is another common scaling factor used in film cooling, which is absorbed in the blowing ratio for this study.

Equation 2: Blowing Ratio

$$M = \frac{(\rho U)_c}{(\rho U)_\infty} \quad (2)$$

The next film cooling parameter to discuss is the momentum flux ratio. The term momentum flux ratio signifies the ratio of the secondary flow (coolant) momentum flux to the primary flow (crossflow) momentum flux, as in Equation 3. The momentum flux ratio can be determined with knowledge of the density ratio and mass flux ratio. For a given laboratory test at a specified M, the DR dictates the momentum flux ratio of the film cooling jet. The momentum flux ratio is pivotal to the fluid mechanics of the coolant jet, as an increase in momentum yields a tendency for the jet to protrude through the boundary layer on the heat transfer surface, and into the mainstream of the primary flow. This condition of 'jet lift off' is often kept in mind when performing film cooling studies, as jet lift off causes a very poor outcome in film cooling effectiveness over the surface. A non-specific, general case of jet lift off is pictured in Figure 4, to show the different behaviors of film cooling jets in regards to momentum flux ratios.

Goldstein [16] asserts different characteristics of each momentum flux ratio regime. In the first regime, for low momentum flux ratios, Goldstein states that the film cooling effectiveness is increased with increases in coolant mass added. At this point, the thermal inertia of the coolant is utilized fully, and because the film is so attached to the heat transfer surface, the film cooling performance is not regarded to the density ratio of the fluid streams. After an increase in momentum flux ratio up to a sufficiently high amount, the film cooling effectiveness now depends on the flow properties present (e.g. DR, M, etc.). This regime is described as the mixing regime, and the flow structures / jet lift off now play a more significant role in the effectiveness resulting. Lastly, Goldstein asserts a regime characterized by clear lift off of the coolant jet, off of the heat transfer surface. This regime has complex turbulent structures present, as the turbulent jet penetrates into the turbulent mainstream.

Equation 3: Momentum Flux Ratio

$$I = \frac{(\rho U^2)_c}{(\rho U^2)_\infty} = \frac{M^2}{DR} \tag{3}$$

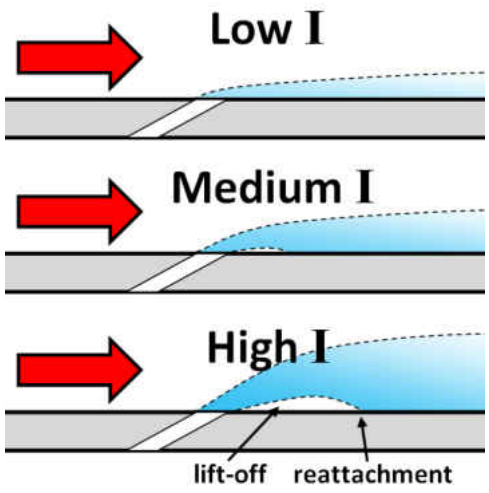

Figure 4: The general effect of momentum flux ratio on jet lift off

1.4.3 Full Coverage Film Cooling

Throughout literature there are a very large number of film cooling studies, each of which may focus on a different quantity or arrangement of holes. Lot of work has been focused on discrete, single film cooling holes. Some of which focus greatly on the governing physics and flow field by using large scale film cooling holes, or even the effect of new, more complex geometries as compared to basic ones (e.g. shaped holes vs. cylindrical holes, etc.). Other studies utilize only a few holes forming a single row, whether it be to investigate the effect of lateral hole spacing on film jet interaction, or any other geometrical configuration. Many correlations and approximations can be found in literature which utilize single row data for conjecturing what the given result of interest (e.g. effectiveness, heat transfer coefficient augmentation, etc.) would be with the subsequent addition of rows of film cooling holes. Such works are also performed for cases with several rows of film cooling holes, to both validate/generate correlations and also directly measure a given result first hand without the use of correlations. As in the case for this study, only full coverage film cooling arrays are considered in the text matrix. These arrays are composed of many rows of film cooling holes.

Even though there is an extensive amount of literature on film cooling in general, there is a much less complete look at the field of full-coverage film cooling. A majority of works in full-coverage film cooling are plotted with their case parameters, Figure 5. It is clear that the available literature focuses on relatively small hole spacings, $<15D$. Also, many studies focus on very simple hole orientations, α=90°, β=0°. The current study focuses on larger spacings, $P/D=X/D$=23, and angled holes, α=45°, β=-45°, +45°, described in more detail in a following section. Further novelty is achieved through implementing a compound angle shift after 12 rows into the array.

Furthermore, much of the data sets from the studies below are incomplete; they do not present both adiabatic film cooling effectiveness and heat transfer augmentation.

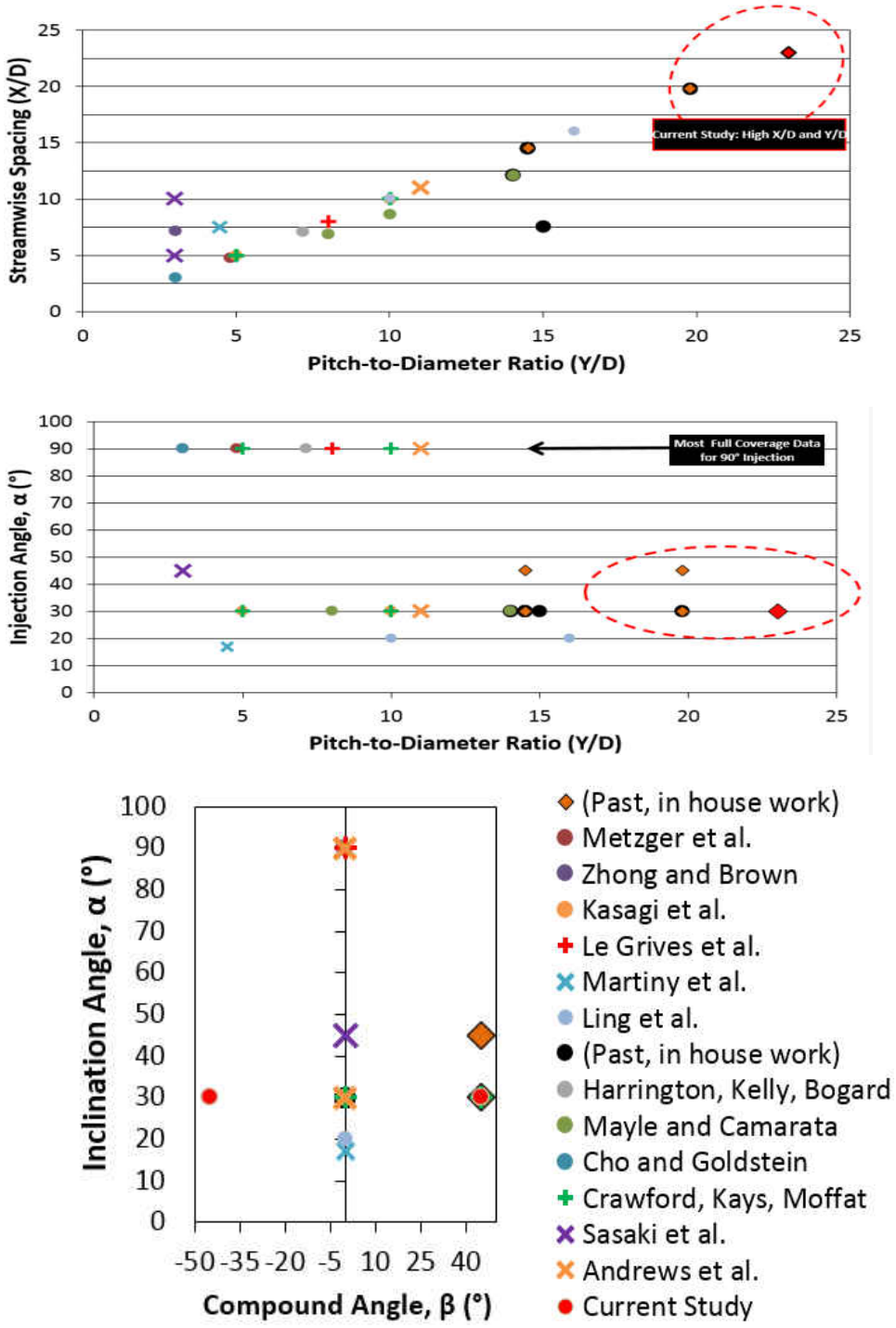

Figure 5: Literature geometric parameters compared with current study [34 -50]

1.4.3.1 Multihole Cooling Film Effectiveness and Heat Transfer [17]

The effect of hole pitch-to-diameter ratio and blowing ratio is studied by determining adiabatic effectiveness and heat transfer augmentation. All the holes are inclined at α=30° and compounded at β=45°. The focus of the study is to provide more information on the influence of hole and row spacing on film cooling array performance. Tests are run at a film-cooling Reynolds number, *Re*, of 3600, where measurements are taken in a span-averaged manner. The reported uncertainty in heat transfer coefficient is 8%.

Mayle concludes that the integrity of each individual jet can be seen in the adiabatic film-cooling effectiveness. This is universally agreed upon in the current understanding of film literature. The interaction and coalescence of individual jets is found to have a detrimental impact upon downstream film-cooling effectiveness. Average heat transfer augmentations up to 2.5 are measured, showing that heat transfer augmentation must be considered while designing a film-cooling array.

1.4.3.2 Full-Coverage Film Cooling Part I: Comparison of Heat Transfer Data for Three Injection Angles [18]

Heat transfer experiments are run with α=90°, β=0°, α=30°, β=0°, and α=30°, β=45°. Zero degree inclination angle produces the greatest heat transfer augmentation. Increasing the number of rows increases the downstream recovery region affected area. A compound angled, inclined hole at a mass flux ratio of 0.4 to 0.5 provides the lowest heat transfer augmentation. The highest increase in heat transfer augmentation is seen by normal injection of coolant. An increase in heat transfer augmentation for all geometries is seen at mass flux ratios greater than 0.4. Increasing the number of downstream rows keeps an elevated heat transfer coefficient while increasing the area being protected.

1.4.3.3 Full-Coverage Film Cooling Part I: Comparison of Heat Transfer Data for Three Injection Angles [19]

This study was aimed at characterizing the heat transfer augmentation produced by three film cooling hole orientations; normal injection with no compound angle, inclined at 30° with no compound angle, and finally inclined at 30° with a compound angle of 45°. As expected, conclusions from the study indicated that heat transfer augmentation was maximized for the normal injection case, and any addition of film cooling rows yielded higher levels of heat transfer in the recovery region. Relevant to this current body of work, comparing the results in heat transfer augmentation for 90° and 45° provides insight into the physical mechanics of the film cooling jets

1.4.3.4 An Investigation of the Heat Transfer for Full Coverage Film Cooling [20]

This study is also a full coverage film cooling study, where ten rows of normally oriented film cooling holes, relative to the heat transfer surface, were tested to investigate the effect of altered levels of freestream turbulence and unheated/heated started lengths prior to the array of film cooling holes. A chief result from this experimental study was that the high and low turbulence levels in the freestream did not indicate a change in heat transfer augmentation, likely due to the relatively large amount of disturbances and turbulence factored from the film cooling holes injecting in a normal configuration. This result from the study by Kelly and Bogard [19, 20] alleviates concern in the present study of slightly varying turbulence levels effecting heat transfer result.

1.4.3.5 Film Cooling Effectiveness for Injection from Multirow Holes [21]

This is a study investigating the comparison of full coverage array data to predictions of full coverage array data from single row data, and different methods to generate such predictions. The array tested experimentally was comprised of tightly spaced (P/D=3, X/D=5) holes, with compound angle configurations of 45°. The general conclusions were that the traditional

superposition model, and the point source model only performed with reasonable accuracy at sufficiently low blowing ratios (M<0.15), for the tighter lateral and streamwise spacing's. The test matrix and geometric specimen in this current study exceed the low blowing conditions that were found to be accurately predicted with different models, and thus such models cannot be concluded as applicable directly (without modifications) to this current study.

1.4.3.6 Turbulence intensity effects on film cooling and heat transfer from compound angle holes with particular application to gas turbine blades [22]

This study concludes that the effect freestream turbulence has on film cooling effectiveness and heat transfer is not different for compound angled holes, compared to film cooling holes without compound angles. The effect of freestream turbulence on film cooling effectiveness is most clearly prevalent at off-center locations in the immediate injection region of compounded film holes, where the film experiences significant lateral spreading. Some more well-established links between freestream turbulence and film cooling performance are also validated in the study, such as that the freestream turbulence intensity tends to yield more uniform cooling over the heat transfer surface.

1.4.3.7 Film cooling from two rows of holes with opposite orientation angles: injectant behavior and adiabatic film cooling effectiveness [23]

Ahn, Jung and Lee investigate injectant behavior and adiabatic film cooling effectiveness for two rows of hole with opposite orientation angles. Four configurations are investigated, inline, staggered and two arrangements between the inline and staggered, where z/D=6D, 3D, 1.5D and -1.5D respectively. Inclination angles for all configurations are set to 35°. At lower blowing ratios, the injectant remains attached to the wall, therefore the spatial uniformity is seen to be a larger factor in determining the overall film cooling effectiveness than local film cooling effectiveness level. Increasing blowing ratios to 1.0 and 2.0 increases the interaction between injectant from the

upstream and downstream holes. At higher blowing ratios, inline holes provide higher adiabatic film cooling effectiveness when compared to the staggered configuration. Lower blowing ratios, near M=0.5 provide the highest adiabatic film cooling effectiveness in the near-hole region, where the higher blowing ratios provides better coverage farther downstream.

1.5 Scope and Objective of Current Study

As from the literature survey, the current study utilizes larger lateral and larger streamwise hole spacings than found in the presented literature survey. Most of the cases from the literature survey presented here are also only considering a large array of film holes with simple hole orientations, as in normal injection without compounding. This study not only investigates arrays with larger hole-to-hole spacings, but also relatively unpopular hole configurations, such as compound angles of both ±45°. The staggered pattern of positive/negative compound angle in this study also creates yet another unique characteristic in the film cooling arrays which is unique to cases found throughout literature. In regards to the literature surveyed, it is clear that this study proves quite unique from other cases in literature due to large hole spacings within the array (lateral and streamwise), uncommonly large compound angles, and a compound angle shift within the array.

The objective of this work is to consider the test specimen under the test conditions specified in the test matrix, Table 2, and quantify both film cooling effectiveness and heat transfer augmentation for each case.

CHAPTER 2: EXPERIMENTAL SETUP AND TESTING PREPARATION

2.1 Geometries Tested

This chapter describes the physical setup for the experimental tests of film cooling arrays, performed at the Siemens Energy Center, the Center for Advanced Turbomachinery and Energy Research at the University of Central Florida. A detailed description will be provided in this section on the fabrication and configuration of the geometry specimen tested, several technical details of the wind tunnel and crossflow environment, both experimental testing methodologies, and an uncertainty quantification.

2.1.1 Independent Testing Parameters Which Influence Film Cooling

The fundamentals of film cooling necessary to the current study are presented below. In a broad sense, there are geometric parameters and flow parameters which affect film cooling. The hole geometry and orientation have a profound effect on the behavior of the jet leaving the wall. Also, several fluid mechanic parameters dominate the performance once a hole geometry is decided.

Some concepts and parameters discussed in the first chapter will be summarized and repeated here for clarity to those readers who wish for a brief description of test parameters.

Nomenclature adopted for this body of work describing the cylindrical hole geometry is diagramed in Figure 6. Figure 7 details the geometric parameters describing multiple film cooling holes.

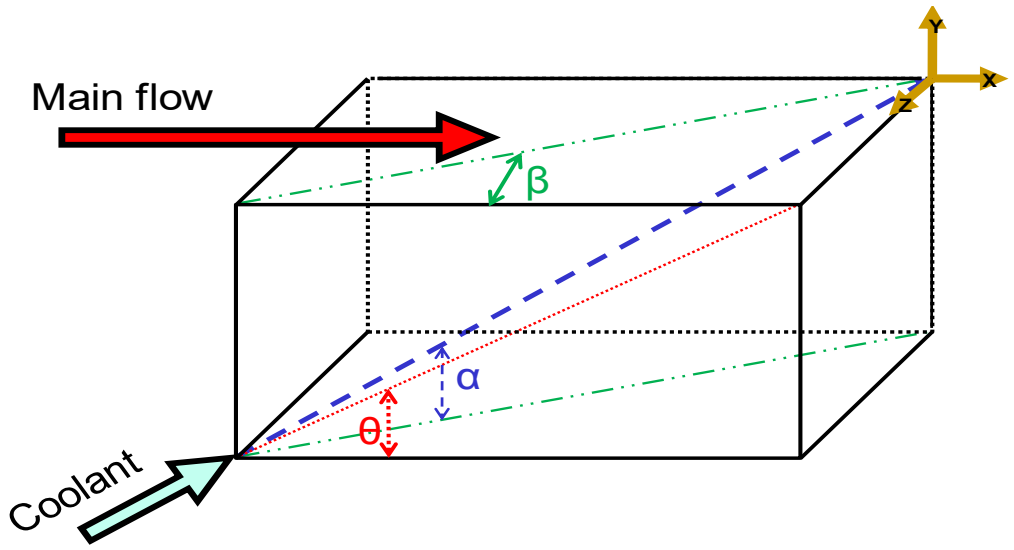

Figure 6: Coordinate system and nomenclature for angles describing film hole geometry

The inclination angle, or surface angle, α is typically between 15-90° for film cooling applications. The effect of α is to adjust the wall normal component of momentum of the coolant jet as it leaves the wall. The compound angle, or flow angle, β can vary anywhere between ±90°. Any deviation from 0° will cause an asymmetric vortex pair exiting the film hole. This is beneficial because it disrupts the induced wall normal velocity, and instead promotes spreading of the jet. The length-scale used for film cooling studies is generally the hole diameter, D. The lateral distance between two adjacent holes, measured from hole exit breakout to adjacent hole exit breakout, is known is the pitch, P. Finally, the stream-wise pitch, X, is the stream-wise distance between two adjacent rows and is normalized to X/D.

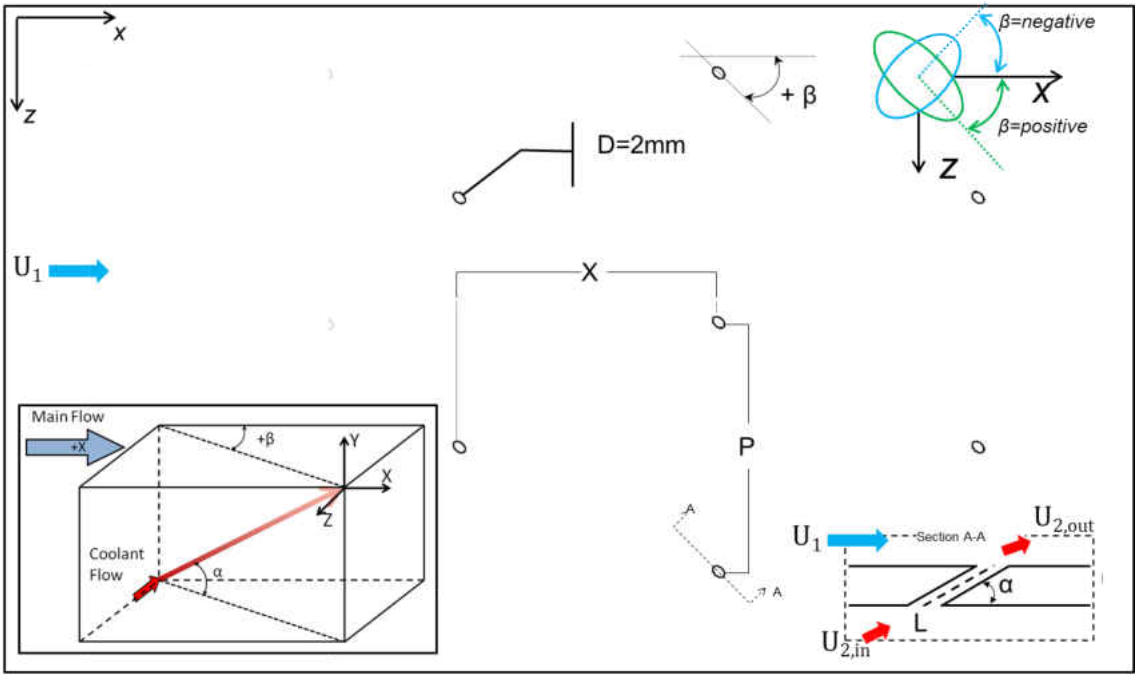

Figure 7: Geometric parameters describing an array of film cooling holes

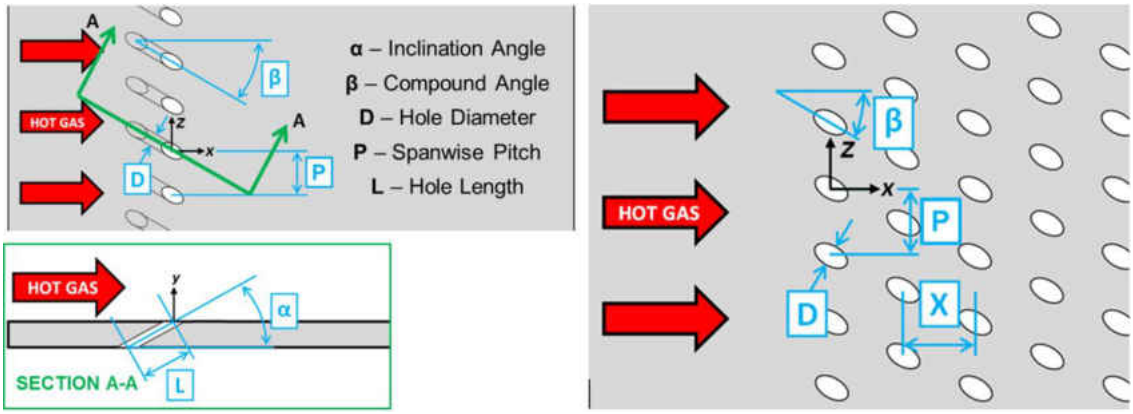

Figure 8: Geometric parameters describing an array of film cooling holes

Up to this point, the geometric parameters relevant to this body of work which affect the film cooling performance have been briefly discussed. The parameters pertaining to the flow of both the primary and secondary flow are now discussed, for this jet in crossflow situation.

Shown in Equation 4, the blowing ratio (M) describes the ratio of coolant mass flux to mainstream hot gas mass flux. This ratio indicates the amount of mass injected into the boundary layer. Both the mainstream and coolant density (ρ) and average velocity magnitude (U) are used.

Equation 4: Blowing Ratio

$$M = \frac{(\rho U)_c}{(\rho U)_\infty} \tag{4}$$

Other parameters often used to describe film cooling performance are the density ratio (DR) and the momentum flux ratio (I).These are calculated using Equation 5 and Equation 6, respectively. The influence of momentum flux ratio on the dynamics of the jet is shown in Figure 9.

Equation 5: Density Ratio

$$DR = \frac{\rho_c}{\rho_\infty} = \frac{T_\infty}{T_c} \tag{5}$$

Equation 6: Momentum Flux Ratio

$$I = \frac{(\rho U^2)_c}{(\rho U^2)_\infty} = \frac{M^2}{DR} \tag{6}$$

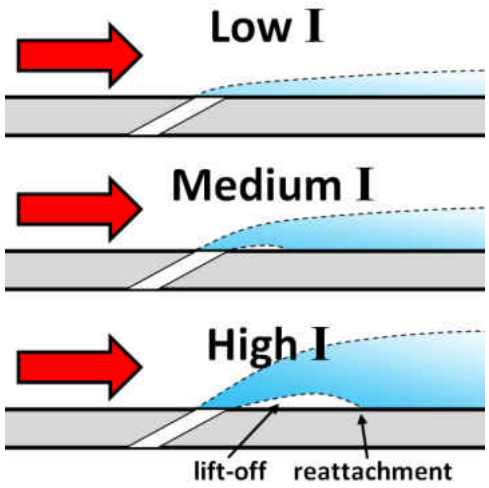

Figure 9: The general effect of momentum flux ratio, describing lift off

2.1.2 Test Matrix

The focus of the current study is the quantification of local heat transfer augmentation and adiabatic film-cooling effectiveness for two full-coverage film cooling surfaces. All specimen have 22 rows of holes in the streamwise direction. In the lateral direction, all full coverage film cooling rows have a total of 10 holes. All specimens have an *L/D* of approximately 14 for holes within the regular array. The test matrix can be seen in Table 2.

Table 2: Geometric test speciman matrix for current study

Specimen	*α (°)*	*β (°)*	*X/D*	*P/D*	*Nx*
FC.V	45	+45/-45	23	23	12 / 10
FC.VI	45	+45	23	23	22

2.1.3 Machining Process

The fabrication process for the test geometries began with creating CAD drawings. A CAD drawing for one of the geometries used in heat transfer augmentation testing can be seen in Figure 10. A CNC machine is used to machine all test geometries. Prior to machining the Rohacell plates, several fine grades of sandpaper are used to create a smooth flow side surface. Flanges are machined on the edges of the test section, as in Figure 11, such that the test plate's surface would be flush with the surface of the wind tunnel. The spindle angle of the CNC machine was altered to vary the end mill's angle relative to the surface, as in Figure 12. This enabled different inclination angles to be cut, in intervals of 15°. For each spindle orientation, several adapter plates had to be fastened to secure the angle of the cutting axis relative to the test surface. The spindle angle is set with an accuracy of ±0.1°, measured with a standard digital level. Gage blocks with an accuracy of ±40 seconds were also used to verify the hole angles machined. To achieve the desired set of compound angles for the test geometries, a fixture is made to change the orientation of the plate relative to the table. Figure 13 shows the fixture, where slots are made for all compound angles included in the test matrix.

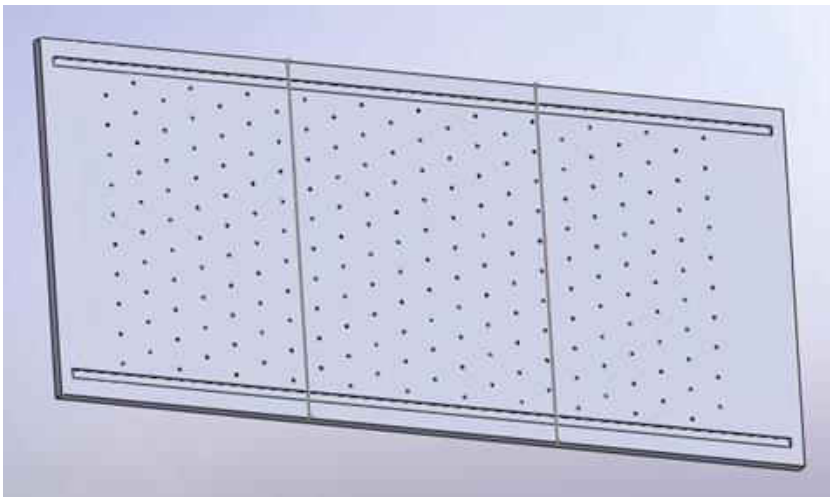

Figure 10: CAD drawings for a HTC test geometry with

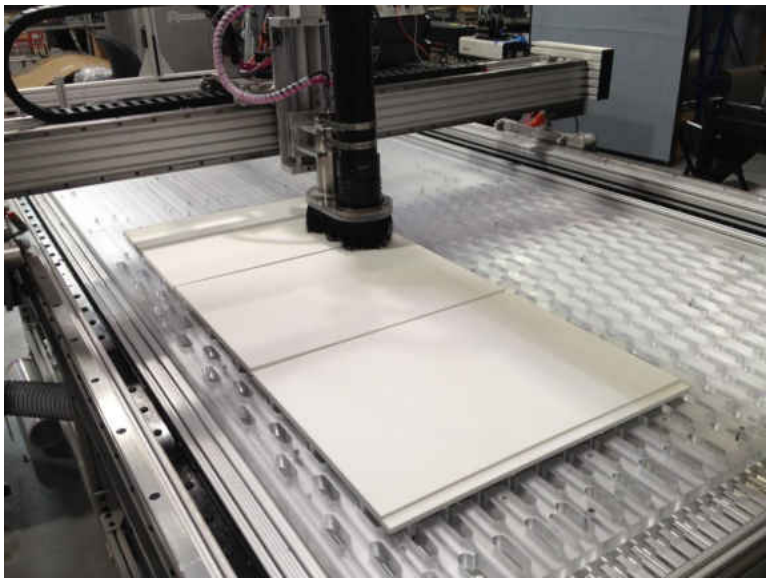

Figure 11: Plates were machined using a CNC

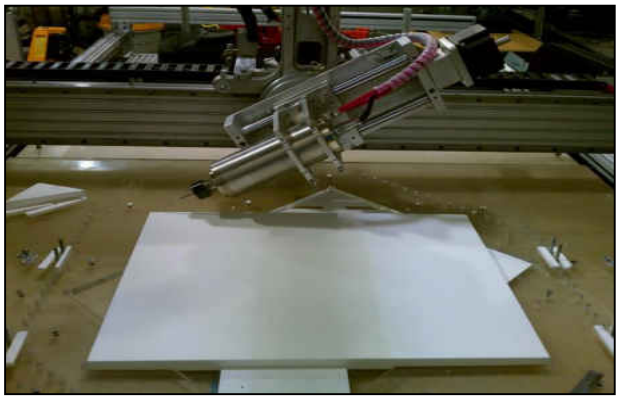

Figure 12: The spindle was rotated to achieve the desired hole inclination angle

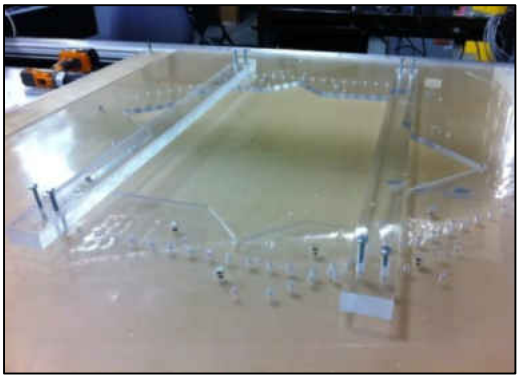

Figure 13: A fixture was made to hold the plates at the appropriate orientation angles (for machining the compounding angle)

After machining, the geometries are measured for uncertainty. Pin gauges are used to check each hole diameter as well as smooth any roughness caused from the milling process. The uncertainty of the pin gauges is 0.0025mm.

Due to the test sections being large, 1.2m in the flow direction, the large test surfaces were broken into streamwise segments for testing. A sample CAD drawing of such breakup of the test section can be seen in Figure 14. These segmented test section pieces were installed into the wind tunnel flush with one another, so that no physical flow trips were present between plates at their transitions. This required great attention to detail when installing the plates, and sometimes required rigid metal tape or wood putty to be placed at the transition.

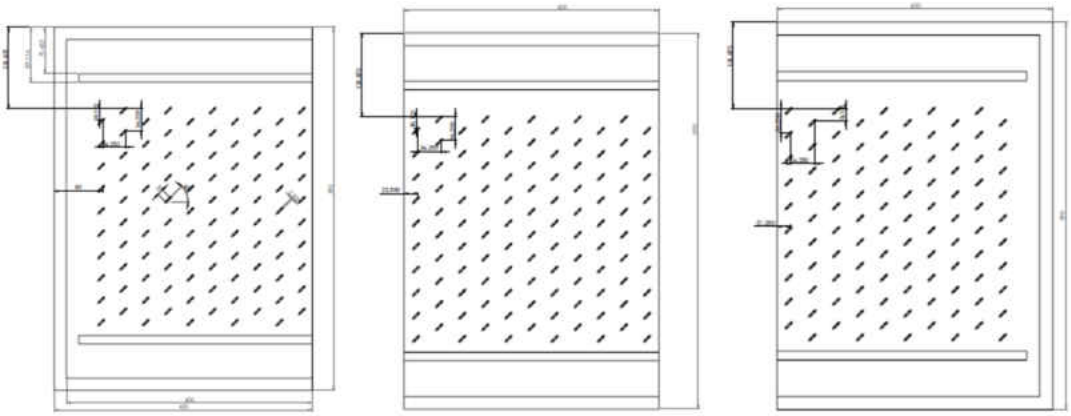

Figure 14: Test surface composed of three sections (plates)

2.1.4 Geometric Uncertainty

Two different cases are tested for film cooling effectiveness, and one case is tested for heat transfer augmentation. The geometric uncertainty table can be seen in Figure 15, where the uncertainty in each geometry fabricated and tested is listed. A cartoon image for clarity on experimental test setup of the heat transfer surface can be seen in

Geometry	*Material*	*Plate Letter*	*D (mm)*	*U_D (mm)*	*X (mm)*	*U_X (mm)*	*P (mm)*	*U_P (mm)*	*X/D*	*P/D*
FC.V	Rohacell	B	2.03	0.070	45.75	0.942	47.00	0.501	*22.58 ± 0.91*	*23.20 ± 0.84*
FC.V	Rohacell	C	1.85	0.157	46.81	1.217	47.09	0.941	*25.37 ± 2.25*	*25.52 ± 2.23*
FC.VI	Rohacell	B	2.02	0.053	47.17	0.823	47.23	0.436	*23.32 ± 0.73*	*23.35 ± 0.65*
FC.VI	Rohacell	C	2.02	0.053	46.80	0.949	47.21	0.401	*23.12 ± 0.76*	*23.32 ± 0.64*
FC.V/VI	Rohacell	A	2.06	0.023	46.89	0.613	47.12	0.446	*22.72 ± 0.39*	*22.83 ± 0.33*
FC.V	Acrylic	B	2.03	0.078	49.07	3.315	47.24	0.762	*24.21 ± 1.88*	*23.31 ± 0.98*
FC.V	Acrylic	C	1.93	0.051	47.21	0.788	49.49	0.483	*24.44 ± 0.76*	*25.62 ± 0.72*
FC.VI	Acrylic	B	2.23	0.073	46.42	0.547	46.42	0.472	*20.87 ± 0.72*	*20.87 ± 0.71*
FC.VI	Acrylic	C	2.19	0.096	46.66	0.484	47.40	0.419	*21.29 ± 0.96*	*21.63 ± 0.97*
FC.V/VI	Acrylic	A	1.99	0.038	46.93	0.768	49.16	0.810	*23.57 ± 0.60*	*24.69 ± 0.63*

Figure 15: Geometric uncertainty table

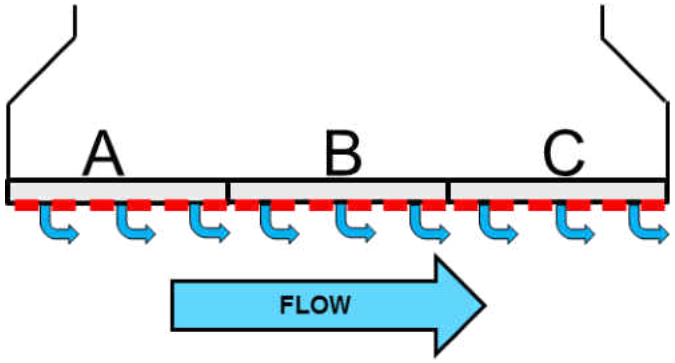

Figure 16: Experimental setup of heat transfer surface, comprised of three separate plates

2.2 Wind Tunnel

A wind tunnel is designed for the study to accommodate the large (1.2m x 0.55m) test section. This allows for a tunnel tailored for studying large arrays of film holes. The cross-section of the cross flow duct at the test section is 6”x 42”. This corresponds to a height of 73D for the film holes of D=2.06mm. This ensures the dynamics of the jets leaving the film holes are not affected by the duct. The cross section of the tunnel is sized so that the added mass due to injection is insignificant compared to the main flow; hence, the study is conducted in a nominally zero pressure gradient boundary layer (until pressure insert is put in).

A model of the tunnel is shown in Figure 17. There is a 45cm conditioning section upstream of the test section. There are 2 honeycombs of 1.3cm cell size and L/D=6. There are also 3 screens. These were installed to reduce the turbulence intensity of the main flow. After the conditioning section there is a slight 1-D nozzle with an area ratio of 2 leading up to the test section.

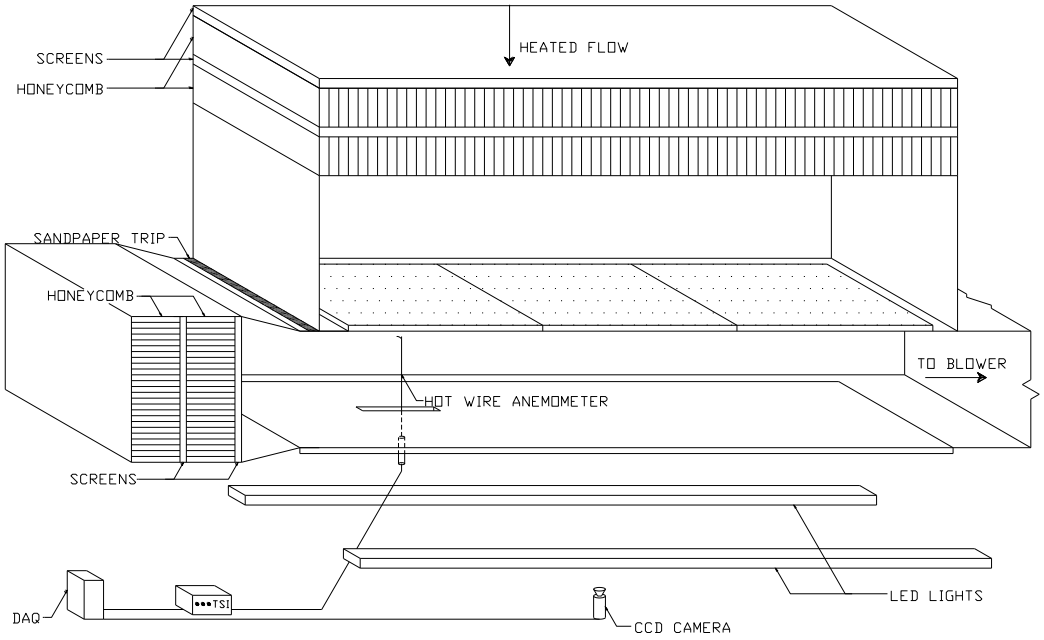

Figure 17: Wind tunnel (crossflow) and plenum (secondary flow) for large film cooling array studies

2.2.1 Blowers

The coolant flow is supplied by an 11kW Spencer Vortex blower capable of 35kPa and 0.3m^3/s. The main flow is driven by a 5kW Ziehl-Abegg fan capable of -1.5kPa and 6.6m^3/s. The flow originated from the blowers is routed to the plenum through PVC piping.

2.2.2 Wind Tunnel Flow Measurements

Several static pressure readings are taken along the test section to verify there is not a significant pressure gradient imposed on the flow for tests which do not utilize the pressure gradient wedge. Over the length of the 1.2m test section there is approximately a 15Pa pressure drop corresponding to a -12.5Pa/m favorable pressure gradient. Figure 18 shows the static pressure development in the streamwise direction for zero pressure gradient testing.

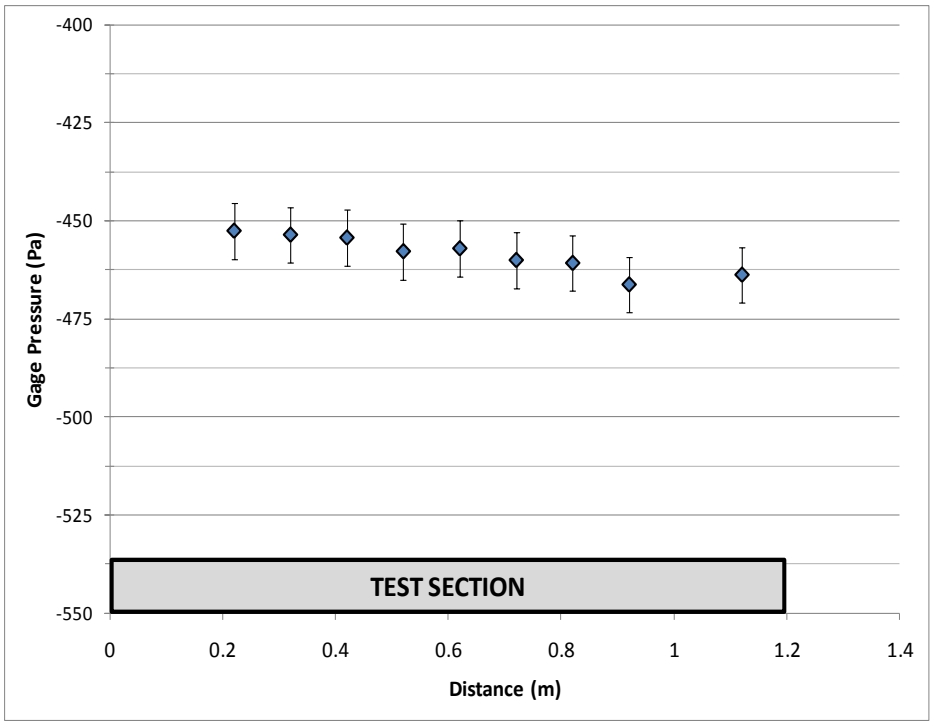

Figure 18: Static pressure variation in the stream-wise direction of the duct without the pressure insert in the wind tunnel

The freestream velocity, turbulence intensity, and several other flow measurements are quantified with a constant temperature anemometer (CTA), and displayed in Table 3. Two free stream velocities were tested to provide flow measurements for low and high freestream velocities. This is significant because the freestream velocity will be lowered for several cases involving a significant pressure gradient. The root mean square of the turbulent fluctuations for both freestream velocities is obtained from this data and the turbulence intensity (TI) of the mainstream is quantified at less than 1% for both cases.

Figure 19 shows the outer scaled velocity profile normalized by the freestream velocity of 27.2 m/s. Similarly, Figure 20 shows the boundary layer thickness for a free-stream velocity of 10.3 m/s. The data was acquired at a rate of 10kHz for 3 seconds per wall normal location. The

measurements started from a location of .13mm away from the wall, allowing for resolving as close to the wall as $y^+=10$.

Table 3: Flow measurements for wind tunnel with constant temperature anemometry

Freestream Velocity (m/s)	U	10.3	27.2
99% Boundary Layer Thickness (mm)	$\delta_{.99}$	9.1	8.8
Displacement Thickness (mm)	δ_1	1.25	1.04
Momentum Thickness (mm)	δ_2	0.82	0.75
Shape Factor	$H=\delta_1/\delta_1$	1.52	1.39
Reynolds Number on δ_2	$Re_2=U\delta_2/\nu$	500	1300
Reynolds Number on D	$Re_D=UD/\nu$	1300	3400
Freestream Turbulence Intensity	$TI=u'_{RMS}/U$	<0.01	<0.01
99% Boundary Layer Thickness to Hole Diameter Ratio	$\delta_{.99}/D$	4.6	4.4
Displacement Thickness to Hole Diameter Ratio	δ_1/D	0.62	0.52
Momentum Thickness to Hole Diameter Ratio	δ_2/D	0.41	0.38

Friction Velocity (m/s)	U_τ	0.52	1.25
Outer-inner length scale ratio	$\delta^+=\delta_{.99}U_\tau/\nu$	298	694
Cole's Wake Strength	Π	0.265	0.27
Constant in van Driest's damping function	A^+	26	26
von Karman's constant	κ	0.41	0.41

The velocity profiles for the two free stream velocities are matched with the law of the wall in order to determine the friction velocity. The profiles are then integrated to determine the integral thicknesses for the wind tunnel. The two inner scaled plots of the upstream boundary layer are shown in Figure 21 and Figure 22. Since the true wall normal distance is unknown for the first measurement point, part of initial processing to generate such plots requires regression between the friction velocity and the distance of the first measurement point. More specifically, the data is matched to the law of the wall for a range of values of both the initial wall normal

position of the measurement, and the shear stress term inside the friction velocity. After considering all physical combinations of both unknowns with a routine in MATLAB, the combination with the best fit to the law of the wall is chosen. Some physical insight can be made, as specifications of the boundary layer probe from the manufacturer allows for an initial guess at the distance from the wall. A modified wake function [31] is then added to the van Driest profile. 10,000 points from y+ = 10^-2 to y+ = 10^3, spaced logarithmically, are integrated from y/δ=0 to 1 with a rectangle rule for estimating the integral (integral thickness).

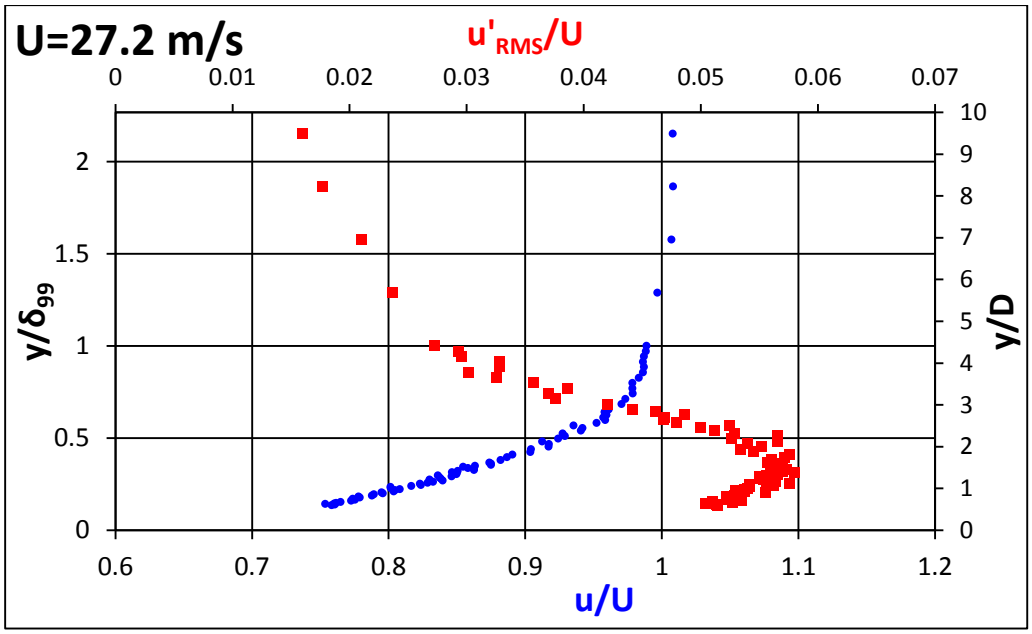

Figure 19: CTA velocity measurements of the boundary layer for the maximum tunnel free stream velocity

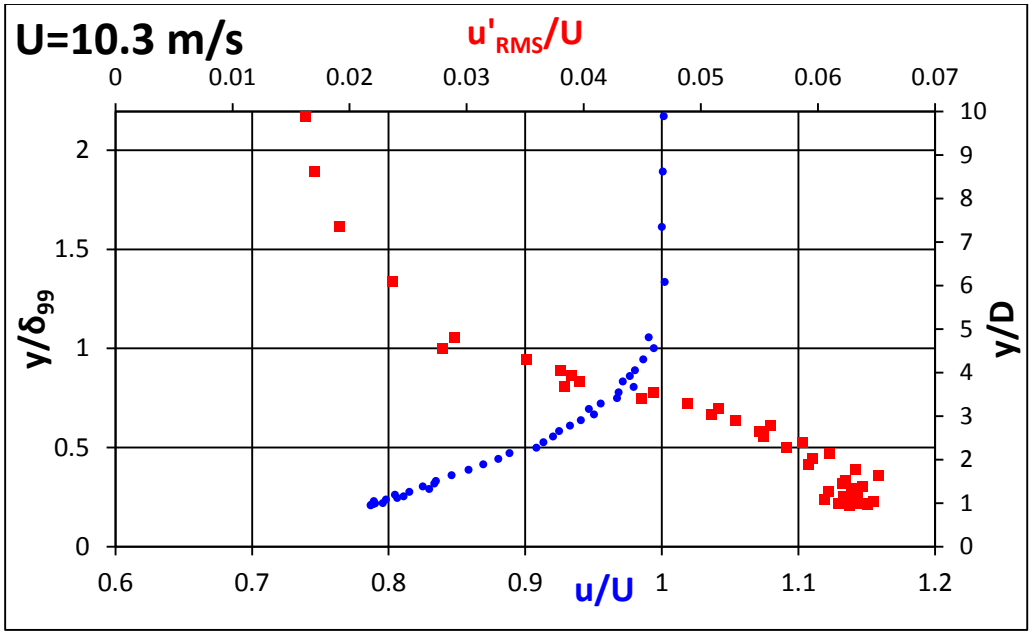

Figure 20: CTA velocity measurements of the boundary layer for a low tunnel free stream

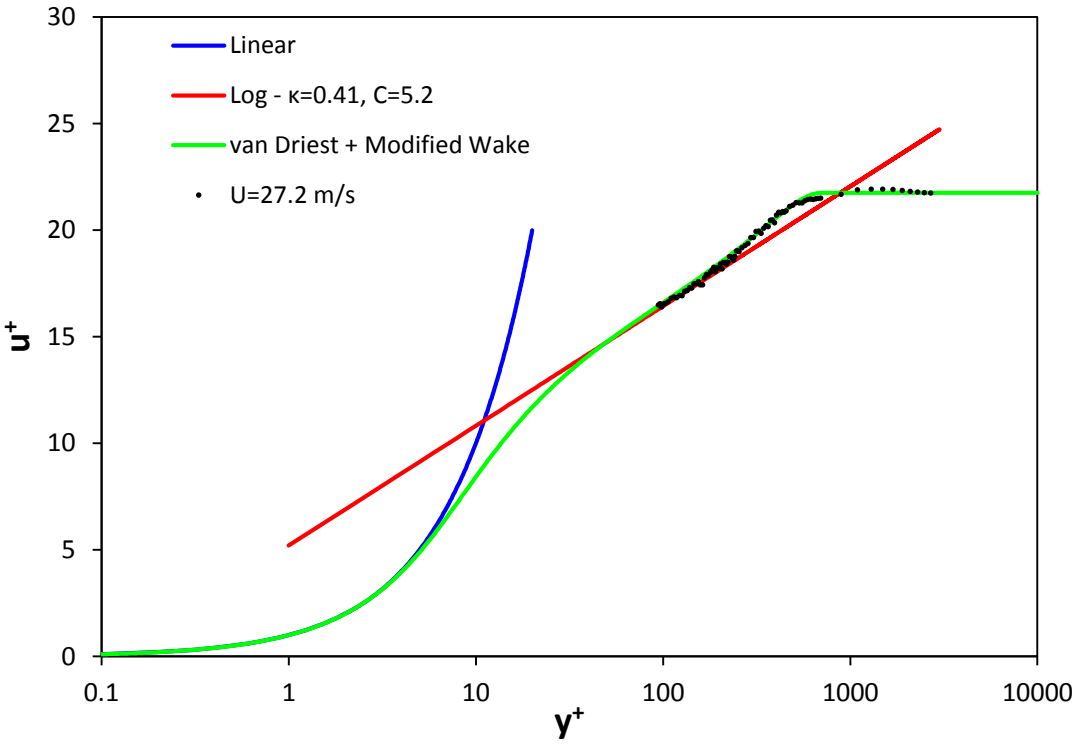

Figure 21: Inner scaling of boundary layer for the tunnels maximum free stream velocity

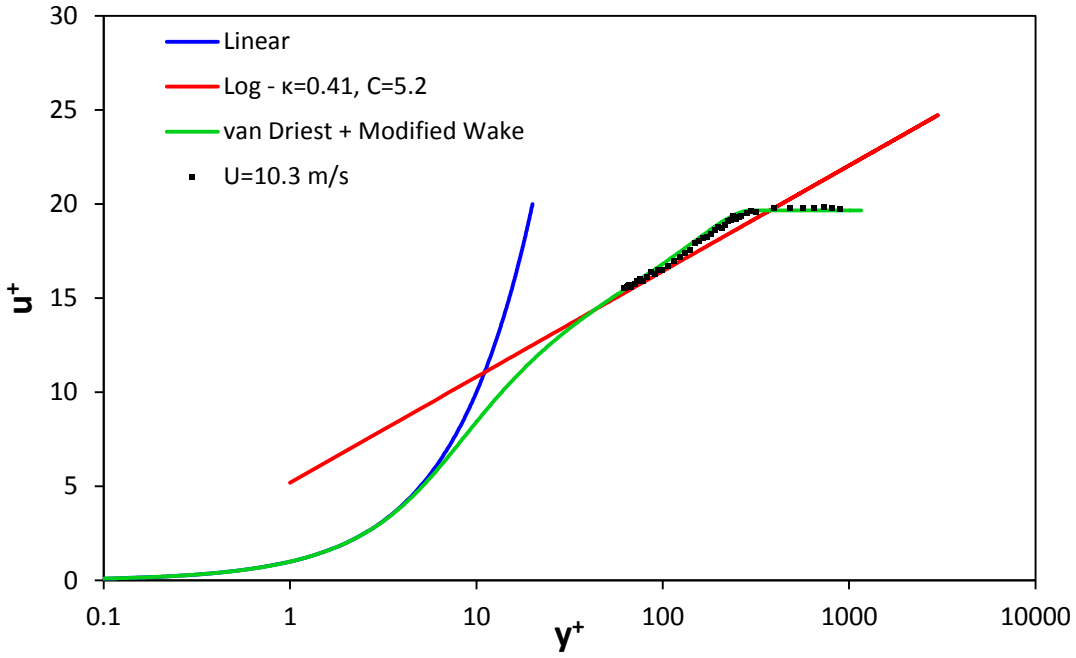

Figure 22: Inner scaling of boundary layer for a lower tunnel free stream velocity

2.3 Measurement Techniques

2.3.1 Testing Methodology – Adiabatic Film Cooling Effectiveness

To obtain values of adiabatic film cooling effectiveness, a low thermal conductivity test surface is machined with the full-coverage geometry into the material. The flow side is coated with TSP, seen in Figure 23. The temperatures are obtained from thermocouples in the freestream and in the holes, and adiabatic wall temperatures measured with TSP. These values are combined to yield local contours of effectiveness.

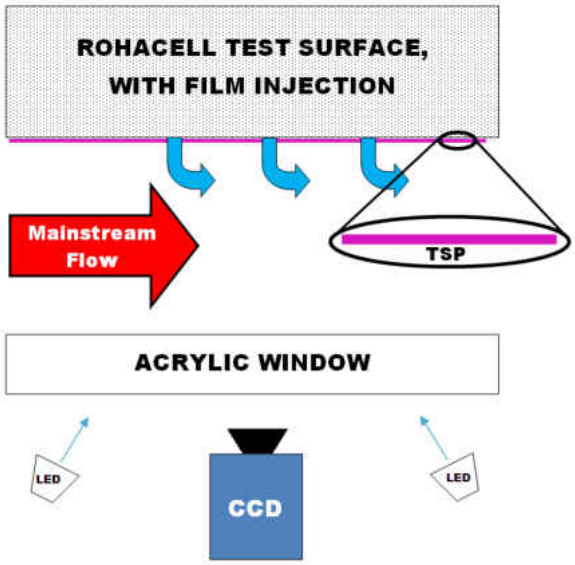

Figure 23: Adiabatic film cooling effectiveness experimental setup

The Adiabatic Wall – Rohacell RIMA

The material chosen for the test surface has a significant effect on the final adiabatic film cooling effectiveness results. Acrylic, a relatively low thermal conductivity material (k=0.2W/m-K) provides very poor quality effectiveness data. Hence, the current study uses Rohacell RIMA, low density closed cell foam as the 'adiabatic' test surface. The RIMA specification is suited especially for painting applications; hence, the roughness of the wall is minimal with the RIMA series. The thermal conductivity of Rohacell is k=0.029W/m-K. Due to the low strength of the material, aluminum brackets are cold-welded to the backside; these brackets improve data quality by minimizing the deflection of the test section during testing.

Temperature Sensitive Paint (TSP)

Pictures gathered with the CCD camera, and processed using in house codes which take the raw image files and process them into temperature distributions. A 1200x1600pixel resolution picture is taken with the camera. The calibration curve for TSP is based off of an intensity ratio as

a function of a temperature difference. Two pictures are needed to gather a temperature distribution, Figure 24. One picture is needed as a reference, the cold picture, with a known temperature over the entire surface being measured, along with the hot picture of the unknown temperature profile. This method of taking intensity ratios leads to a technique which is rather insensitive to lighting and paint variations, a huge strength of TSP. Eight pictures are taken for both the hot and cold set and are averaged into one picture. This multiple sampling is used to reduce the noise of the pictures.

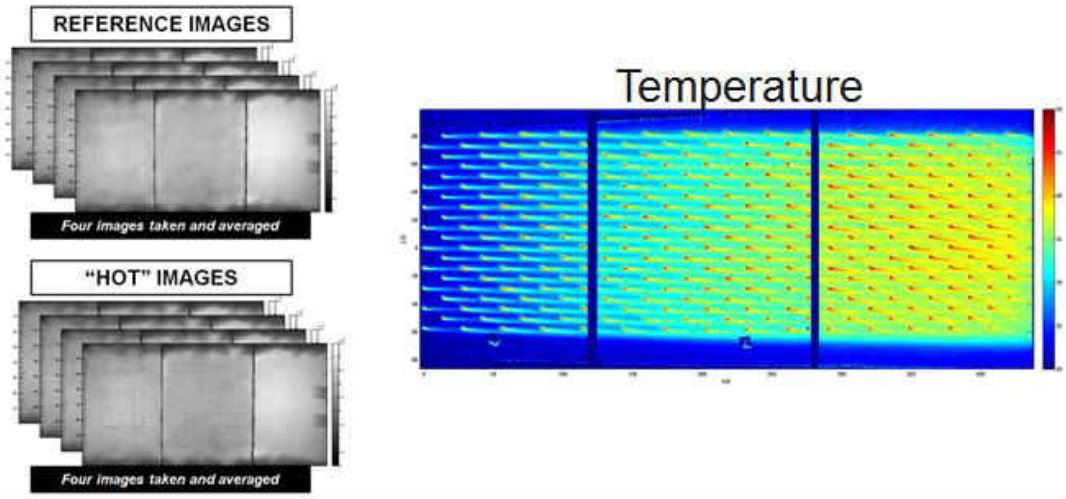

Figure 24: Process of processing temperature from raw data using TSP

By means of in house MATLAB codes developed specifically for processing TSP into usable heat transfer data, the intensity values of the cold pictures are read and averaged; the same procedure takes place for the hot images taken at steady state. Then through the use of calibration curves of the TSP, temperature values are obtained from the ratio of the intensity values of the hot to cold images. These calibration curves are obtained through experiment, Figure 25. A 1.3cm thick sheet of acrylic is painted with approximately 6 layers of TSP, at the same time as the test section, as the calibration piece. This piece is placed on a copper block on top of a small electric

heater which is used to heat the test piece to 10 different temperatures. With a thermocouple monitoring the temperature on the surface, steady state is monitored and temperatures are recorded. This calibration allows the use of the formula above to obtain temperature as a function of an intensity ratio.

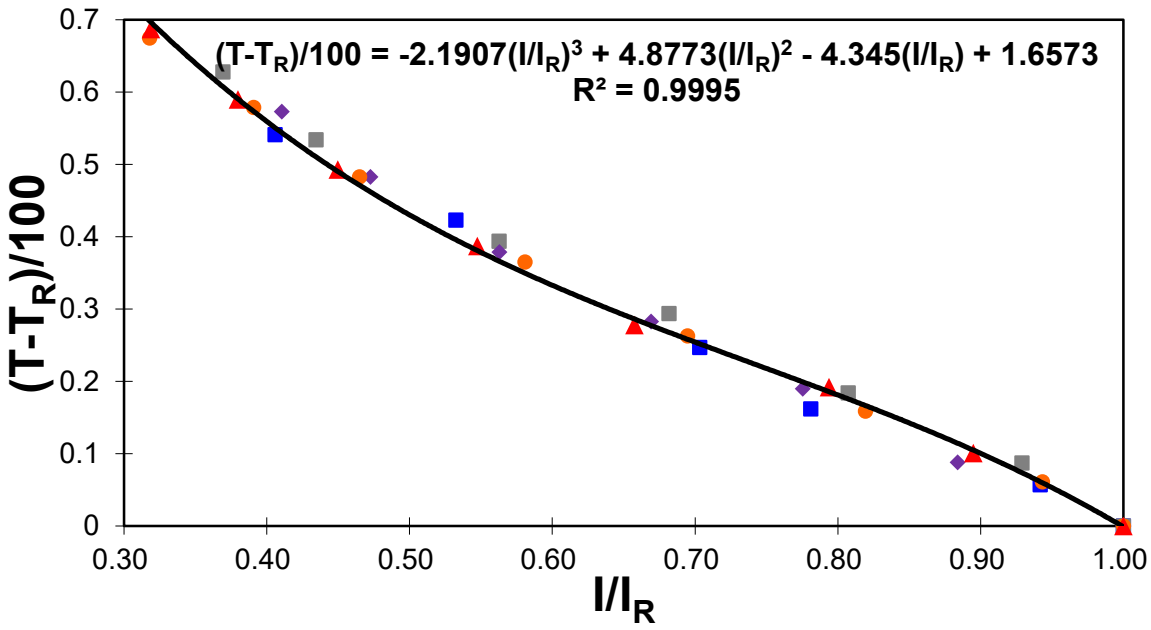

Figure 25: Typical calibration curve for TSP (in-house)

2.3.2 Testing Methodology – Heat Transfer Augmentation

The measurement of heat transfer augmentation requires an experimental setup different from the effectiveness testing. In concept, it is a steady state method for obtaining the heat transfer coefficient. Constant heat flux heaters are mounted on an acrylic test surface and coated with TSP, Figure 26. From an energy balance it is clear that in order to obtain the heat transfer coefficient, quantification of all the heat flow in, out and across the convective surface is necessary. The heat rate information for a 1-D process is quantified including the heat generated by Joule heating, heat conducted through the acrylic, and heat radiated to the tunnel. With these heat rates quantified, the heat removed through convection can be determined. First the heat transfer

coefficient defined by the temperature difference between the wall and the freestream is determined from this convected heat rate. Then the film effectiveness distribution, previously obtained, is overlaid on the data and used to define a heat transfer coefficient in the presence of the film. Finally, this corrected heat transfer coefficient is scaled by the heat transfer coefficient distribution without blowing, finally resulting in local heat transfer augmentation values.

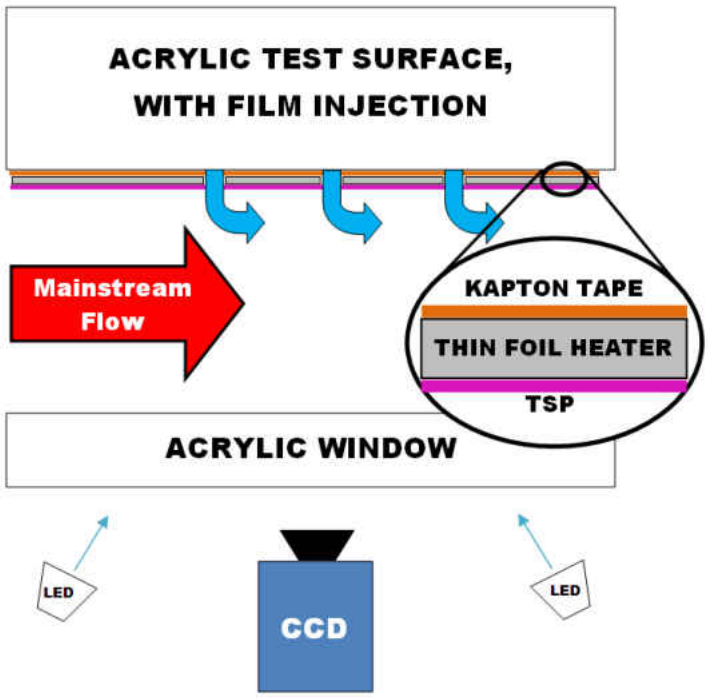

Figure 26: Heat transfer augmentation experimental setup

A constant heat flux condition is desired from the surface of interest. Since the heated surface has features that cannot be covered by the heaters such as film cooling holes, the heaters are installed around them without disturbing the flow that each feature has. The area if interest is heated as much as possible in order to obtain an acceptable temperature difference between the wall and the fluid. These foil heaters are made out of t=5.08*10-5m thick stainless steel type 321. Using data from Chu [32], a plot of temperature vs. electrical resistivity is created, seen in Figure 27. A curve is fitted to the plot over temperature range of interest, between 293K and 350K. This

curve fit is used in the data processing to help attain a higher degree of accuracy. These steel sheets are painted and then baked at a temperature close to 90°C for half an hour. Kapton tape is used on both sides of each heater because it is electrically isolative, thin and it is intended for high temperature environments. This helps ensure good heater performance. The heaters are then applied to the acrylic test surfaces in series. The series installation allows the heat rate to be determined by the current, providing a much more accurate method of calculation than installing them in parallel and measuring the voltage drops.

Several methods for measuring the current are used to provide the highest confidence in circuit current. This experimental parameter is one of the most important ones measured, which nearly everything is contingent on. For the first method of measuring current, A shunt resistor, R=1mΩ and i=30A maximum, is installed in-line with the heaters. Keithley model 2000 multimeter is used to measure the voltage drop across the shunt resistor, and from this voltage and the resistance of the shunt, the current through the circuit is calculated. The Keithley multimeter features a 0.1μV resolution with bias of ±(0.06%) the reading. The voltage drop across the shunt during testing is on the order of mV. The benefit of using this method to calculate current is that the shunt resistance is very controlled, and unchanging.

The second method for current measurement involves using a clamp meter. The meter is placed over a segment of the circuit's wire, and current measurements are directly made. This method is very beneficial because all of the circuits components are wired in series and it is easy to perform. To reduce the effect of the clamp meters inaccuracy, several sections of the circuits wire are bundled into loops. For each test, current measurements are taken over a section of a single wire, a three wire bundle, and a ten wire bundle. This inherently results in a smaller effect of the clamp meters uncertainty. Typically, the circuits measured current converged to the reading from the ten wire bundle (clamp meter reading divided by ten), which provides the most accurate

reading of all the methods used. One disadvantage of this method though however, is that the meters reading strongly depends on the tools orientation to the wire(s). This problem was averted by recording values for several orientations, and using an average.

The last method used to calculate the current was less robust, however serves as a double check and initial evaluation of circuit current. Prior to making the circuit live, a Keithley model 2000 multimeter was used to determine the circuit resistance. Using this resistance value, and the voltage across the variac, an initial determination for the needed voltage from the variac was made. The main limitation to this method is that the bias in the circuit resistance is significant relative to the overall circuit resistance. Even though the Keithley multimeter has very small bias, the contact resistance on the multimeter leads is inconsistent (because it is measured by hand over the circuit).

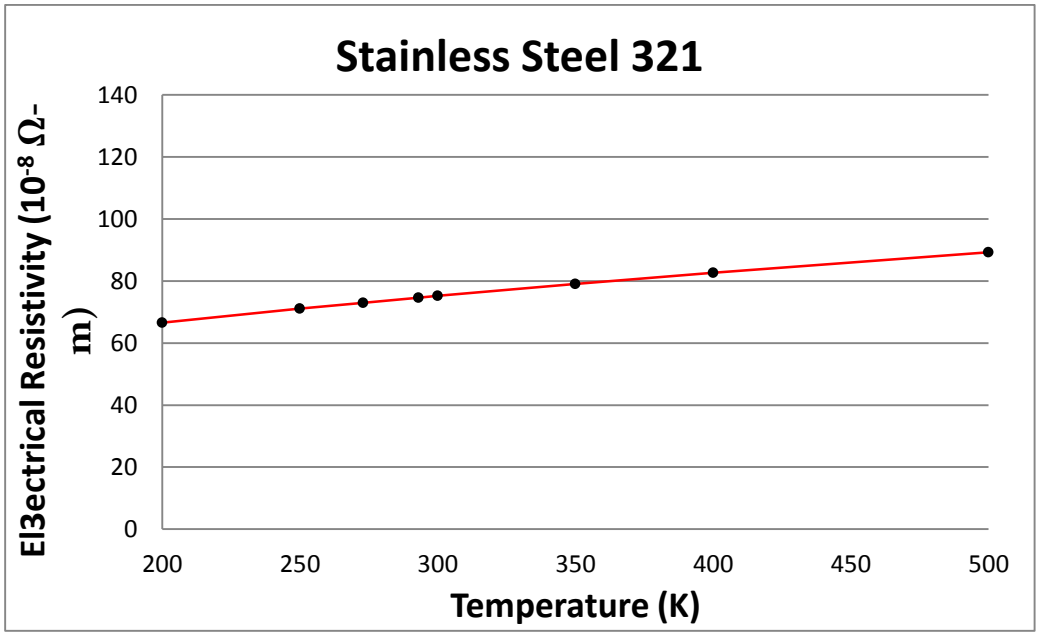

Figure 27: Stainless steel type 321 temperature vs. electrical resistivity

A 1-D control volume is placed at the convective surface of the heaters, Figure 28.

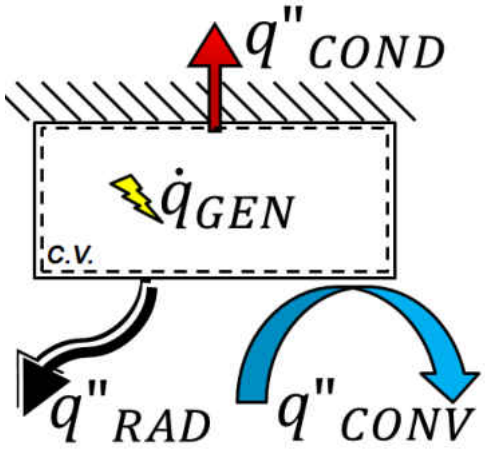

Figure 28: Control volume and energy balance of heater surface

In terms of Joule Heating, In order to determine the heat transfer coefficient, the electrical current (i) and heater resistance (R) are converted into an input heat flux. This is shown in Equation 7, where A_s represents the surface area of the heater exposed to the mainstream flow.

Equation 7: Input Heat Flux

$$q''_{gen} = \frac{i^2 R}{A_s} \tag{7}$$

The heater resistance is calculated using the resistivity (ρ_{el}) of stainless steel and the dimensions of the heater, as seen in Equation 8. The length (l) is measured in the span direction while the width (w) is measured in the stream direction. The thickness (t) is the thickness of the stainless steel foil, measured in the wall normal direction.

Equation 8: Electrical Heater Resistance

$$R = \frac{\rho_{el} l}{wt} \tag{8}$$

In terms of data reduction for heat loss, Necessary for determining the heat transfer coefficient are the other modes of heat transfer from the surface. Heat loss is correlated experimentally to determine what generated portion is lost to conduction and radiation, the remaining heat is taken to be convected away by the boundary layer.

Conduction loss, q''cond is quantified as a function of the temperature difference between the wall temperature Tw and the average backside acrylic temperature Tb. This also accounts for a small amount of radiation loss through the back surface. A schematic of this test setup is shown in Figure 29.

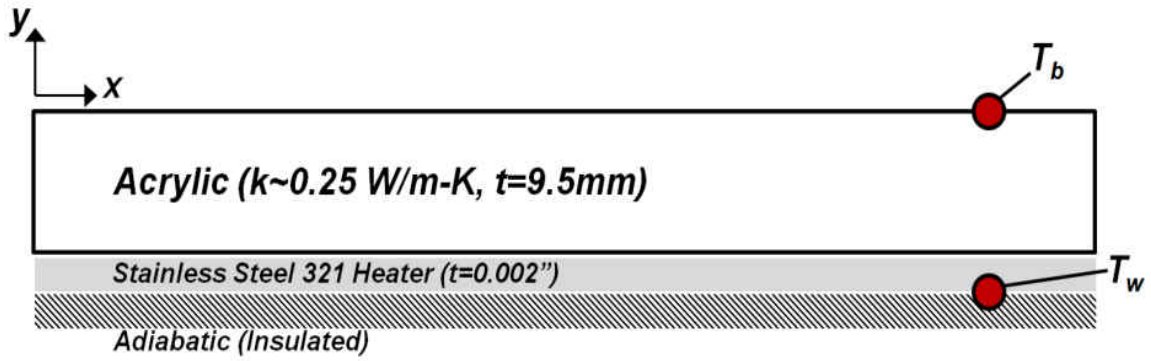

Figure 29: Conduction heat loss test setup

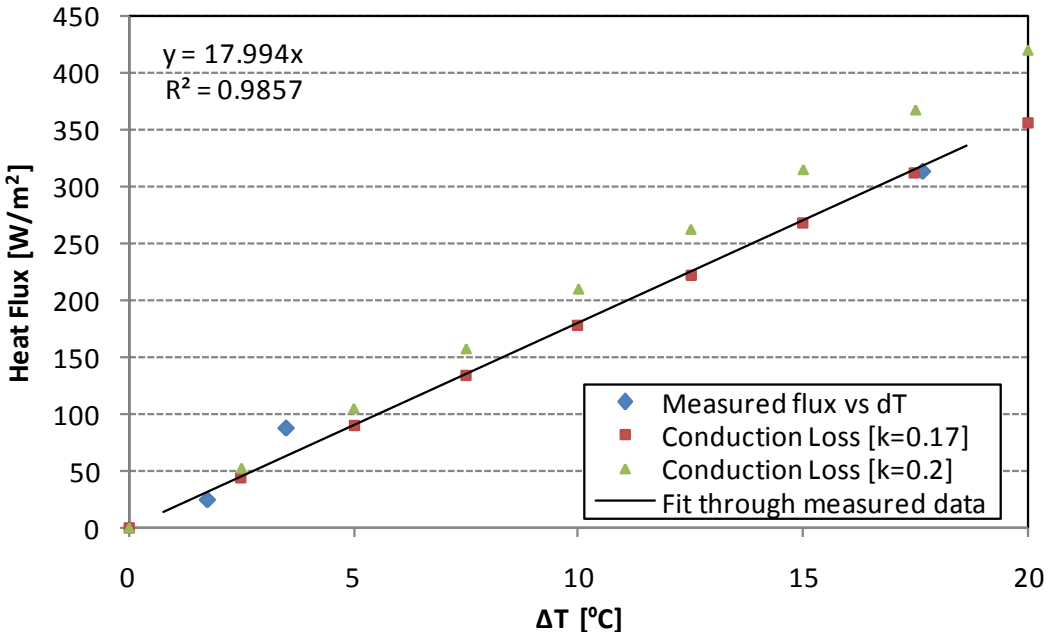

Figure 30: Conduction heat loss test results

Figure 30 shows the result of the conduction heat loss test. The resulting relationship between Tw and q''cond is described by Equation 9. Note that this loss is applied locally, as described in the 1-D heat loss correction section. The measured Tw profile and average Tb are easily combined to determine the q''cond at each pixel of captured data.

Equation 9: Heat loss as a Function of Wall Temperature

$$q''_{cond} = 17.994[T_w(x,z) - T_b] \tag{9}$$

Heat lost by radiation to the environment is also quantified through a separate experiment. This is achieved by insulating the backside of an acrylic plate and sealing the mainstream flow tunnel to prohibit air from flowing over the plate. A foil heater, coated with TSP, is attached to the acrylic plate to reproduce the conditions of a heat transfer experiment.

The results of this test, seen in Figure 31, show that there is a radiation loss of approximately 87% of the blackbody radiation exchange. The results of this experiment are in

agreement with estimates of radiation loss based on the emissivity of white paint. The radiation heat loss is therefore evaluated by Equation 10, where σ is the Stephan-Boltzmann constant.

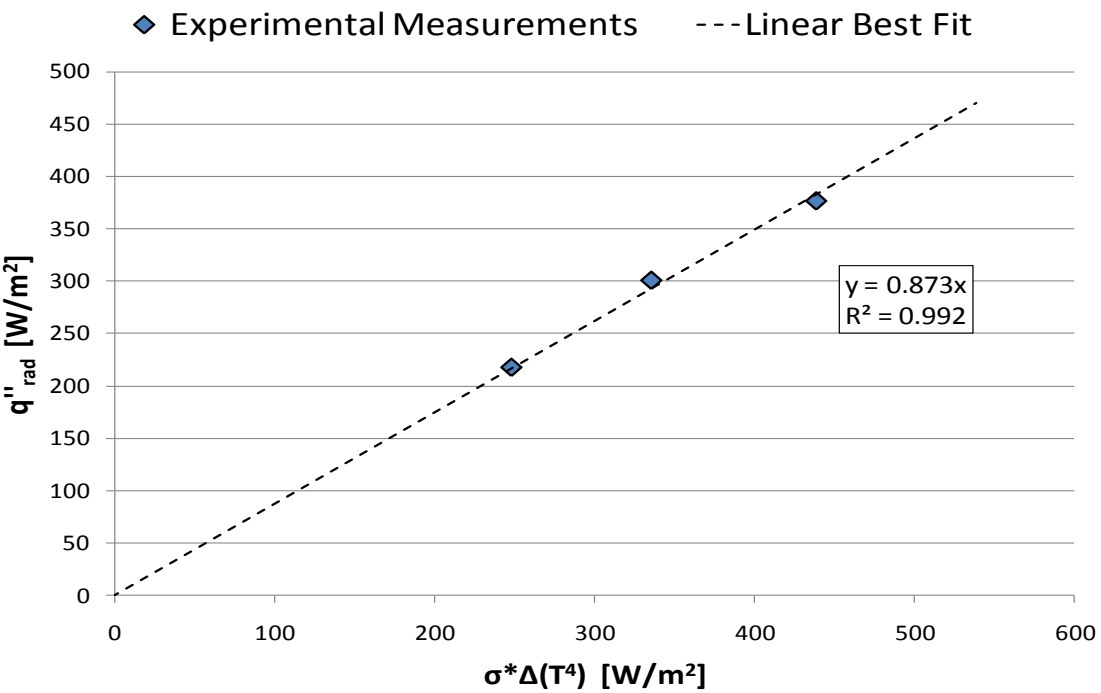

Figure 31: Radiation heat loss results

Equation 10: Radiation Heat Loss of the Experimental Rig

$$q''_{rad} = 0.873\sigma[T_w^4 - T_\infty^4] \quad (10)$$

The heat transfer coefficient is corrected for with the film temperature. Using this information, the local uncorrected heat transfer coefficient is calculated by Equation 11, where q_conv'' is determined by Equation 12.

Equation 11: Local, Uncorrected Heat Transfer Coefficient

$$h_u = \frac{q''_{conv}(x,y)}{T_w(x,y) - T_\infty} \quad (11)$$

Equation 12: Corrected Convective Heat Flux

$$q''_{conv} = q''_{gen} - q''_{cond} - q''_{rad} \quad (12)$$

Note that this heat transfer coefficient is "uncorrected" because it is determined using the mainstream flow temperature, which differs from the coolant temperature by 2-10°C. Once evaluated, the local effectiveness data is used with Equation 13 to account for this difference.

Equation 13: Corrected Heat Transfer Coefficient (Effectiveness Utilized)

$$h_f = h_u[1 - \eta\theta]^{-1} \quad where \quad \theta = \frac{T_\infty - T_c}{T_\infty - T_w} \quad (13)$$

The electric current measurement in processing the heat transfer data was very crucial to minimixing uncertainty, as the uncertainty in the current measurement was one of the most sensitive parameters. Thus as discussed earlier, there were three techniques used to ensure an accurate measurement was achieved. Figure 32 shows a cartoon image of the circuit with heaters in series. The conlcusion was that the shunt will be used for measurement in data processing

processing, while the voltmeter and clamp meter will be used to verify the shunt meter reading. In summary:

Shunt

Procedure: Voltage and resistance are measured across shunt

Benefits: Ideally most accurate (most controlled resistance)

Complication: Values of current are 2 orders of magnitude off, but match macro circuit calculation otherwise

Clamp Meter

Procedure: Placed over cable and reads current

Benefits: Easiest method, provides best

Complication: susceptible to orientation of reader, measurement bias not quantified by manufacturer

Clamp Meter

Procedure: Measure output voltage of the variac and total circuit resistance

Benefits: Mainly as a double check

Complication: Resistance measurement uncertainty (bias is on the order of circuit resistance)

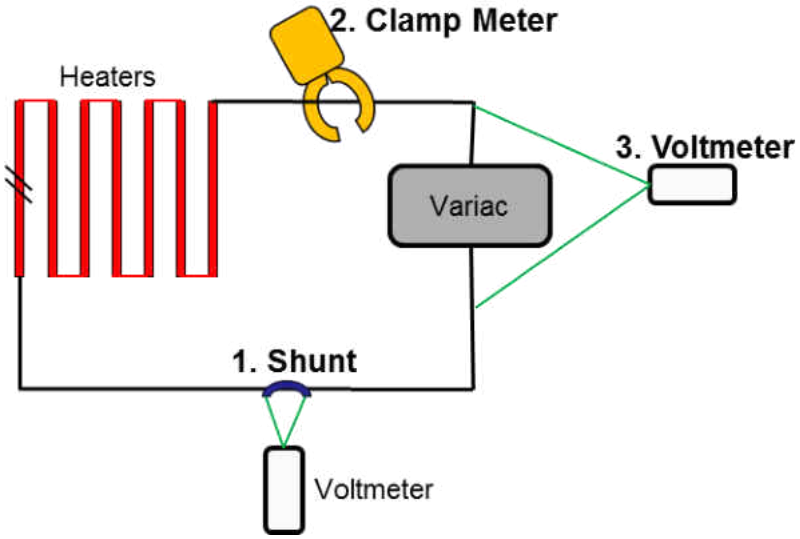

Figure 32: Cartoon image of circuit measurement devices

Additionally, the heat transfer data is more useful when presented as heat transfer enhancement, hf/h0, where h0 is the flat plate heat transfer coefficient in the absence of film cooling. h0 is determined analytically so that numerous heater geometries may be accounted for with a single equation. This analytical result is validated with a flat plate with various heated and unheated portions. These results are provided in a following section.

Equation 15, the unheated starting length equation for turbulent flow over a flat plate, is used to superimpose the effect of multiple constant heat flux surfaces and adiabatic surfaces to simulate the alternating thermal boundary conditions on the test surface. Figure 36 describes the heated and unheated surface conditions.

The following equations are used to evaluate h0:

Equation 14: Nusselt Number Flat Plate Correlation

$$Nu_x = 0.0308 Re_x^{4/5} Pr^{1/3} \tag{14}$$

Equation 15: Nusselt Number Correlation Involving an Unheated Starting length

$$Nu_x = \frac{Nu_x|_{\xi=0}}{\left[1-(\xi/x)^{9/10}\right]^{1/9}} \tag{15}$$

Equation 16: Uncorrected Heat Transfer Coefficient Without Blowing

$$h_0 = Nu_x * \frac{k_f}{x} \tag{16}$$

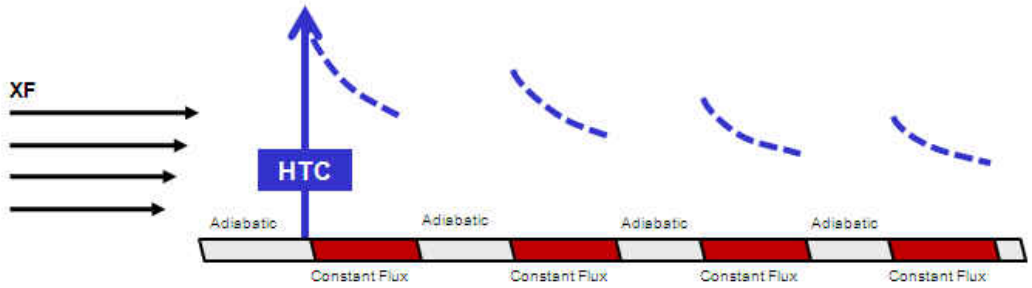

Figure 33: Heated and unheated surfaces and the effect on heat transfer

Equation 17: Heat Transfer Coefficient Augmentation Factor

$$HTC\ augmentation = \frac{h_f}{h_0} \tag{17}$$

2.4 Uncertainty Quantification

Quantification of uncertainty for the experiment has been conducted. Resultants can be seen at the top of each "tree". The calculated values are broken down into each measurand and the last values seen are the uncertainties in each measured value. These trees allow a view at each parameter contributing to the uncertainty of the final calculated value.

From Figure 34, one can see the contributing factor to uncertainty in the numerator of heat transfer enhancement. There is a large amount of measurands contributing to the experimental uncertainty in heat transfer enhancement leaving the final uncertainty in heat transfer

augmentation much larger than the uncertainty in adiabatic film-cooling effectiveness, whose uncertainty tree can be seen in Figure 35.

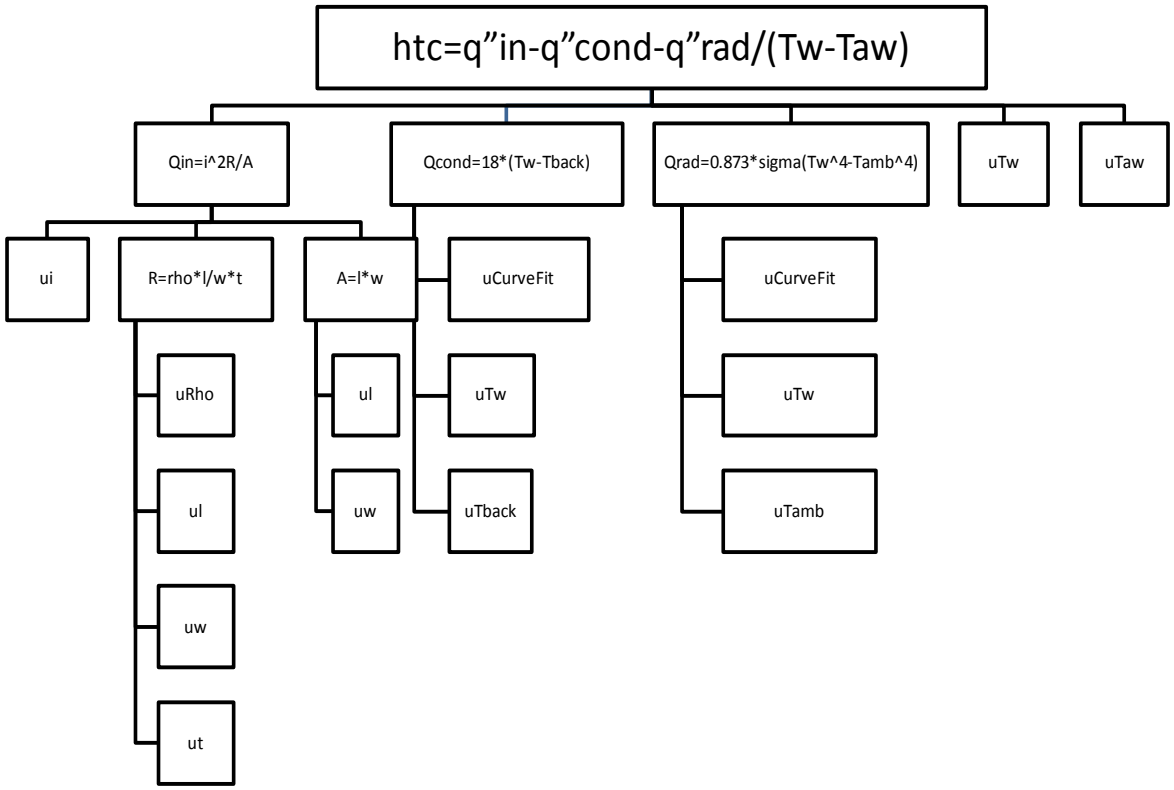

Figure 34: Contributions to uncertainty in heat transfer coefficient

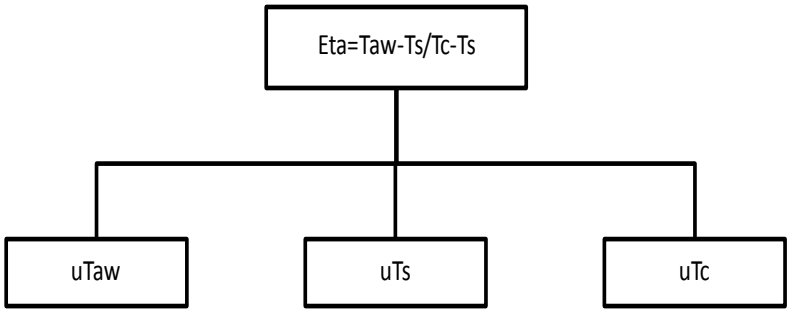

Figure 35: Contributions to uncertainty in adiabatic film-cooling effectiveness

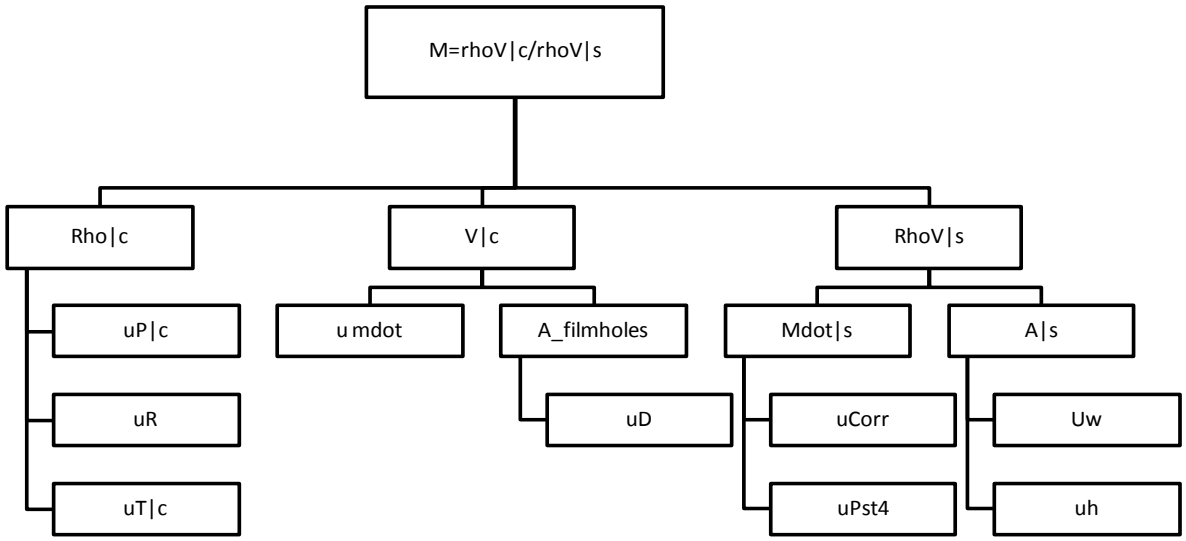

Figure 36: Contributions to uncertainty in blowing ratio

The propagation of error effect on the absolute error of the resultant, Ω, is quantified through Equation 18. The uncertainty trees shown above represent the j measurands, xj. In the case of adiabatic film cooling effectiveness and blowing ratio, the partials of the resultant with respect to each measurand are calculated analytically based off of the appropriate relationships. In the case of calculating the partials for the heat transfer coefficient, a singular perturbation method is used due to the complexity of the relationships.

Equation 18: Experimental Uncertainty

$$u_{\Omega} = \sqrt{\sum_{j=1}^{n} \left(\frac{\partial \Omega}{\partial x_j} u_{x_j} \right)^2} \tag{18}$$

Uncertainties are shown for film cooling effectiveness and blowing ratio in Table 4, where intermediate parameters necessary for the calculation of η and M are shown in Table 5 with their typical value and associated experimental uncertainties.

Table 4: Experimental uncertainty for heat transfer coefficient and augmentation, and effectiveness

Parameter	***Typical Value***	***Total Uncertainty (20:1)***	***Percent Uncertainty***
Heat Transfer Coefficient	100	9.6	9.6
Heat Transfer Augmentation	1.200	0.18	15
Effectiveness	0.2	0.02	10
Blowing Ratio	0.63	0.0567	9

Table 5: Experimental uncertainty in intermediate parameters

Parameter	**Units**	**Typical Value**	**Bias**	**Precision**	**Total Uncertainty (95% C.I.)**	**Percent Uncertainty**
Coolant Temperature	°C	50.49	0.05	1.399	1.4	2.8
Mainstream Temperature	°C	25.15	0.05	0.595	0.597	2.4
Adiabatic Wall Temperature	°C	29.51	0.005	0.447	0.447	1.5

CHAPTER 3: ADIABATIC FILM COOLING EFFECTIVENESS RESULTS

3.1 Benchmark

The experimental procedure for evaluating local film cooling effectiveness used in the current project has been previously compared with literature and shown to produce results corroborating with published data. Here, the comparison with Mayle [3] is shown, Figure 37, with the current study experiment matching literature within experimental uncertainty.

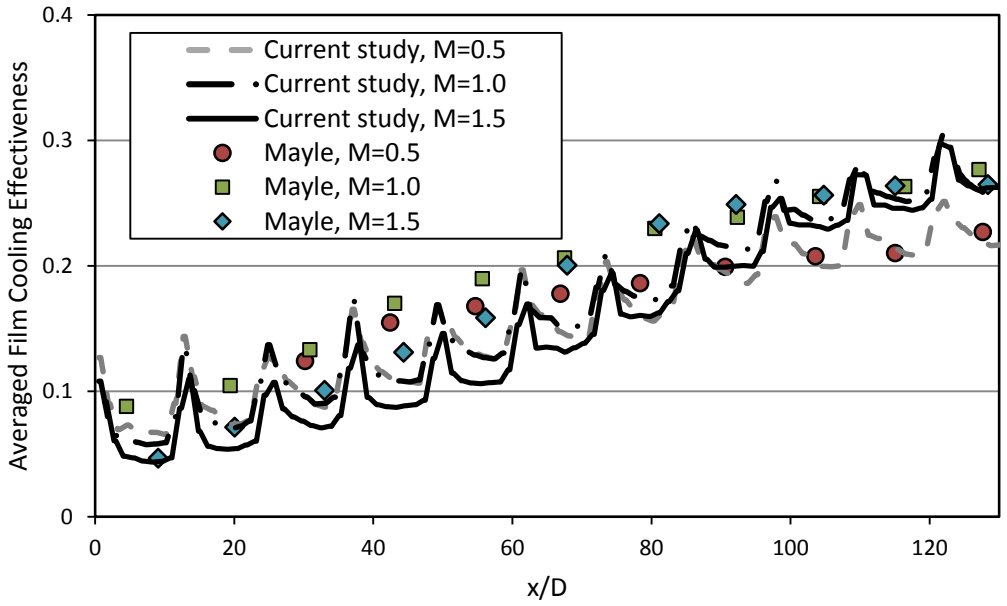

Figure 37: Comparison of in-house data vs. Mayle (1975)

3.2 Local Physics

Local representations of the adiabatic film cooling effectiveness are presented here. For each of the sets of images that are presented, the vertical axis represents the z/D axis (lateral/transverse dimension) and the horizontal axis represents the streamwise position within the array. All of the images are taken will a wall-normal reference to the heat transfer surface from a CCD camera, as described earlier in the experimental setup description of the report. It should be noted that the

streamwise segments that are blank between plates represent regions where the data acquired is discarded, as such locations are where the plate transitions occur. Such transitions are smoothed with woody putty and/or rigid metal tape, to ensure there are no disturbances (i.e. artificial flow trips) to the flow field, and thus the data acquired in such regions are void.

FC.VI and FC.V are identical until row 13. FC.V shows a very strong re-attachment after jet lift-off at M=2.0. At the compound angle change, the laterally averaged effectiveness decreases, this follows the same trend seen throughout all testing. Following the decrease in the laterally averaged effectiveness at the compound shift, the array recovers and begins to pick up. The average effectiveness profile flattens out when the alternating compound angle begins. Figure 38 shows the adiabatic film cooling effectiveness for the FC.V geometry at all blowing ratios, and similarly Figure 39 for FC.VI.

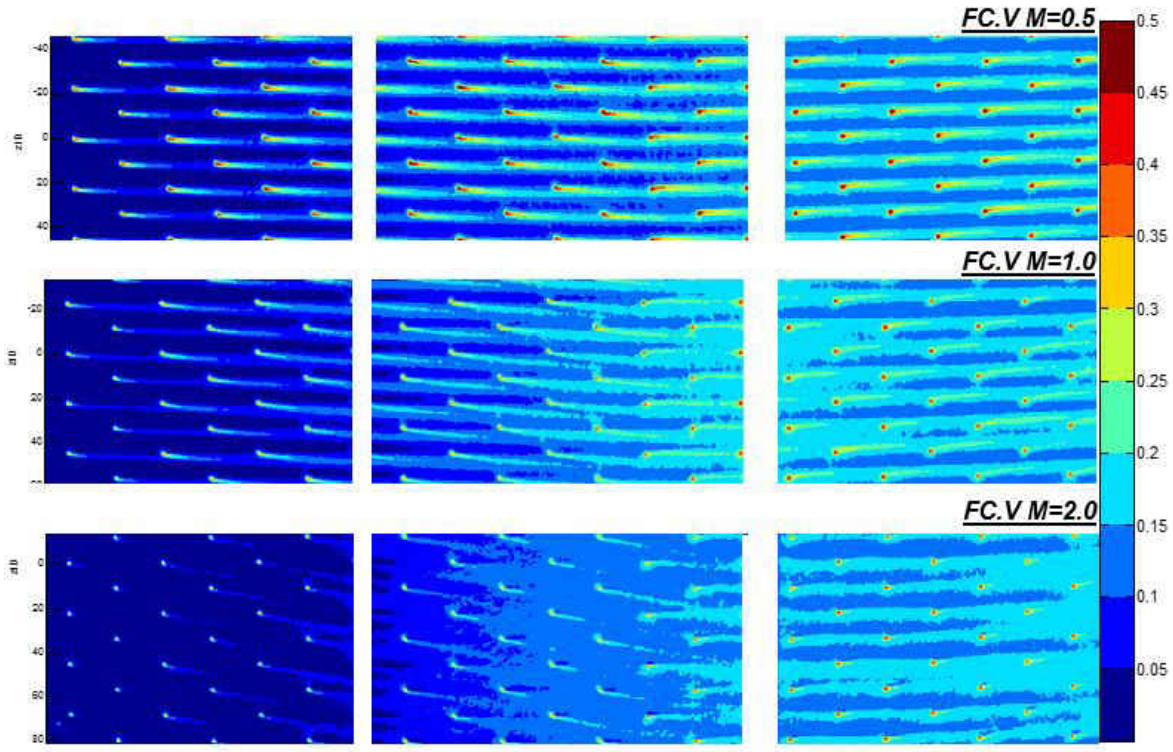

Figure 38: Adiabatic film cooling effectiveness (local data) for FC.V at all blowing ratios

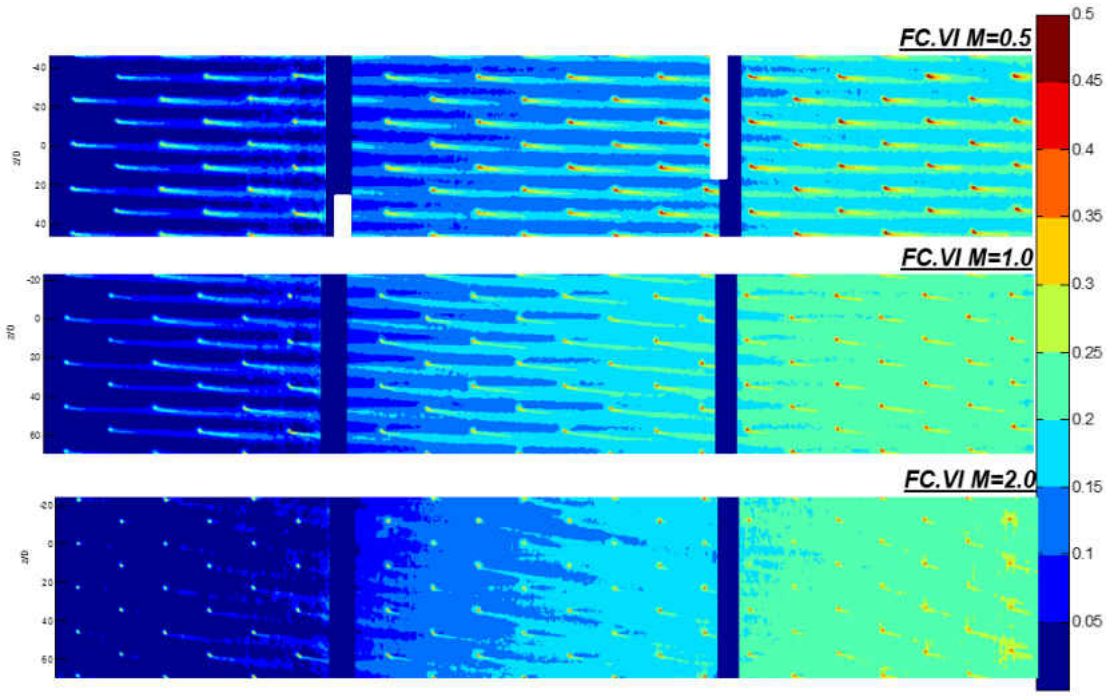

Figure 39: Adiabatic film cooling effectiveness (local data) for FC.VI at all blowing ratios

3.3 Laterally Averaged Film Cooling Effectiveness

The temperature matrix from the CCD camera images is processed as described in the Temperature Sensitive Paint section, and is assumed to be equivalent to the adiabatic wall temperature (failing the assumption negligibly due to the very low thermal conductivity of the Rohacell used). The film cooling effectiveness can be seen defined in Equation 19. The effectiveness is dependent on the coolant temperature (secondary flow) and the freestream temperature (primary flow). The placement of thermocouples for each measurement can be found in earlier sections of the report. In short, thermocouples for measuring these two temperatures were placed 'floating' in the plenum, on the backwall of the Rohacell (in the plenum), at the entrance to the film cooling holes (plenum side), within the film cooling holes, at the exit of the film cooling holes, on the surface of the TSP on the heat transfer surface, and far away from the heat transfer surface in the freestream of the wind tunnel. In

excess of 20 thermocouples was used and averaged to yield the freestream wind tunnel temperature and the coolant temperature. The laterally averaged expression of adiabatic film cooling effectiveness can be seen in Equation 20.

Equation 19: Film Cooling Effectiveness

$$\eta\left(\frac{x}{D},\frac{z}{D}\right)=\frac{T_{AW}\left(\frac{x}{D},\frac{z}{D}\right)-T_{\infty}}{T_{C}-T_{\infty}} \tag{19}$$

Equation 20: Laterally Averaged Film Cooling Effectiveness

$$\overline{\eta}\left(\frac{x}{D}\right)=\frac{1}{P}\int_{-P/2}^{P/2}\eta\left(\frac{x}{D},\frac{z}{D}\right)d\frac{z}{D} \tag{20}$$

Film cooling effectiveness data has been presented in the form of local contour images, however, in this section the result discussed will be the laterally averaged adiabatic film cooling effectiveness.

Laterally averaged measurements of film cooling effectiveness were taken for each full coverage film cooling geometry at M=0.5, 1.0, 1.5, and 2.0. Data was taken on the test surface with TSP, where the segmented test section was made up of three separate plates.

In order to readily compare film cooling performance of different geometries and blowing ratios, η was laterally averaged for each test case. The region of averaging was not the full width of the test surface, but rather only the portion that would best simulate the performance of an infinitely wide film cooling array. Local data was used to best discern what portion of the array would be used for lateral averaging. The region averaged for laterally averaged effectiveness varied between tests, but was always an integer multiple of the pitch, and was always as wide as possible.

In Figure 40, a sample local data image of effectiveness is shown, where the averaging window is approximately highlighted as dashed black lines. The bounds of the averaging window were always measured and carefully taken to be exactly half the lateral spacing between two holes, equally bisecting the space between two holes. Data inside the film cooling holes was not considered, the film cooling holes were not painted with TSP, as the intensity readings from measurements would be skewed due to the surface curvature. For each geometry, the full range of blowing ratios were tested between M=0.5 and M=2.0.

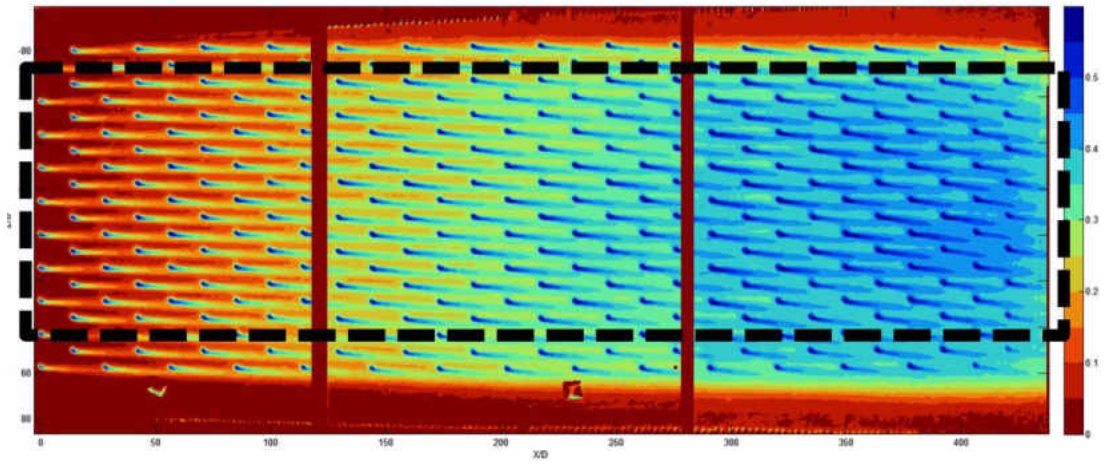

Figure 40: Sample data (from this work) with contours and the averaging window for laterally averaged effectiveness shown

3.3.1 FC.V

The FC.V adiabatic film cooling effectiveness can be seen in Figure 41. This geometry tested includes a compound angle shift mid-array. Noteworthy discussion can be directed to the expected how levels of coverage relative to the other cases. These relatively low values of coverage would be an inferior design to that with rows of shaped holes, for in cases where large thermal loads are locally present. Also, the M=2.0 case starts low and does not surpass any of the lower blowing ratio cases in effectiveness through the entire array, a trend that is slightly more pronounced here than in other geometries.

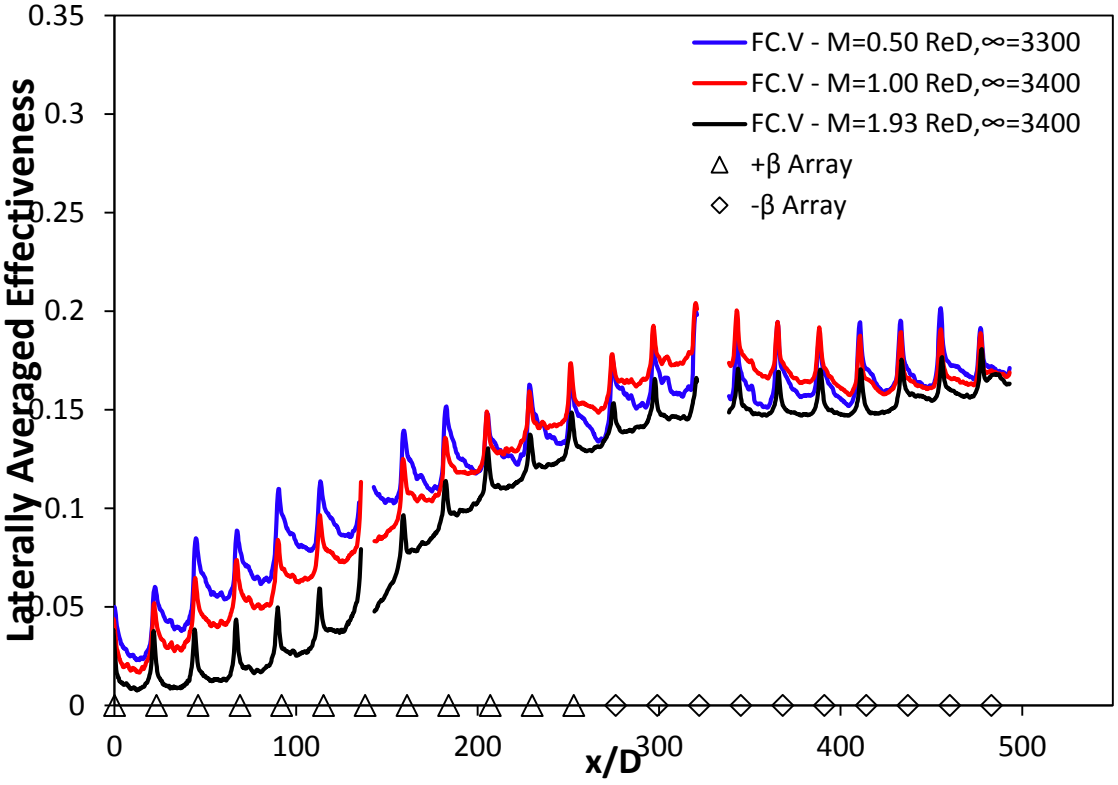

Figure 41: FC.V Adiabatic Film Cooling Effectiveness

Effectiveness testing was conducted at different freestream conditions (i.e. freestream velocity). As a result, two different Reynolds number, based on hole diameter, can be defined. Effectiveness results can be seen in , as the laterally averaged data is compared for each freestream velocity condition. The laterally averaged film effectiveness has a qualitatively similar trend with respect to the Reynolds number based on hole diameter and freestream velocity. As blowing ratio increases for each of the data sets, the Reynolds number dependence has less effect.

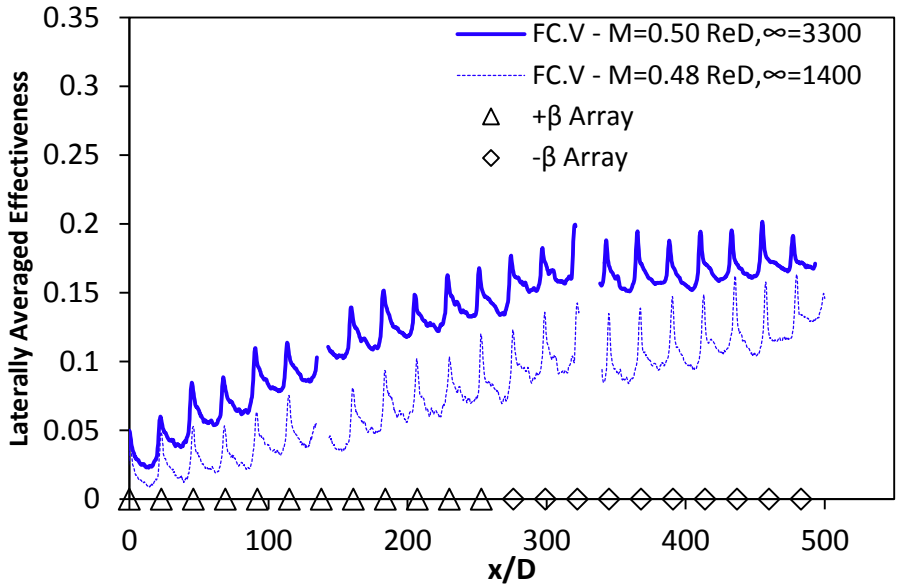

Figure 42: Comparison of effectiveness data for different freestream velocities, for FC.V, M=0.5

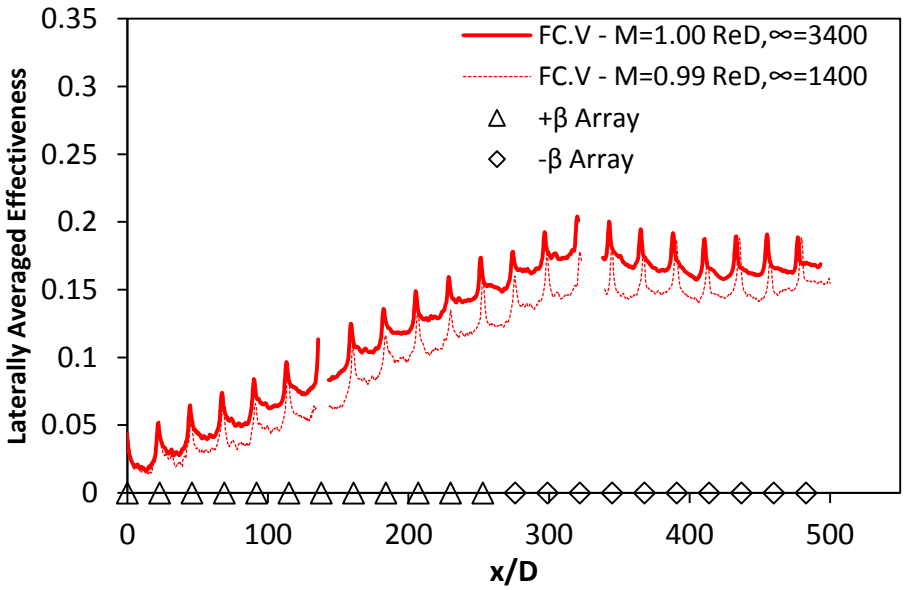

Figure 43: Comparison of effectiveness data for different freestream velocities, for FC.V, M=1.0

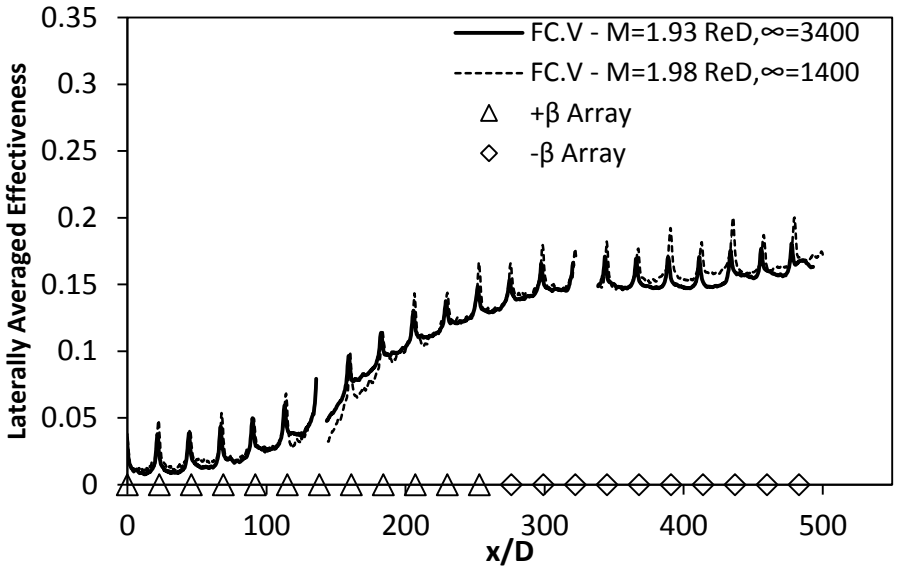

Figure 44: Comparison of effectiveness data for different freestream velocities, for FC.V, M=2.0

3.3.2 FC.VI

The FC.VI adiabatic film cooling effectiveness can be seen in Figure 45. This test specimen differs from FC.V due to FC.VI not having a compound angle shift present in the array. The impact of this is clear, as the cooling effectiveness downstream in the array continues to rise and does not plateau as compared. The effectiveness at the end of the array is considerably higher than for the cause without a compound angle shift. This conclusion that the compound angle shift is detrimental to the global (not local) performance in heat transfer is consistent with other tests in this study. Also, one can notice that the M=2.0 starts low in both the FC.V and FC.VI case, however, for the case without a compound angle shift the effectiveness continues to rise above the other cases, sufficiently far downstream.

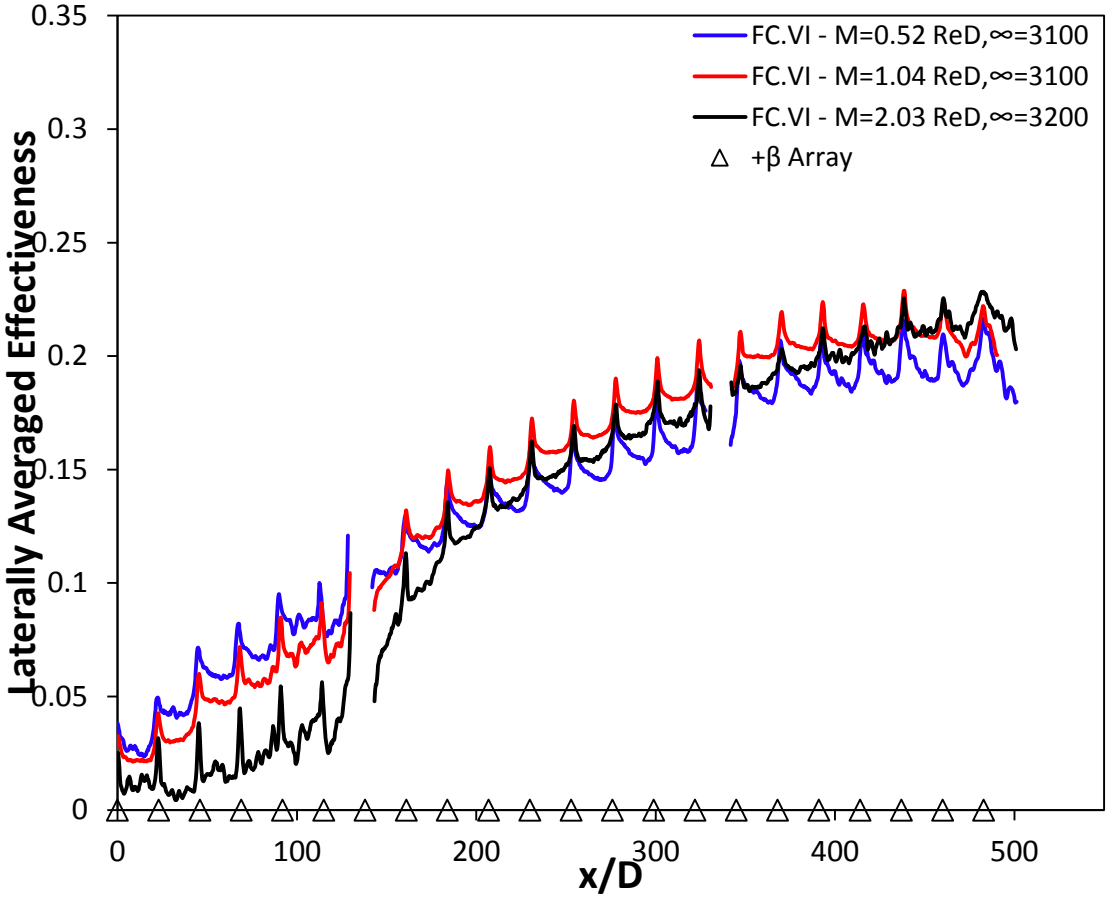

Figure 45: FC.VI Adiabatic Film Cooling Effectiveness

3.3.3 Direct Comparisons between Geometries

Several conclusions can be made when comparing FC.V and FC.VI, however, the largest conclusion is in regards to the compound angle change throughout the array. The compound angle shift can be locally helpful towards increasing the film effectiveness, by virtue of a large layer of film quickly accumulating around the holes of alternating compound angle. This aid to increasing effectiveness though does not persist downstream past the first row where the compound angle is shifted, as seen in the local effectiveness data. As in Figure 38 and Figure 39, one can see that jet coalescence is much less prevalent in the case where the compound angle shifts in the middle of the

array. These results are agreeable when looking to the laterally averaged film effectiveness results when analyzing the change in compound angle shift.

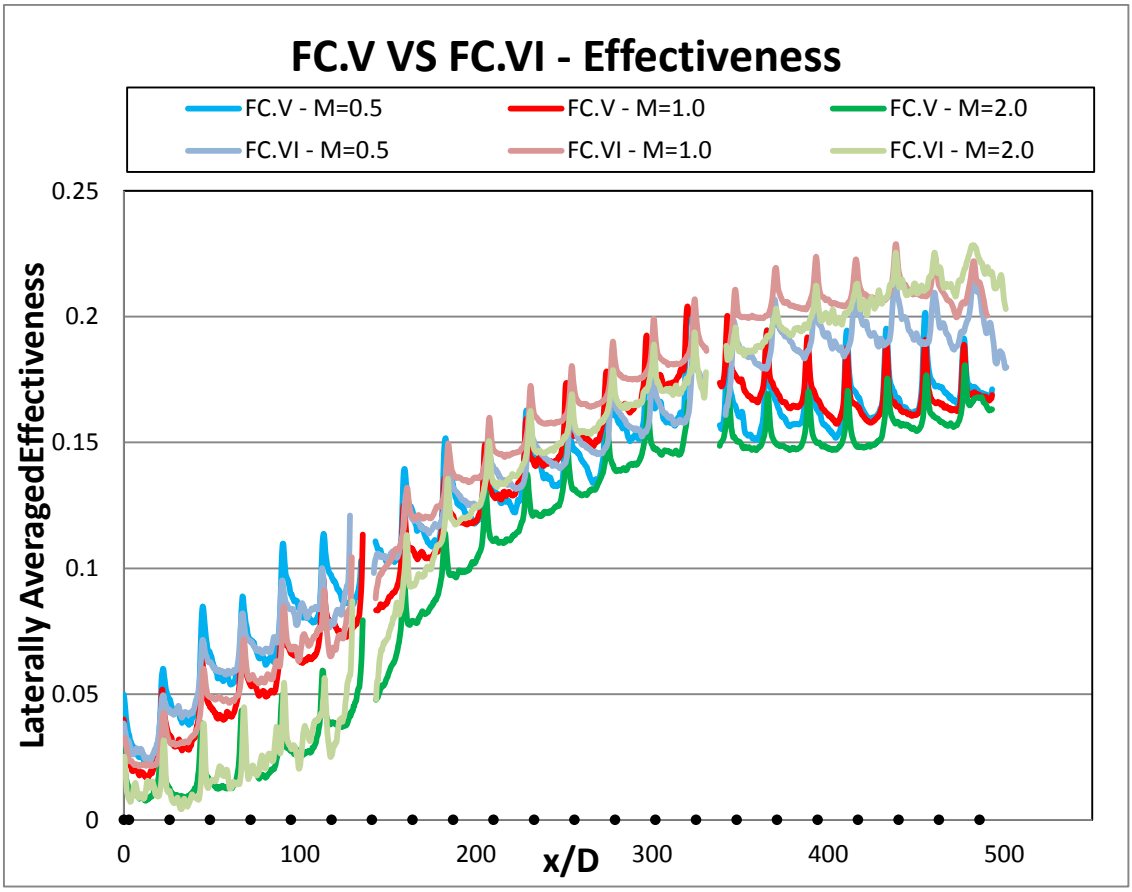

Figure 46: FC.V and FC.VI effectiveness compared for all blowing ratios

CHAPTER 4: HEAT TRANSFER AUGMENTATION RESULTS

4.1 Benchmark

The method of measuring heat transfer coefficient was validated in two ways: first, the method of determining h_0 was tested using a flat plate with alternating heated and adiabatic portions. The results of this, seen in Figure 47 and Figure 51, showed that the measured heat transfer coefficients were in good agreement to the h_0 prediction. This experiment also validated the method of calculating the heat transfer coefficient based on the electrical power input to the heaters.

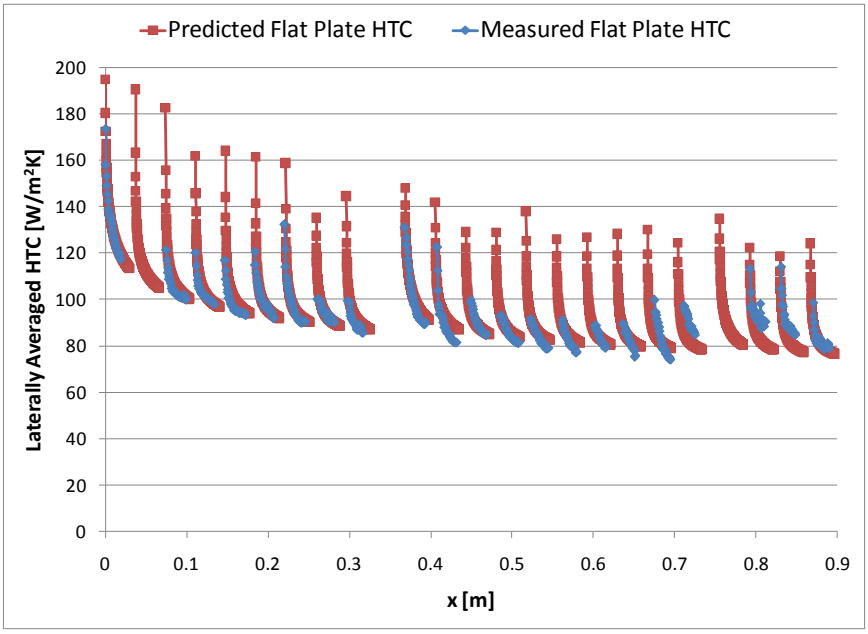

Figure 47: Flat plate h0 validation

Additionally, the film cooling geometry tested for validation was identical to the geometry used by Mayle [3] during heat transfer testing. The heat transfer enhancement results were compared directly to this publication data and showed good agreement, within the measurement

uncertainty of the experiment. A comparison of this work and Mayle's data for M = 0.5 is found in Figure 48, while M = 1.0 and M = 1.5 are found in Figure 49 and Figure 50, respectively.

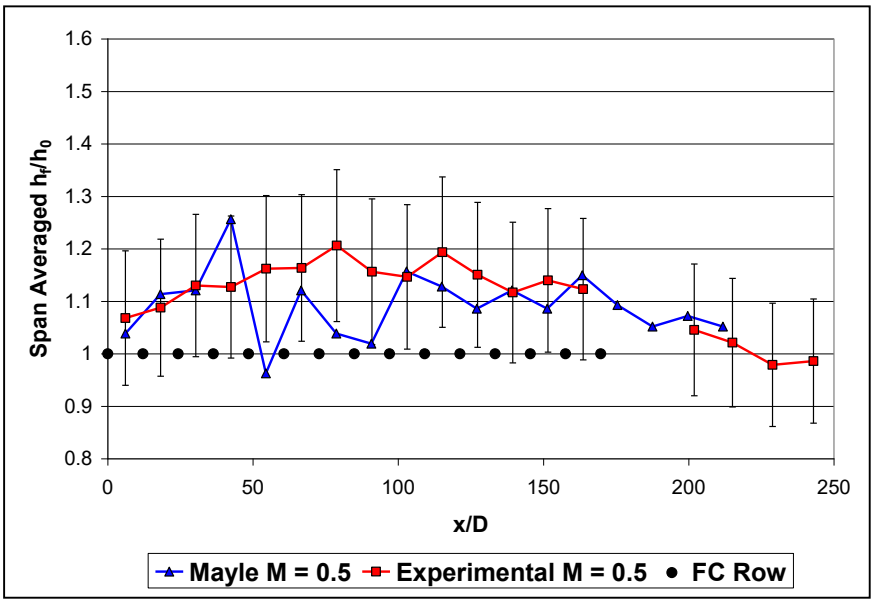

Figure 48: Validation of the M=0.5 case with (identical geometry) Mayle [3]

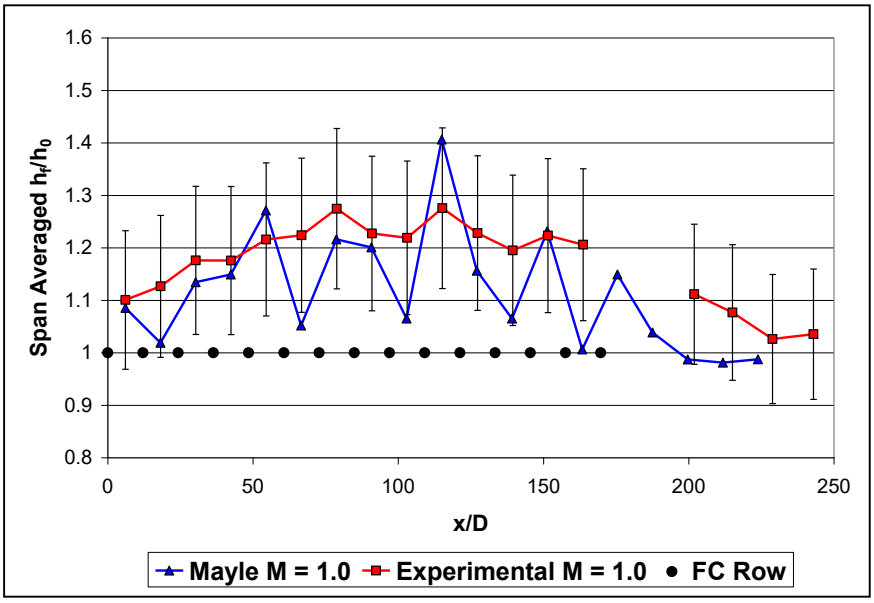

Figure 49: Validation of the M=1.0 case with (identical geometry) Mayle [3]

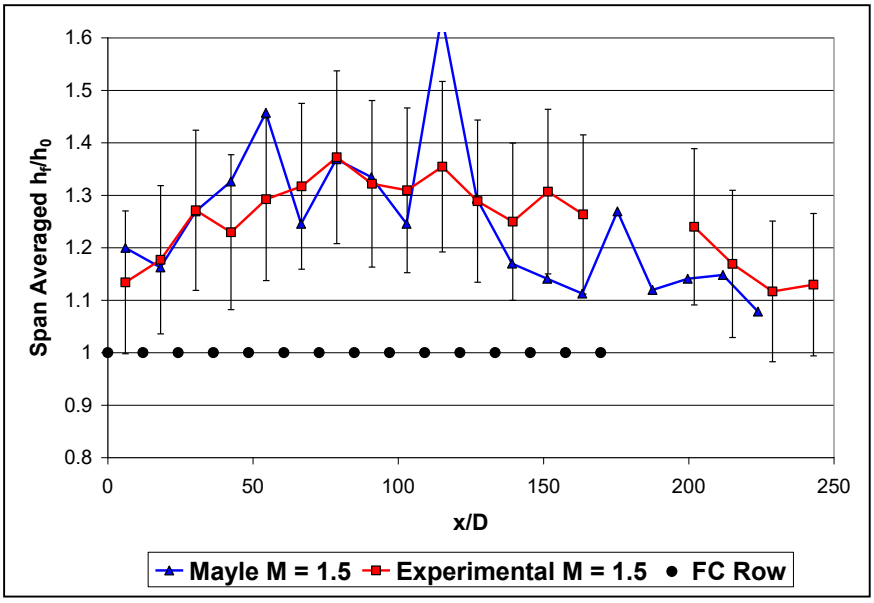

Figure 50: Validation of the M=1.5 case with (identical geometry) Mayle [3]

Figure 51 shows additional validation work that was conducted prior to heat transfer coefficient testing. Uncorrected heat transfer coefficient measurements over a flat plate without film injection was measured over 6 heaters, as opposed to Figure 47, and heater spacing was identical to that in the test matrix. The streamwise origin is equal to 20 cm, where two coordinate systems were used. One is the virtual origin of the hydrodynamic boundary layer, the other is the first row of holes. The distance between the two is x_0. The augmentation values are within 1+/- 0.1, and experimental uncertainty of 14%. Also, a slight 2D effect was present at the trailing edge of heater strips (due to an apparent increase in HTC at trailing edge, implying a lower temperature, a result of 2D conduction).

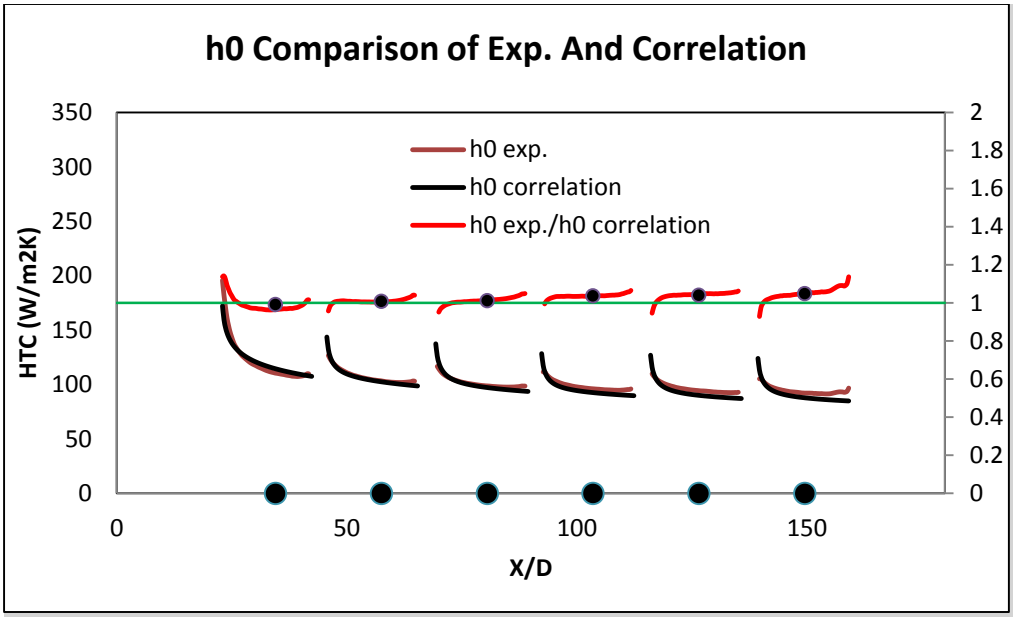

Figure 51: h0 testing, comparing of experiment and correlation

4.2 Local Heat Transfer Augmentation

Local heat transfer augmentation data plots are shown in this section, which will be followed by quantitative comparisons. New experimental practices have been implemented throughout the development and preparation of this study, to ensure high quality local heat transfer data. More specifically, methods of preparing and installing the test sections to maintain smooth surfaces and test specimen integrity, use of high quality plates and heaters to increase temperatures and reduce uncertainties, and other such test preparation practices. Improvements to the data processing techniques have also been made, such as using curve fits for backside temperature, changing resistance as a function of temperature, and other similar changes.

Figure 52 shows local heat transfer augmentation data for all blowing ratios of the FC.VI test specimen. From the lowest blowing ratio case, the jets remain very distinct and have not coalesced, almost completely independent of one another. There is no signs of flow detachment due to heater strips poorly adhered to the heat transfer surface. This effect is seen to disappear at

higher blowing ratios though however, especially when comparing the jets distinct and independent nature at low x/D over the heater strips. Even at large x/D the jets seem to be separated for the M=0.50 case. Another interesting observation is that increasing the blowing ratio results in a direct increase in heat transfer augmentation, as compared with effectiveness heat transfer data, where some of the increases in blowing ratio results in only marginal increases in effectiveness. However, the heat transfer augmentation data does qualitatively look to the effectiveness data, since the effectiveness profile is used to correct for the film temperature.

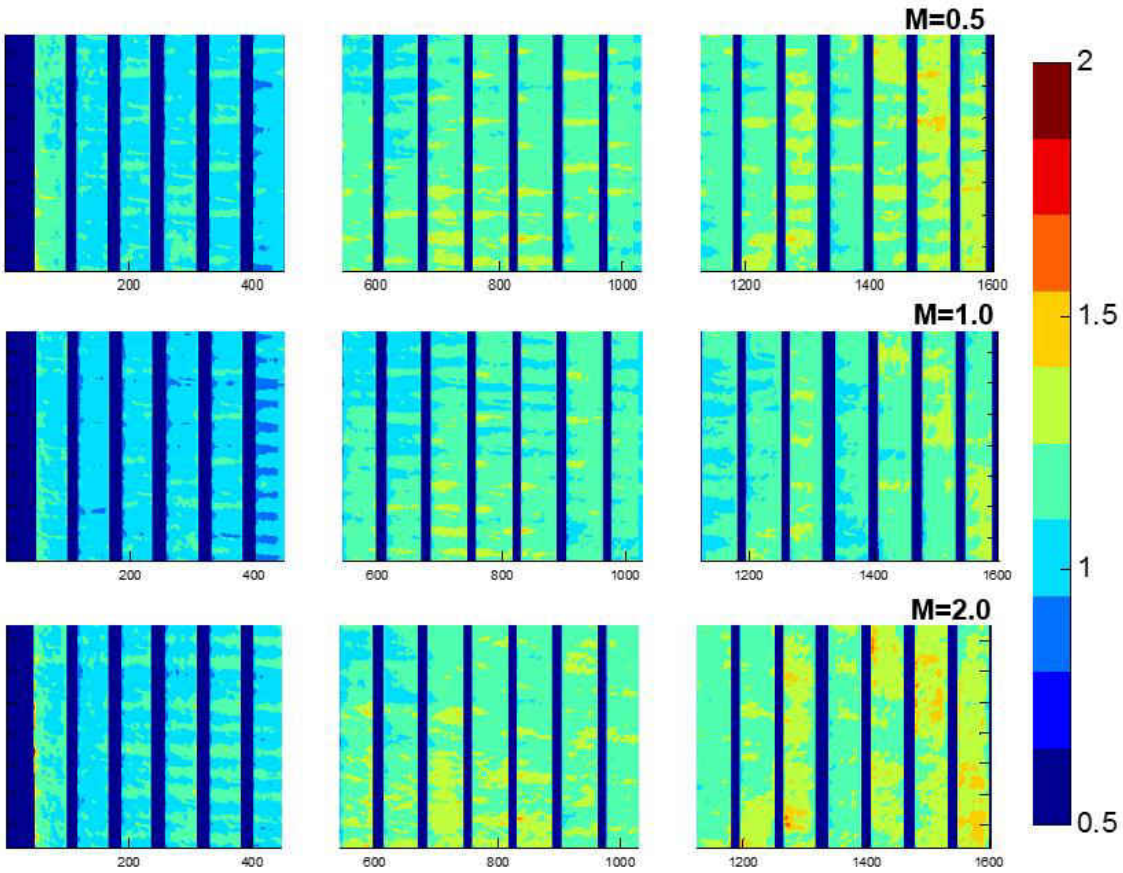

Figure 52: Local HTC augmentation values for FC.VI at all blowing ratios

4.3 Span Average Heat Transfer Augmentation

4.3.1 FC.VI

Span average plots for heat transfer augmentation are presented here for all blowing ratios of the FC.VI specimen, as in Figures Figure 53 through Figure 55. The defining features for this geometry is the absence of a compound angle shift in the array geometry. Contrary to previous cases, this array shows that the heat transfer coefficient augmentation shows little or no dependence on the blowing ratio. The heat transfer coefficient augmentation increases down the array in a nearly linear fashion. Average augmentation to the heat transfer coefficient over the array for the M=0.5, 1.0, and 1.5 cases is 1.15, 1.11, and 1.18, respectively.

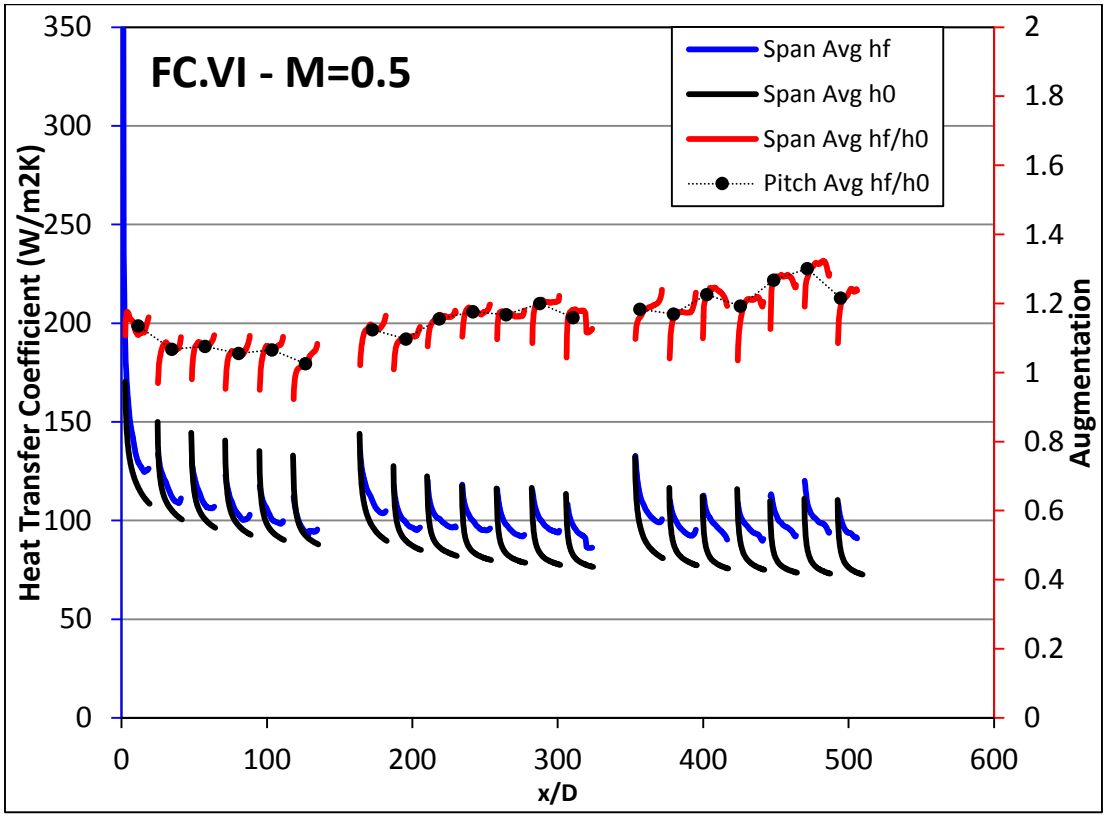

Figure 53: FC.VI heat transfer data for M=0.50

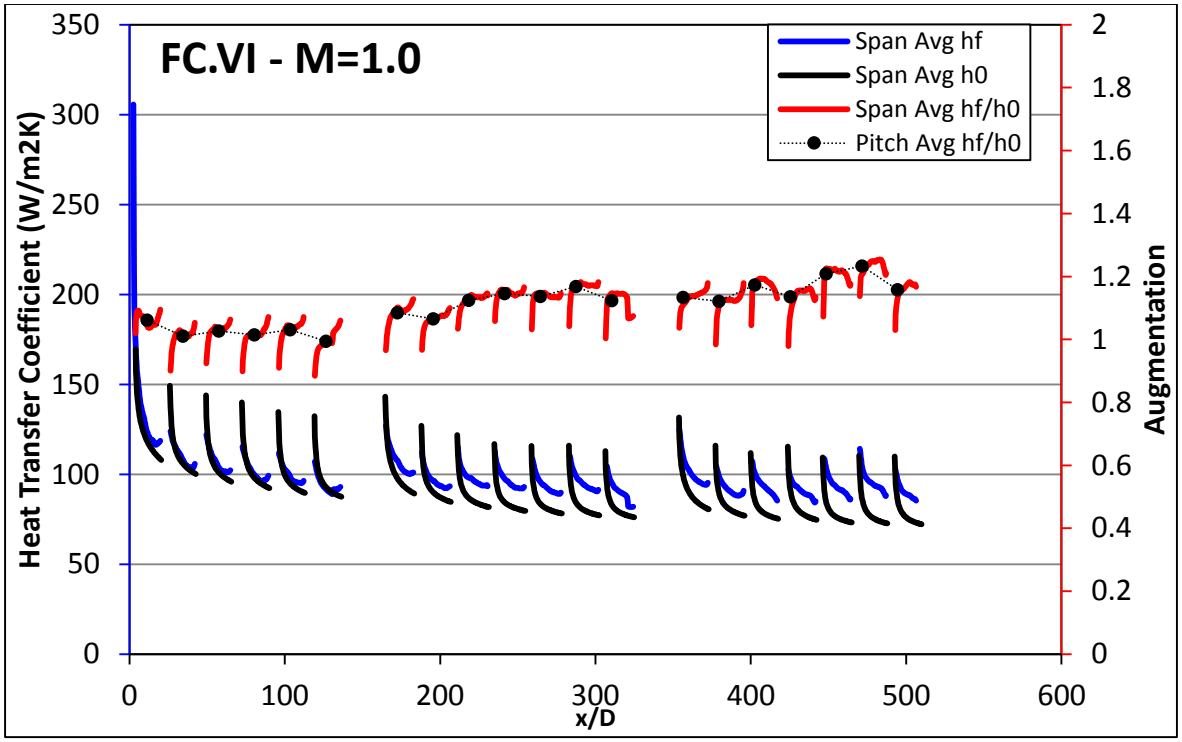

Figure 54: FC.VI heat transfer data for M=1.0

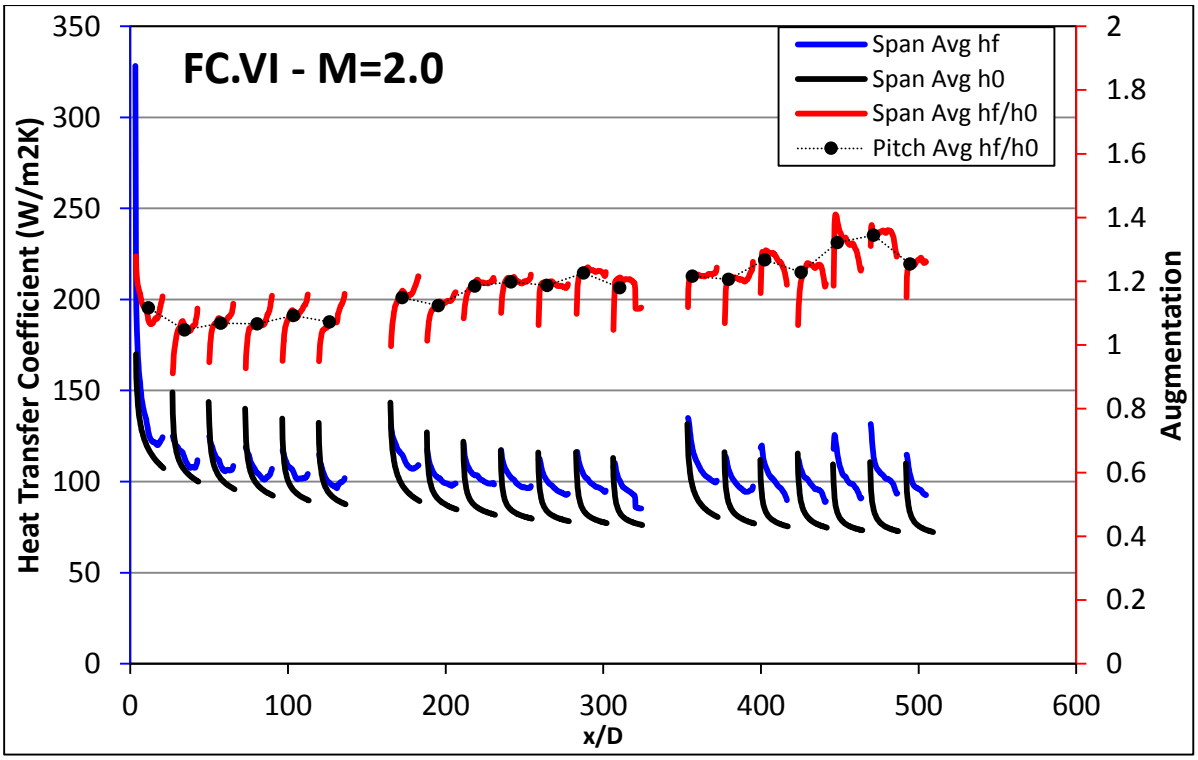

Figure 55: FC.VI heat transfer data for M=2.0

CHAPTER 5: COMPUTATIONAL EFFORTS

5.1 Fluid Domain

5.1.1 Geometry

Figure 56 shows the computational fluid domain. The geometry of choice is the fluid volume in a wind tunnel experiment of a flat plate with an array of cooling holes. Figure 57 and Figure 58show the different orientation of the array within the computational domain.

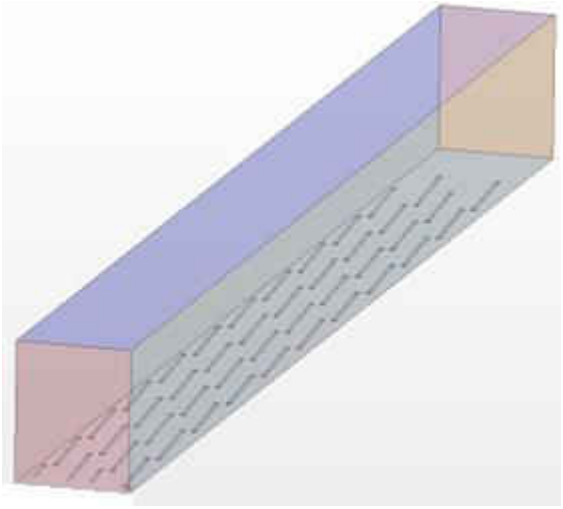

Figure 56: Isometric view of the fluid domain

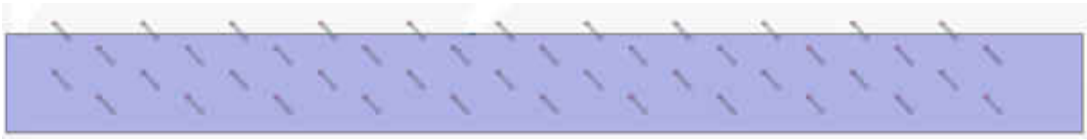

Figure 57: Top view of geometry

Figure 58: Side view of geometry

This model was specifically setup in an effort to match the experimental data, as it is by comparing the results of the simulation to the experimental data that we will judge the success of the model. Although the geometry length matches the experiment in the streamwise direction, the width has been reduced so that the full array of holes in the transverse direction are not included in the domain. Essentially, the fluid domain represented here is a thin slice out of the wider geometry of the experiment. In order to ensure a reasonable comparison of the simulation results with experimental data, boundary conditions will be set to mimic this repeating pattern in the transverse direction. This periodic boundary condition is used to greatly reduce the computational resources required to obtain a solution, while not affecting the predictions in film cooling performance for an infinite array of holes.

Within STAR-CCM+, boundary conditions are defined for each boundary surface within the region in the simulation. Specifically defined are the crossflow inlet and exit, the top "wall" (outside the boundary layer), the heat transfer surface, the left and right lateral wall, the inlet to the each film cooling hole, and the walls of each film cooling hole.

Table **6** shows the boundary condition type assigned to each boundary of the fluid domain, with some sample quantities in place, which were used for the FC.VI M=1.0 case tested. The boundary conditions for this simulation will be covered in much more detail in later sections of this report.

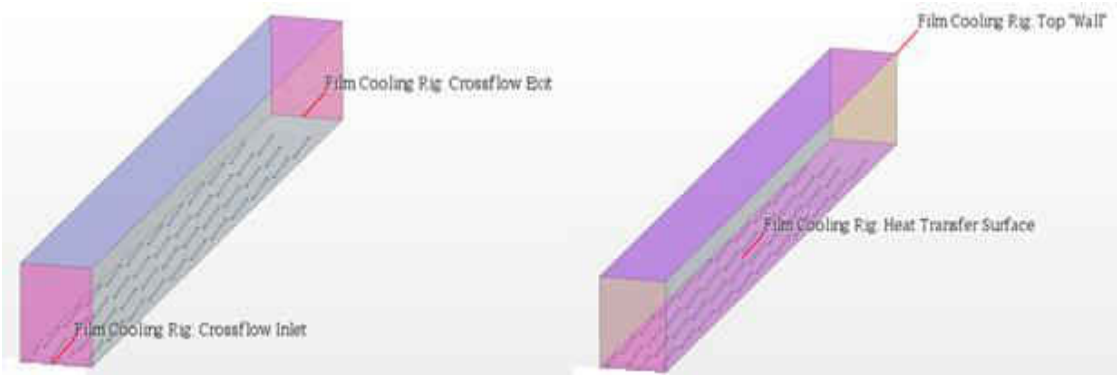

Figure 59: Region defined for fluid domain

Table 6: Sample quantities used for FC.VI, M=1 computation

Boundary	Boundary Condition Details
Crossflow Inlet	Velocity Inlet to Match Exp. Data $U_\infty = 26$ m/s $T_\infty = 300$ K $TI_\infty = 0.7\%$ $\Lambda_I = 0.3$ m (Exp. Calculated)
Crossflow Outlet	Pressure Outlet
Spanwise Walls	Periodic
Top Wall	Symmetry (Gradients approach zero)
Bottom Wall	No slip, adiabatic, impermeable
Wetted Wall Inside Film Holes	No slip, adiabatic, impermeable
Inlet to Film Holes	Velocity Inlet $U_{hole} = \frac{M}{DR} * U_\infty * \cos(\alpha)$ $V_{hole} = \frac{M}{DR} * U_\infty * \sin(\alpha)$ $W_{hole} = \frac{M}{DR} * U_\infty * \sin(\beta)$ $T_{Static} = 325$ K TI=1% $\Lambda_I = 0.00206$ m (hole diameter)

5.2 Mesh

Many issues with a volumetric mesh can be traced back to a poor surface mesh. In order to improve the initial surface mesh and help produce a good volumetric mesh for the model, it is wise to choose the surface remesher option within STAR-CCM+. The surface remesher is recommended by STAR-CCM+ always prior to volume meshing.

A polyhedral mesher is used to populate the volume of the fluid domain. It uses an arbitrary polyhedral cell shape with an average of 14 cell faces to build the core mesh. The polyhedral mesh is considered to produce more accurate results than other mesh types available, but it requires additional memory and time for the solution to converge.

The prism layer mesher is used to generate orthogonal prismatic cells near wall surfaces and boundaries, which improves near wall flow solutions. As the main area of interest for this simulation is near the heat transfer wall, the prism layer mesher is ideal to use to ensure accurate heat transfer results along the surface.

Standard industry practice typically requires a sufficiently small y^+ value (<5) to properly resolve the boundary layer and heat transfer. A properly conditioned group of prism layer cells is essential in heat transfer studies, as computing heat transfer near walls is a procedure that begins and relies on standard wall functions (e.g. law of the wall, boundary layer theory, user specified, etc.). This computational study utilized up to 30 prism layers in critical regions, such as where the coolant jets were introduced. A full list of the details of the mesh can be seen in Table 7.

The mesh generated had cells of variable size in order to reduce computational expenses and retain higher fidelity in regions of most interest. The scheme implemented refined meshing around the hole several diameters downstream and normal to the surface in order to obtain proper accuracy in the highly turbulent region. A coarser mesh is applied progressively

downstream up to the next row of holes and upwards into the free-stream. Figure 60 shows the transition into a coarse mesh in the free-stream, while Figure 61 shows the recursive pattern in the streamwise direction.

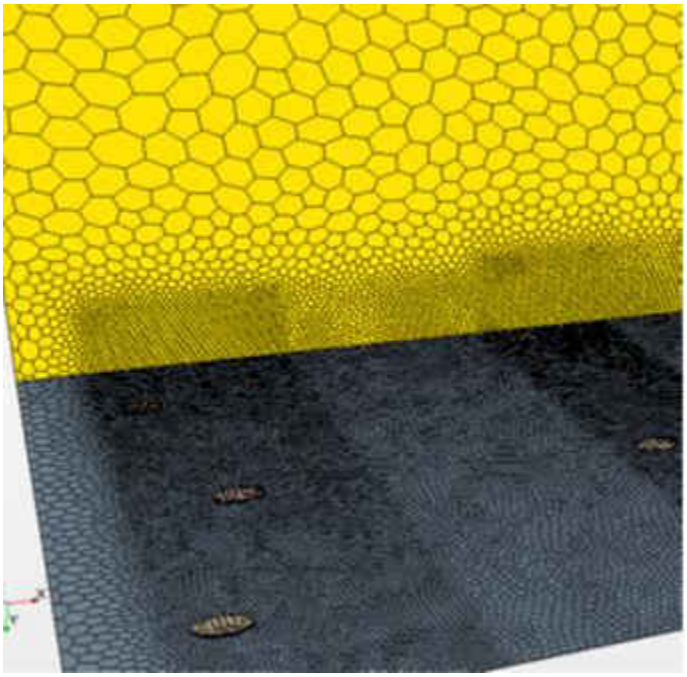

Figure 60: Fluid domain showing mesh transition from fine near heat transfer surface to coarse in free-stream

Figure 61: Domain showing recursive pattern of fine and coarse mesh in streamwise direction

To generate the mesh, blocks were made and stacked one after the other in the streamwise direction. Each block occupied the full lateral space in the domain with a height that ranged from 6-10 hole diameters tall so that it would completely encompass the interaction of the jet in crossflow. Initial simulations and correlations were utilized for determining the most appropriate height of the blocks, such that all coolant jet interactions with the mainstream could be captured. Figure 62 shows the blocks directly over the holes as well as the filler blocks located between each row of holes.

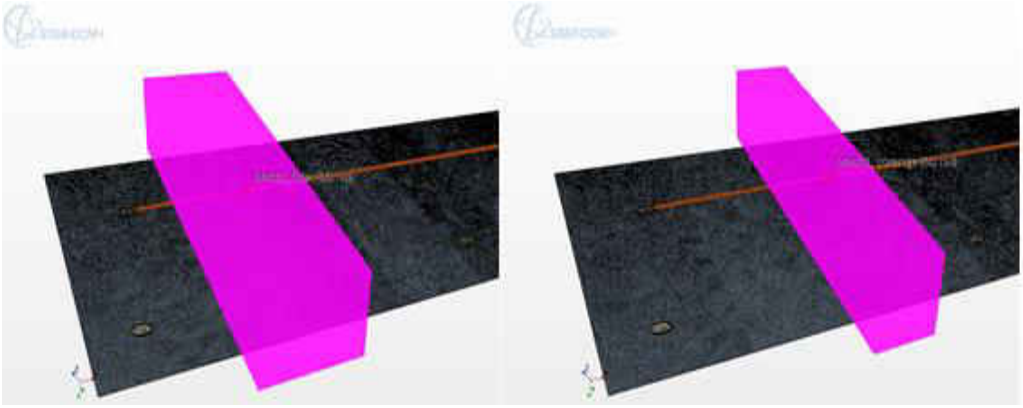

Figure 62: Image on left shows filler block located between rows of holes, and image on right shows block located directly above holes

The blocks located over the holes were assigned specific settings, as were the filler blocks located between each row of holes. The remaining volume of the computational domain was meshed with its own separate settings. The full list of values for all three sections are located in Table 7 which includes the mesh base size, number of prism layers, prism layer stretching, and prism layer thickness.

Table 7: Mesh settings

Blocks Located between Rows of Holes	
Base Size	15% (.00075 m)
Number of Prism Layers	30
Prism Layer Stretching	1.1
Prism Layer Thickness	5% (0.00025 m)
Blocks Located Immediately Above Holes	
Base Size	12% (.0006 m)
Number of Prism Layers	30
Prism Layer Stretching	1.1
Prism Layer Thickness	5% (0.00025 m)
Remaining Volume of the Computational Domain	
Base Size	0.005 m
Number of Prism Layers	4
Prism Layer Stretching	1.5
Prism Layer Thickness	33% (0.001665 m)

Before running the simulation, the first check was to the validity and quality of the volume mesh. A java script was written and implemented to generate mesh plots and scenes, to evaluate the quality of the mesh within the computational domain after each mesh iteration. It was also important to search through the domain to ocularly search for regions where poorly conditioned cells exist. Such cells may exist between different meshing regions, sharp transitions in the geometry (e.g. from the film cooling hole to the heat transfer surface), and need to be addressed individually in order to prevent and difficulty in proper computation. The four metrics chosen to assess the mesh are cell quality, skewness angle, volume change, and wall y+ values.

The cell quality metric is based on a hybrid of the Gauss and least-squares methods for cell gradient calculations. It is a function of both the distribution of cell centroids of a cell to its

neighbors and the orientation of the cell faces. Cells of good quality are highly orthogonal, such as a cubic cell, and have a cell quality of 1.0. Poor quality cells, such as a flat cell, have a cell quality metric approaching zero and will likely negatively impact the accuracy of the solution. Figure 63and Figure 64 show a visual representation of the cell quality in the fluid domain.

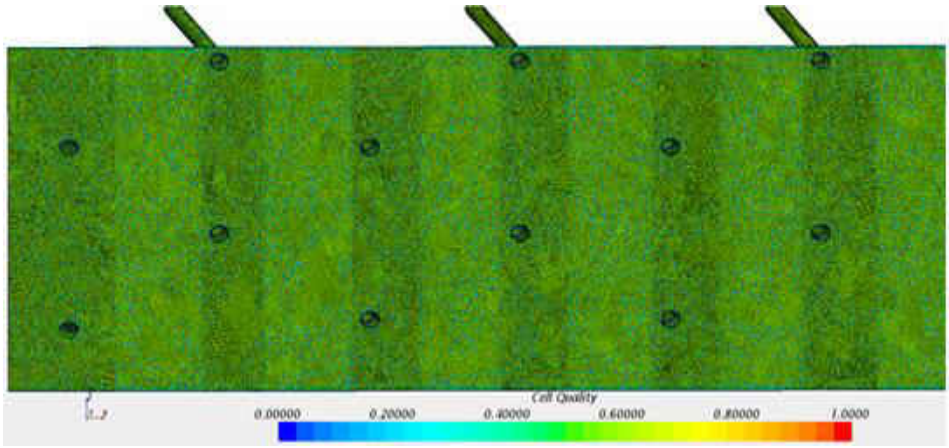

Figure 63: Cell quality over the heat transfer surface (from 0 to 1)

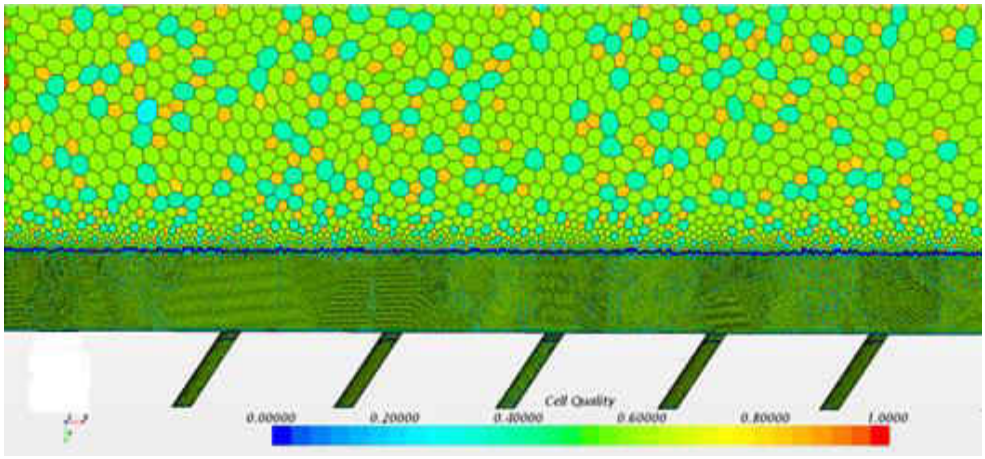

Figure 64: Cell quality over wall normal plane to heat transfer surface (from 0 to 1)

Figure 65 shows a histogram for the cell quality metric. It demonstrates that in the volume mesh, the vast majority of cells have a cell quality metric of close to the perfect value of 1.0. Most importantly, it shows that there is no significant number of degenerate cells in the volume.

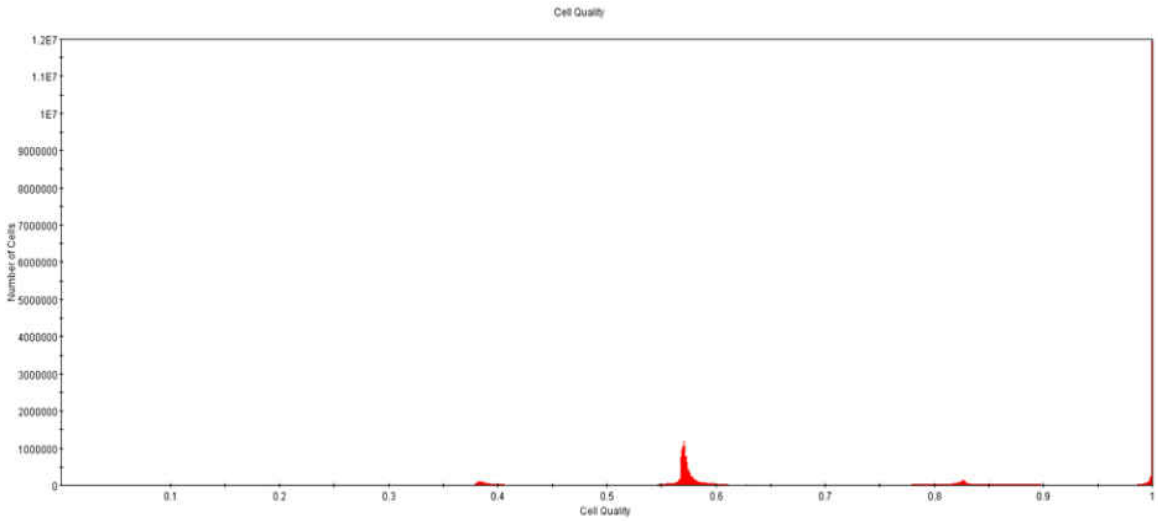

Figure 65: Histogram of cell quality (quality ranging from 0 to 1, and number of cells ranging from 10^6 to $1.2*10^7$)

The skewness angle is the angle between the face normal vector of two neighboring cells and the vector that connects those cell's centroids. A perfectly orthogonal mesh would have a skewness angle of 0˚, while a concave cell would have an angle greater the 90˚. Skewness angles of 90˚ or greater lead to problems with the solver due to the use of the dot product of these two vectors in the denominator of the diffusion term formulation for transported variables. In this case quantities become unbounded and inaccuracies are introduced into the solution. Ideally skewness angles greater than 85˚ should be avoided. Figure 66 shows that the overwhelming majority of cells in the mesh that are well below the 85˚ threshold, indicating a good quality mesh.

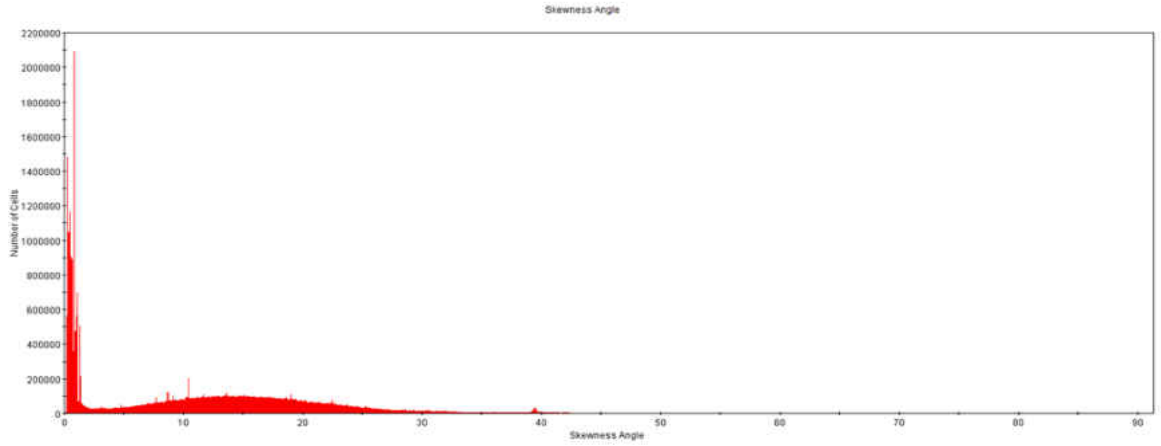

Figure 66: Histogram of skewness angle (skewness angle from 0 to 90, number of cells from $2*10^6$ to $22*10^6$)

The volume change metric represents the ratio of the volume of one cell to its largest neighboring cell. Large changes in volume from one cell to the next can cause inaccuracies and instability in the solvers. A volume change value of 1.0 is ideal, indicating a cell has an equal or higher volume then its neighboring cells. Values less than 0.01 are a typical indicator of poor quality cells and may need to be addressed. Figure 67 shows that most cells in the computational domain have an acceptable volume change value. Although some cells fall below the established threshold, they are relatively few in number and special care was taken to ensure that they occur only in areas that are not of interest for our simulation.

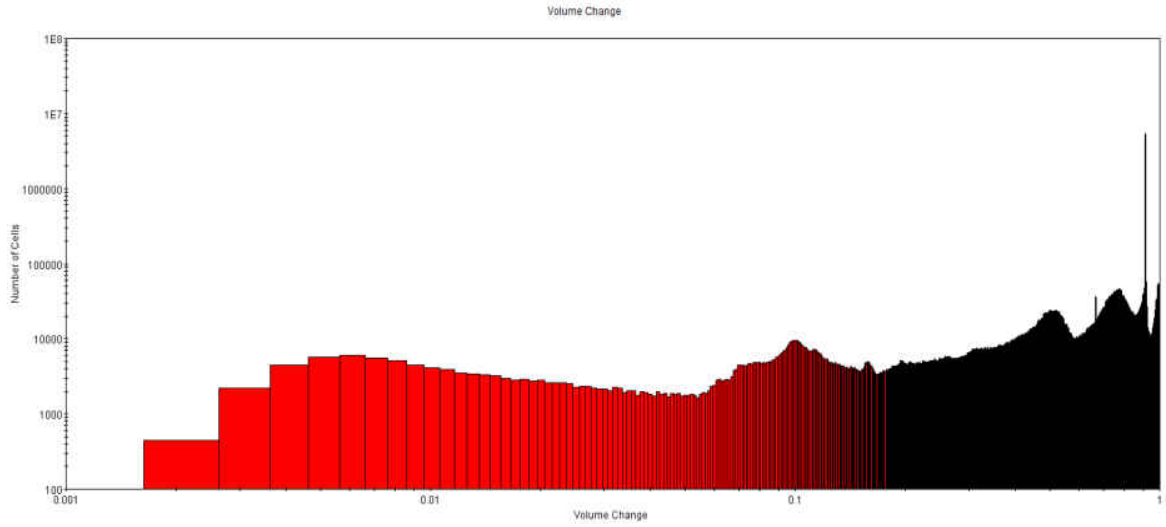

Figure 67: Histogram of volume change metric (volume change from 0.001 to 1, number of cells from 100 to $1*10^8$)

A check the y+ value was also done for the first grid point along the heat transfer surface (nearest to the wall). If the wall y+ value is too large, it will fall outside of the boundary layer or outside the viscous sub layer region, and the simulation may not correctly calculate flow properties at this location and then introduce errors into the results. Standard industry practice suggest that for accurate results an ideal wall y+ value should be less than 5. As can be seen in Figure 68, the y+ values for our heat transfer surface are sufficiently low enough to suggest accurate results.

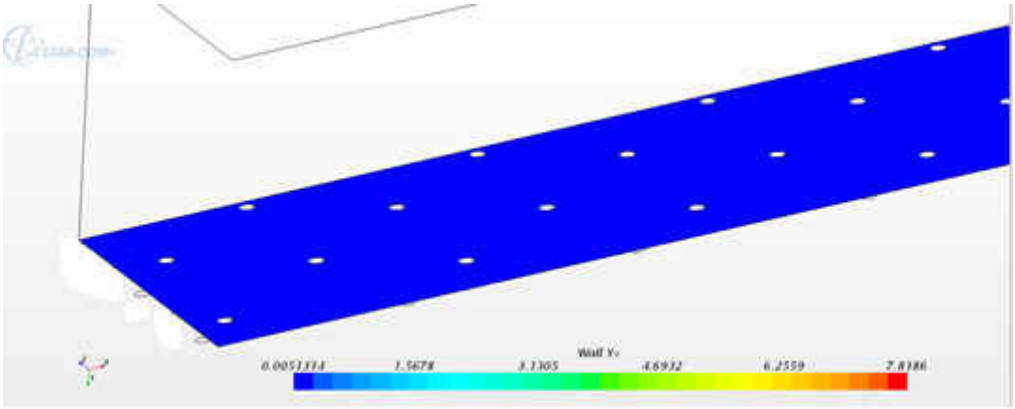

Figure 68: Wall y+ value distribution on the heat transfer surface

5.3 Boundary Conditions

For the top "wall" of the fluid domain, a symmetry plane boundary is applied. The solution obtained in this manor is the same as if the fluid domain was mirrored about that plane. The gradient across a symmetry plane is zero, which makes it appropriate to use in this simulation, as free stream flow is expected at this height away from the heat transfer surface.

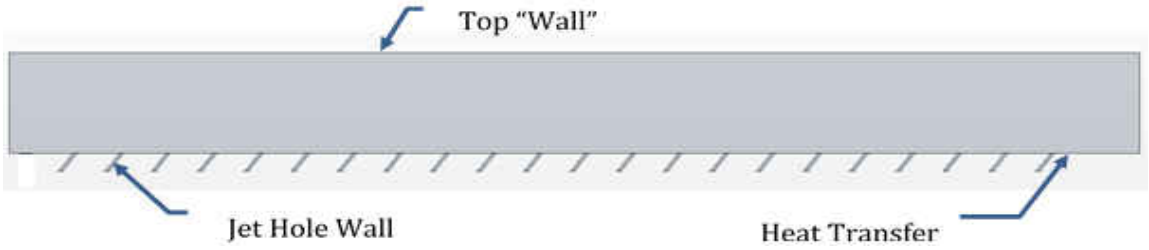

Figure 69: Side view of fluid domain indicating location of the select boundaries

Along the heat transfer surface wall and wall boundary is applied. These are impermeable walls, and the shear stress specification was set to no-slip. The surfaces were considered smooth and adiabatic. In experiments, these walls are not truly adiabatic, but it is a common assumption to make in evaluating film cooling effectiveness. However, for this experiment, a specialty grade of insulation (Rohacell) was used with an extremely low thermal conductivity to closely mimic an adiabatic wall.

All the jet hole inlets are specified as velocity inlets, where the exact values will match the experimental work that this simulation was intended to replicate. As in Table 8, the velocity components were specified in the simulation based on the measured blowing ratios of the testing conditions. Because local pressure measurements were made throughout the array from within the plenum, specific pressure and temperature boundary conditions could be prescribed at almost every row of holes within the simulation. The turbulence is specified by intensity and length scale,

where the length scale value chosen matches the jet hole diameter. The main array holes are broken up into three sections, each with a different static temperature value at their respective inlets. The exact values used for hole boundary conditions are found in the following tables. Table 8 shows the location of the three main array hole sections.

Table 8: Tabulated quantities for boundary conditions

Main Array Holes 1-12	
Static Temperature (K)	340.05
Turbulence Intensity	0.01
Turbulent Length Scale (m)	0.0021
Velocity (m/s)	[0.0, -14.5997, -25.2874]

Main Array Holes 13-28	
Static Temperature (K)	342.55
Turbulence Intensity	0.01
Turbulent Length Scale (m)	0.0021
Velocity (m/s)	[0.0, -14.5997, -25.2874]

Main Array Holes 29-44	
Static Temperature (K)	333.65
Turbulence Intensity	0.01
Turbulent Length Scale (m)	0.0021
Velocity (m/s)	[0.0, -14.5997, -25.2874]

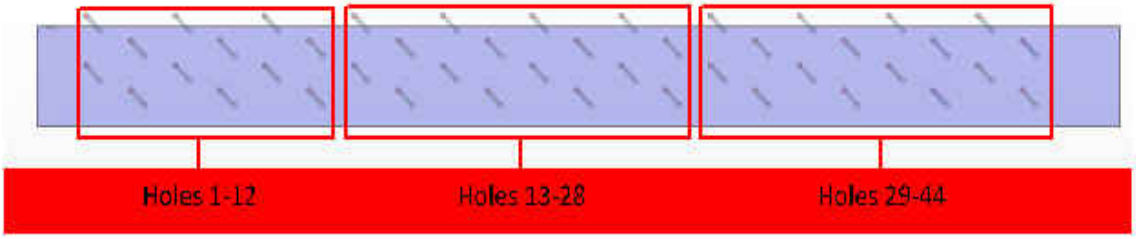

Figure 70: Top view of domain with location of hole sections highlighted

Similarly, the crossflow inlet is also set as a velocity inlet, with values prescribed to match the thorough boundary layer characterization that was performed experimentally. More thorough

information on the boundary layer characterization can be found in previous sections of this report. The turbulent length scale is set as approximately 10% of the fluid domain inlet height. Unlike the hole inlets, where velocity was assumed as uniform, the crossflow inlet is set to match a known velocity profile. A user defined field function is set within the program to replicate this profile, and the boundary condition uses this function to set the inlet velocity. The boundary layer profile was specified in STAR-CCM+ with three piecewise functions, in order to minimize any error in curve fitting the experimental data.

Table 9: Crossflow inlet quantities for boundary condition specification

Crossflow Inlet	
Static Temperature (K)	300
Turbulence Intensity	0.01
Turbulent Length Scale (m)	0.01
Velocity (m/s)	User defined field function

The crossflow exit is specified as a pressure outlet, where the experimental testing provided static pressure values all throughout the array, including at the very trailing edge. The pressure is set as per the experimental set up, and the turbulence is once again defined by intensity and length scale. Since the mass flow rate and temperature entering the domain through the crossflow inlet and the hole inlets is known, a mass weighted average is used to provide a value for the temperature at the exit. The specific values are located in the following table.

Table 10: Crossflow exit quantities for boundary condition specification

Crossflow Exit	
Pressure (Pa)	-764.5
Static Temperature (K)	302.15
Turbulence Intensity	0.08
Turbulent Length Scale (m)	0.0255

As mentioned previously, the simulation geometry did not contain the entire array of jets, as in the experiment. This pattern of holes repeats in the direction perpendicular to the crossflow (lateral). The decision to not include the full array of holes in the lateral direction was made to improve the computational efficiency of the simulation, since a finer mesh can be applied to the smaller fluid domain. To simulate this repeating geometry, a periodic interface is set along the lateral walls. The interface represents a repeat of information across the boundaries, so fluxes that cross one boundary are tabulated and applied to the other identically. To set this boundary condition, the lateral walls are first defined as walls like the heat transfer surface. Then, an internal interface is applied to both lateral wall regions with periodic topology. When using a periodic interface, a conformal mesh is produced on both sides of the interface so that the vertex locations and face topologies match identically. This is necessary because essentially all that the periodic interface does it take one value at one wall, and push it across the interface to the appropriate cell, thus requiring an identical set of cells.

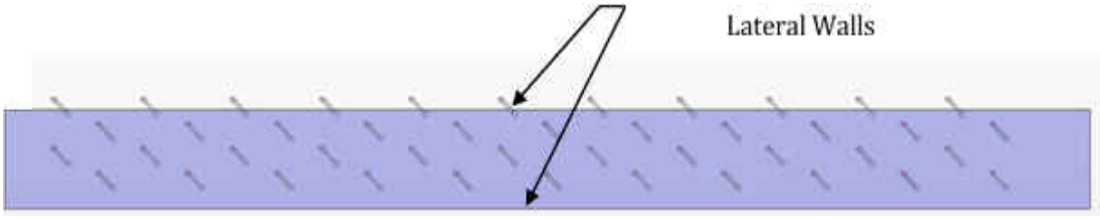

Figure 71: Top view of domain showing location of internal interface for periodic boundary condition

5.4 Generic Physics Models

In this part of the report, some of the main modules of the software used for prescribing the physics in the continuum will be discussed. Figure 72 illustrates the physics models used in the simulation, as seen from the STAR-CCM+ simulation tree.

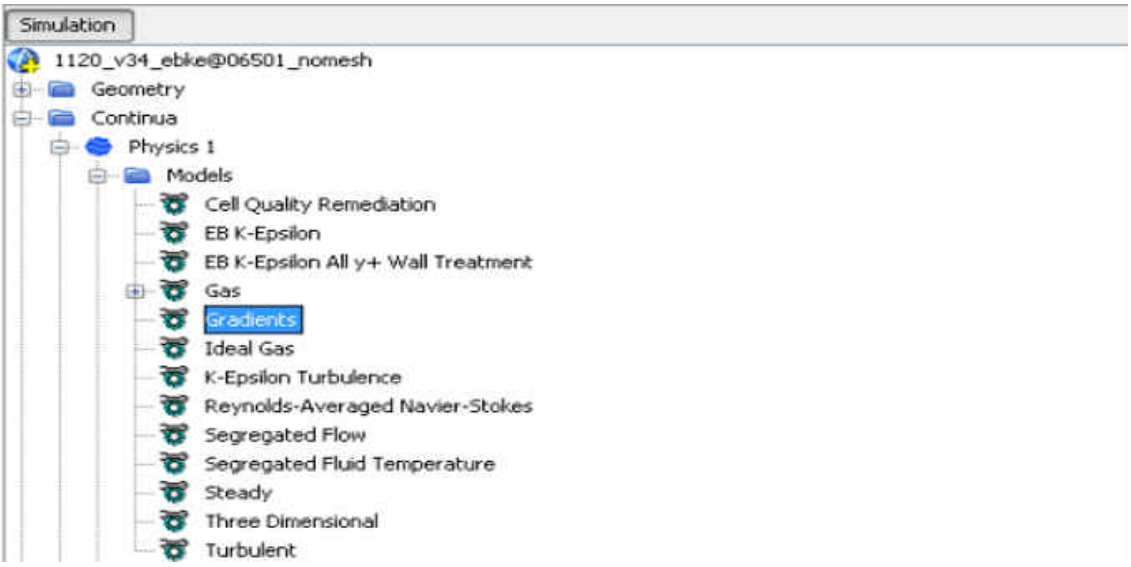

Figure 72: General tree line of the simulation

5.4.1 Gradients

The computation of gradients is a very import important aspect of the simulation, which allows for calculation of the data values at each cell with ensuring accuracy. Usually gradient computation plays a role within the transport equation solution methodology in reconstructing field values at the cell faces, secondary gradients of diffusion terms, pressure gradients for pressure-velocity coupling in the segregated flow model, and strain-rate and rotation-rate calculations for turbulence models. In this study, it was most vital to take care of the convection field values at faces, accounting for higher order diffusion terms, and pressure gradients.

Gradient computation can be specified as limited or unlimited within the STAR-CCM+ interface. Unlimited gradients do not prohibit the reconstructed field variables on the cell faces from exceeding the minimum and maximum values of the neighboring cells whereas limited methods does the reverse. In this simulation, limited gradient computation was implemented. Hybrid Gauss LSQ method was used to compute gradients and the Venkatakrishnan method was

implemented to limit them. These methods dictate how to calculate the gradients of different terms at cell centroids.

5.4.2 Hybrid LSQ Method

The unlimited gradient reconstruction was calculated at the cell-0 face by using following weighted least squares formula:

Equation 21: Weighted Least Squares Formula for Gradient Reconstruction

$$(\nabla\phi)_r^u = [\sum_f \frac{ds \otimes ds}{ds \bullet ds}]^{-1}[\sum_f \frac{\phi_0 - \phi_n}{ds \bullet ds}] \quad , \quad ds = x_0 - x_n \tag{21}$$

5.4.3 Ventkatakrishnan Limiter Method

The model uses the maximum and minimum values of the neighboring cells at which the reconstructing is being calculated and limits the gradient computation. The detailed calculation procedure is given below:

Minimum and maximum value calculations:

$$\phi_0^{\max} = \max(\phi_0, \phi_{neighbors}) \quad , \quad \phi_0^{\min} = \min(\phi_0, \phi_{neighbors})$$

These quantities can also be computed as:

$$\Delta_{\max} = \phi_0^{\max} - \phi_0 \quad , \quad \Delta_{\min} = \phi_0^{\min} - \phi$$

Each face *f* of cell-0 is defined as:

$$\Delta_f = \phi_{f,0} - \phi_0 = s_0 \cdot (\nabla\phi)_{r,0}^u$$

The limits are defined as:

$$r_f = \begin{cases} \dfrac{\Delta_f}{\Delta_{\max}} \; for \Delta_f > 0 \\ \dfrac{\Delta_f}{\Delta_{\min}} \; for \Delta_f \le 0 \end{cases}$$

Finally, the limiter equation is defined as:

$$\alpha_f = \frac{2r_f + 1}{r_f(2r_f + 1) + 1}$$

5.4.4 Segregated Flow

The Segregated Flow model solves the flow equations (one for each component of velocity, and one for pressure) in a segregated, or uncoupled, manner. The linkage between the momentum and continuity equations is achieved with a predictor-corrector approach.

Equation 22: Discretized Momentum

$$\frac{\partial}{\partial t}(\rho \aleph v V)_0 + \sum_f [v\rho(v - v_g) \cdot a]_f = -\sum_f [\rho \mathrm{I} \cdot a]_f + \sum_f \mathrm{T} \cdot a \tag{22}$$

Equation 23: Discretized Continuity

$$\sum_f \dot{m}_f = \sum_f (\dot{m}_f^* + \dot{m}_f') = 0 \tag{23}$$

Where the term denoted by * is computed after discretized momentum equations are solved. The term denoted with this is corrected mass flow rate and required to satisfy continuity.

Generally, this model has its roots in constant-density flows. Although it can handle mildly compressible flows and low Rayleigh number natural convection, it is not suitable for shock-capturing, high Mach number, and high Rayleigh-number applications.

5.4.5 Segregated Fluid Temperature

The Segregated Fluid Temperature model solves the total energy equation with temperature as the solved variable. Enthalpy is then computed from temperature according to the equation of state.

Equation 24: Total Energy

$$\frac{d}{dt}\int_V \rho E dV + \oint_A [\rho H(v - v_g) + v_g p] \cdot da = -\oint_A \dot{q}'' \cdot da + \oint_A \mathrm{T} \cdot v da + \int_V f \cdot v dV + \int_V s_u dV \tag{24}$$

Since there is no heat flux or heat source used, all of the related terms in the above equation will be cancelled to zero. Ideal gas enthalpy relationships will be used to determine required information.

5.4.6 Miscellaneous Models

Other models that were applied to this simulation, but have yet to be discussed are; steady sate, and three dimensional. The calculations performed during the simulation were independent of the time and were computed in 3D space.

5.4.7 Initial Conditions

Initial conditions were used to prevent the residual from rapidly increasing at the early iterations and to aid in smooth convergence. Figure 73 shows the initial condition node in the STAR-CCM+ simulation tree, where sub nodes indicate initial conditions which were specified.

An initial velocity of 24 m/s was specified in the streamwise direction, as linear ramps in place for changes in velocity and pressure with subsequent iteration ensures that the respective transport variable do not have exponential growth in residuals at early iterations. Similarly, many other ramps were implemented for the energy and turbulent solvers. The main purpose of the

ramps is to prevent large changes in the monitored variables (e.g. turbulent kinetic energy, temperature, etc.) between iterations.

For initial values in pressure and temperature, values very close to the steady value from experimental were used. This is justifiable as values of pressure and temperature in the wind tunnel (i.e. at the inlet, the freestream, in the plenum, etc.) should not change throughout each test cases ran or as the film cooling effectiveness develops with initialization of initial conditions.

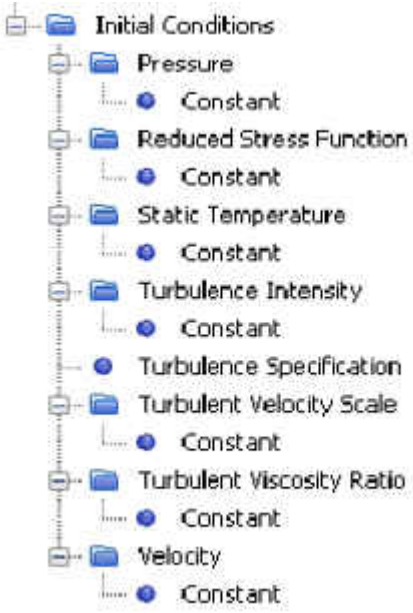

Figure 73: Initial Conditions listed in STAR-CCM+

5.5 Turbulence Models

The v2f variant of the traditional k-ε turbulence model is the primary turbulence model to be tested for this study. The need for modeling validation and comparison between other models compels the implementation of a secondary turbulence model; SST (Shear Stress Transport). The elliptic blending variant of the traditional k-ε turbulence model is also used as a third comparison, without serious investigation though however into the mechanics of the model. Both secondary

models, based on literature, are widely used schemes in both academia and industry. Further, primary validation will be provided by the available experimental data.

In any fluid flow problem whether the investigator aims at studying heat transfer or mass transfer, every solution finds its origin in the continuity, momentum and energy equations (presented here in 2-D form).

Equation 25: Continuity

$$\frac{\partial u}{\partial x}+\frac{\partial v}{\partial y}=0 \tag{25}$$

Equation 26: Momentum

$$u\frac{\partial u}{\partial x}+v\frac{\partial u}{\partial y}=-\frac{1}{\rho}\frac{\partial P}{\partial x}+\frac{\partial}{\partial y}\left(\upsilon\frac{\partial u}{\partial y}\right) \tag{26}$$

Equation 27: Energy

$$u\frac{\partial T}{\partial x}+v\frac{\partial T}{\partial y}=\frac{\partial}{\partial y}\left(\alpha\frac{\partial T}{\partial y}\right) \tag{27}$$

By applying the Reynolds decomposition, which separates any transport variable into its average and fluctuation components in conjunction with the concept of time averaging, the resulting equation of interest, namely the former Navier-Stokes equations, finds a new form. More specifically, this form expresses the transport variables in an average and fluctuating manner separately within the Reynolds Averaged Navier-Stokes (RANS) and average energy equations.

Equation 28: RANS

$$\bar{u}\frac{\partial \bar{u}}{\partial x}+\bar{v}\frac{\partial \bar{u}}{\partial y}=-\frac{1}{\rho}\frac{\partial \bar{P}}{\partial x}+\frac{\partial}{\partial y}\left(\upsilon\frac{\partial \bar{u}}{\partial y}-\overline{u'v'}\right) \tag{28}$$

Equation 29: Energy with RANS Decomposition

$$\bar{u}\frac{\partial \bar{T}}{\partial x}+\bar{v}\frac{\partial \bar{T}}{\partial y}=\frac{\partial}{\partial y}\left(\alpha\frac{\partial \bar{T}}{\partial y}-\overline{v'T'}\right) \tag{29}$$

A new term has appeared in each equation, the turbulent shear stress and the turbulent heat flux. Whereas all familiar terms can readily be evaluated and quantified, the equation cannot be solved now, since there are more unknowns than equations available, hence there is a closure problem. This type of issue can be tackled by modeling the additional terms and relating them to known quantities. By observing turbulent flow it is plausible that turbulent shear stress and normal turbulent heat flux would tend to zero if there were no mean velocity and mean temperature gradients (in the normal direction) hence the following formulation would be reasonable:

Equation 30: Reynolds Stress (Fluctuations in Momentum due to Turbulence)

$$-\overline{u'v'} \propto \frac{\partial \bar{u}}{\partial y} \tag{30}$$

Equation 31: Turbulent Heat Flux from RANS Decomposition

$$-\overline{T'v'} \propto \frac{\partial \bar{T}}{\partial y} \tag{31}$$

As a proportionality factor, the eddy diffusivity for momentum and heat transfer are included in the expressions:

Equation 32: Reynolds Stress Defined in Terms of Eddy Diffusivity

$$-\overline{u'v'} = \varepsilon_M \frac{\partial \bar{u}}{\partial y} \tag{32}$$

Equation 33: Turbulent Heat Flux from RANS Decomposition in Terms of Eddy Diffusivity

$$-\overline{v'T'} = \varepsilon_H \frac{\partial \bar{T}}{\partial y} \tag{33}$$

The final forms of the RANS equations hence take shape:

Equation 34: RANS with Eddy Diffusivity Incorporated

$$\bar{u}\frac{\partial \bar{u}}{\partial x} + \bar{v}\frac{\partial \bar{u}}{\partial y} = -\frac{1}{\rho}\frac{\partial \bar{P}}{\partial x} + \frac{\partial}{\partial y}\left((\upsilon + \varepsilon_M)\frac{\partial \bar{u}}{\partial y}\right) \tag{34}$$

Equation 35: Energy Equation with RANS Decomposition and Eddy Diffusivity Incorporated

$$\bar{u}\frac{\partial \bar{T}}{\partial x} + \bar{v}\frac{\partial \bar{T}}{\partial y} = \frac{\partial}{\partial y}\left((\alpha + \varepsilon_H)\frac{\partial \bar{T}}{\partial y}\right) \tag{35}$$

The first attempts at providing closure by modeling the eddy diffusivities exploited the concept of mixing length, which either discretized the boundary layer or fully described it through functions. More modern approaches bring closure by defining additional equations based on other transport variables characteristic of turbulent flow such as turbulent kinetic energy, turbulent

dissipation energy (ε), specific dissipation (ω) and similar quantities. These schemes are known are 2, 3 and 4 equations models.

Despite the tremendous amount of ingenuity put in these complex formulations, each model tends to target a specific flow region and successfully solves with sizable error only that region. As mentioned, it all depends on how the RANS turbulent features are modeled. The models chosen to solve and validate a jet in cross flow problem are particularly appropriate for near wall turbulence transport representation.

5.5.1 V2-f Variant of the Traditional K-ε Model

The traditional k- ε model suffers from strong free stream sensitivity and prediction ability in adverse pressure gradients. The k-ε model was specifically designed to tackle the issue of slow adjustment of the free-stream section of the boundary layer to changing boundary conditions that would otherwise lead the solver to under predict. This particular approach is particularly effective in free shear flow with small pressure gradients and mildly accelerating flows. It performs poorly in flow fields where large adverse pressure gradients drive the flow.

As before initially, eddy viscosity will now be defined:

Equation 36: Eddy Viscosity

$$\upsilon_t = C_\mu f \frac{k^2}{\varepsilon} \tag{36}$$

Equation 36 is based on turbulent kinetic energy and turbulent dissipation which are determined by the scales of turbulence. The turbulent transport equations take the following form:

Equation 37: Turbulent Transport Equation No. 1 for V2f

$$\frac{\partial}{\partial t}(\rho k)+\frac{\partial}{\partial x_i}(\rho k u_i)=\frac{\partial}{\partial x_j}\left(\left(\mu+\frac{\mu_t}{\sigma_{v^2}}\right)\frac{\partial k}{\partial x_j}\right)+P_k+P_b-\rho\varepsilon-Y_M+S_k \tag{37}$$

Equation 38: Turbulent Transport Equation No. 2 for V2f

$$\frac{\partial}{\partial t}(\rho \varepsilon)+\frac{\partial}{\partial x_i}(\rho \varepsilon u_i)=\frac{\partial}{\partial x_j}\left(\left(\mu+\frac{\mu_t}{\sigma_{v^2}}\right)\frac{\partial \varepsilon}{\partial x_j}\right)+C_{1\varepsilon}\frac{\varepsilon}{k}(P_k+C_{3\varepsilon}P_b)-C_{2\varepsilon}\rho\frac{\varepsilon^2}{k}+S_\varepsilon \tag{38}$$

Similarly to the k-ω models, we find the convective, turbulence production, dissipation terms and in addition there is a buoyancy term. The coefficients present mostly affect turbulence production and buoyancy effects in the dissipation transport equation.

The V2f variation of the k- ε model works well at low Reynolds numbers and near wall as it incorporates equations treating turbulence anisotropy, which typically causes model stiffness due to high non-linearity increasing computational inefficiency in the domain. The additional equations allow modeling the entire boundary layer from free stream all the way to the wall through the viscous sub-layer without the need for wall functions.

It models the eddy viscosity using the averaged squared velocity fluctuation normal to the streamlines, which provides the right scaling for the proper representation of turbulent transport damping near walls.

Equation 39: V2f Definition of Eddy Viscosity

$$\upsilon_t = C_\mu \overline{v^2} T \tag{39}$$

Anisotropic wall effects are then modeled by an elliptic relaxation function, f, embedded in an elliptic equation. In addition to the traditional k and ε, a transport equation for the new variable can be obtained in the following form where we have the typical form including convective, kinetic, dissipation and diffusion terms. Note that the effective viscosity expression remains intact:

Equation 40: Transport Equation No. 3 for V2f

$$\frac{\partial \overline{v^2}}{\partial t} + U_j \frac{\partial \overline{v^2}}{\partial x_j} = kf - \frac{\overline{v^2}}{k}\varepsilon + \frac{\partial}{\partial x_j}\left((\upsilon + \frac{\upsilon_t}{\sigma_{v^2}})\frac{\partial \overline{v^2}}{\partial y}\right) \tag{40}$$

and the elliptic equation for the relaxation function:

Equation 41: Elliptic Relaxation for 'f' in V2f Model

$$L^2 \nabla^2 f - f = \frac{C_1 - 1}{T}\left(\frac{\overline{v^2}}{k} - \frac{2}{3}\right) - C_2 \frac{P_k}{\varepsilon} \tag{41}$$

When defining the turbulent viscosity and deriving the transport equations, it is imperative to define the time scales and length scales which drive the degree of accuracy of the model. Note that the time scale directly affects the expression for the turbulent viscosity, which in turn defines the transport equations. Time and length scales are defined as:

Equation 42: Length Scale (V2f Specific)

$$L = C_L \max\left[\frac{k^{3/2}}{\varepsilon}, C_\eta\left(\frac{\upsilon^3}{\varepsilon}\right)^{1/4}\right] \tag{42}$$

Equation 43: Time Scale (V2f Specific)

$$T = \max\left[\frac{k}{\varepsilon}, C_T\left(\frac{\upsilon}{\varepsilon}\right)^{1/2}\right] \tag{43}$$

Keep in mind that these values for length and time are bounded by the Kolmogorov definitions, which mark the smallest turbulent element the model can track.

For modeling purposes these equations are implemented into finite differencing codes, which allow the user to manipulate the solver through the coefficients embedded in the transport equations. Note that these coefficients mainly handle the turbulence generating and the dissipation terms, this may generate more specific turbulence models appropriate to a particular flow field.

The coefficients used in the V2-f turbulence model are controlled from within the STAR-CCM+ user interface, and are up to the user to vary. The coefficients used are found below in Table 11.

Table 11: Coefficients used for the V2f turbulence model testing

Coefficients	
Cμ	0.09
C1,e	1.14
C2,e	1.9
Ct	6.0
σ,k	1.0
σ,e	1.3
A	0.045
C1	1.4
C2	0.3
Cl	0.23
Cμ,v2	0.22

5.5.2 SST Variant of the K-ω Model

The traditional k-ω model is a two-equation model that uses two transport variables, the turbulent kinetic energy and the specific dissipation, which provides turbulence scaling. Unlike the k-ε model it does not involve non-linear damping functions that require higher resolution near the wall in the order of $y^+<0.2$. Such low values result in radical computational inefficiencies. The lack of such functions allows to increase reduce the resolution by an order of magnitude to $y^+<2$.

Similarly to other models we start by expressing the eddy viscosity in the following way based on k and ω:

Equation 44: Eddy Viscosity (Specific to the K- ω Model)

$$\upsilon_t = \frac{k}{\omega} \tag{44}$$

Equation 45: Relationship of Specific Dissipation and Other Turbulent Transport variables

$$\omega = \frac{\varepsilon}{kC_{\mu}} \tag{45}$$

Following there are the fully derived transport equations for the k-ω model:

Equation 46: Transport Equations for the K-ω Model

$$\frac{\partial k}{\partial t} + U_j \frac{\partial k}{\partial x_j} = \tau_{ij} \frac{\partial U_i}{\partial x_j} - \beta^* k\omega + \frac{\partial}{\partial x_j}\left((\upsilon + \sigma^* \upsilon_T) \frac{\partial k}{\partial x_j} \right)$$

$$\frac{\partial \omega}{\partial t} + U_j \frac{\partial \omega}{\partial x_j} = \alpha \frac{\omega}{k} \tau_{ij} \frac{\partial U_i}{\partial x_j} - \beta \omega^2 + \frac{\partial}{\partial x_j}\left((\upsilon + \sigma \upsilon_T) \frac{\partial \omega}{\partial x_j} \right) \tag{46}$$

These equations include convective turbulence production, dissipation, and diffusion terms.

The SST variation of the traditional k-ω model is a widely used and very robust 2-equation eddy viscosity model in academia and in the industry capable of solving turbulent flow both near wall and in free stream. It combines the k-ε model and the k-ω model. The k-ω formulation allows for using the model in the inner regions of the boundary layer all the way to the wall, while the SST formulation can then switch to k-ε treatment in free stream to prevent enhanced k-ω sensitivity to inlet free stream boundary conditions, reducing model's stiffness. Due to this formulation the model can be directly applied without the use of any damping function near the wall.

This model tends to over predict in regions of large normal stress or strong acceleration, however theses effects are largely reduced compared to the traditional models. In addition it

provides good solutions in adverse pressure gradients and separating flow. In this case for jet in cross flow these qualities make this model appropriate for validation purposes.

Combining the k-ε and the k-ω models under the SST formulation, the transport equations turn out as:

Equation 47: Transport Equation No. 1 for the SST K- ω Model

$$\frac{\partial}{\partial t}(\rho k)+\frac{\partial}{\partial x_i}(\rho k u_i)=P-\beta^{*}\rho\omega k+\frac{\partial}{\partial x_j}\left((\mu+\sigma_k\mu_t)\frac{\partial k}{\partial x_j}\right) \tag{47}$$

Equation 48: Transport Equation No. 2 for the SST K- ω Model

$$\frac{\partial}{\partial t}(\rho\omega)+\frac{\partial}{\partial x_i}(\rho\omega u_i)=\frac{\gamma}{\upsilon_t}P-\beta\rho\omega^2+\frac{\partial}{\partial x_j}\left((\mu+\sigma_\omega\mu_t)\frac{\partial k}{\partial x_j}\right)+2(1-F_1)\frac{\rho\sigma_{\omega 1}}{\omega}\frac{\partial k}{\partial x_j}\frac{\partial \omega}{\partial x_j} \tag{48}$$

also known as the SST k-ω model as the two equations make use of the turbulent kinetic energy and specific dissipation transport variables. The eddy viscosity is expressed as:

Equation 49: Eddy Viscosity for the SST K- ω Model

$$\upsilon_t=\frac{a_1 k}{\max(a_1\omega,\Omega F_2)} \tag{49}$$

Through blending functions the model interpolates through the boundary layer all the way to the wall reducing the equations to the k-ω formulation.

The coefficients used in the SST k- ω turbulence model are controlled from within the STAR-CCM+ user interface, and are up to the user to vary. The coefficients used are found below in Table 12.

Table 12: Coefficients used for the SST K- ω turbulence model testing

Coefficients	
K	0.41
β*	0.09
β1	0.075
β2	0.0828
σ,k1	0.85
σ,w1	0.5
σ,k2	1.0
σ,w2	0.856
A1	0.31

5.6 Resources

The software of choice was Star-CCM+ 9.04.011, a powerful CFD tool capable of turbulence modeling and great flow visualization. In addition it has user friendly modes which allow the user to run each simulation in either serial or in parallel on servers with virtually limitless computing power for faster solving.

A total of 5 nodes were used for calculation, with 16 cpus per node. On a per cpu basis, there were 3.125 GB ram. This program served ideal for simulation as batch testing and monitoring of the solution was ideal through Star-CCM+ in Linux based operating systems.

5.7 Results and Discussion (FC.VI, M=1.0)

As discussed earlier, the main result for this study is the film cooling effectiveness, which speaks to the heat transfer occurring at the heat transfer surface based on the design tested. This

is a user defined field function within STAR-CCM+, based on the temperatures measured within the rig, as per the definition of effectiveness. When running the computation, the results for film cooling effectiveness in STAR-CCM+ are natively presented as contours over each specified section. This puts any specified scalar or vector to each cell, such that the user can toggle values through the domain. This works for qualitative comparison, but a more quantitative comparison is required, as seen throughout literature and industry practice. This derived result is called laterally averaged film cooling effectiveness.

The laterally averaged film cooling effectiveness is a means to turn a contour type plot of local effectiveness data into a two dimensional line plot. The horizontal axis of said plot is streamwise position, where each data point represents the effectiveness data averaged over the entire pitch. It should be noted that the lateral distance averaged at each streamwise location must be an integer of the pitch. This is such to ensure that the lateral average film cooling effectiveness accurately represents the effectiveness prediction over an infinite array.

The laterally averaged film cooling effectiveness is a derived quantity in STAR-CCM+. The film cooling effectiveness derived result is calculated by the user through creating a user defined field function, and then creating and running a java applet to average laterally at each streamwise location. It has the same physical meaning as effectiveness, it is just a means to concisely express the result.

As discussed earlier in this report, three turbulence models are tested in this study, all of which are compared against the experimental data acquired for the FC.VI case, for a blowing ratio of unity.

The first turbulence model which will be compared with experimental data is the V2f model, as seen in Figure 74. The V2f model possesses distinction from the standard k-ε models by

virtue of its accommodation for near-wall turbulence anisotropy and on-local pressure-strain effects, the results of which in this film cooling study are compared with V2f's performance seen otherwise in literature for film cooling application [25]. Kassab [25] demonstrated the tendency for the V2f turbulence model to over predict film cooling effectiveness by up to 17% in the region where the two fluid streams mix in the immediate vicinity of injection (X/D<4). This result seems consistent with the results, as local to the blowing ratios, where mixing of the two fluid streams is significant, the V2f model over predicts film cooling effectiveness. The V2f prediction of effectiveness is best predicted in the first ~200 diameters of the array, where thereafter a steady over prediction of heat transfer is predicted throughout the array. The general physical trend of the CFD data and experimental data match however, in that the effectiveness is low throughout the start of the array, then it is ramps up distinctly around 175 diameters, and therefore a very slight increase occurs with further streamwise position.

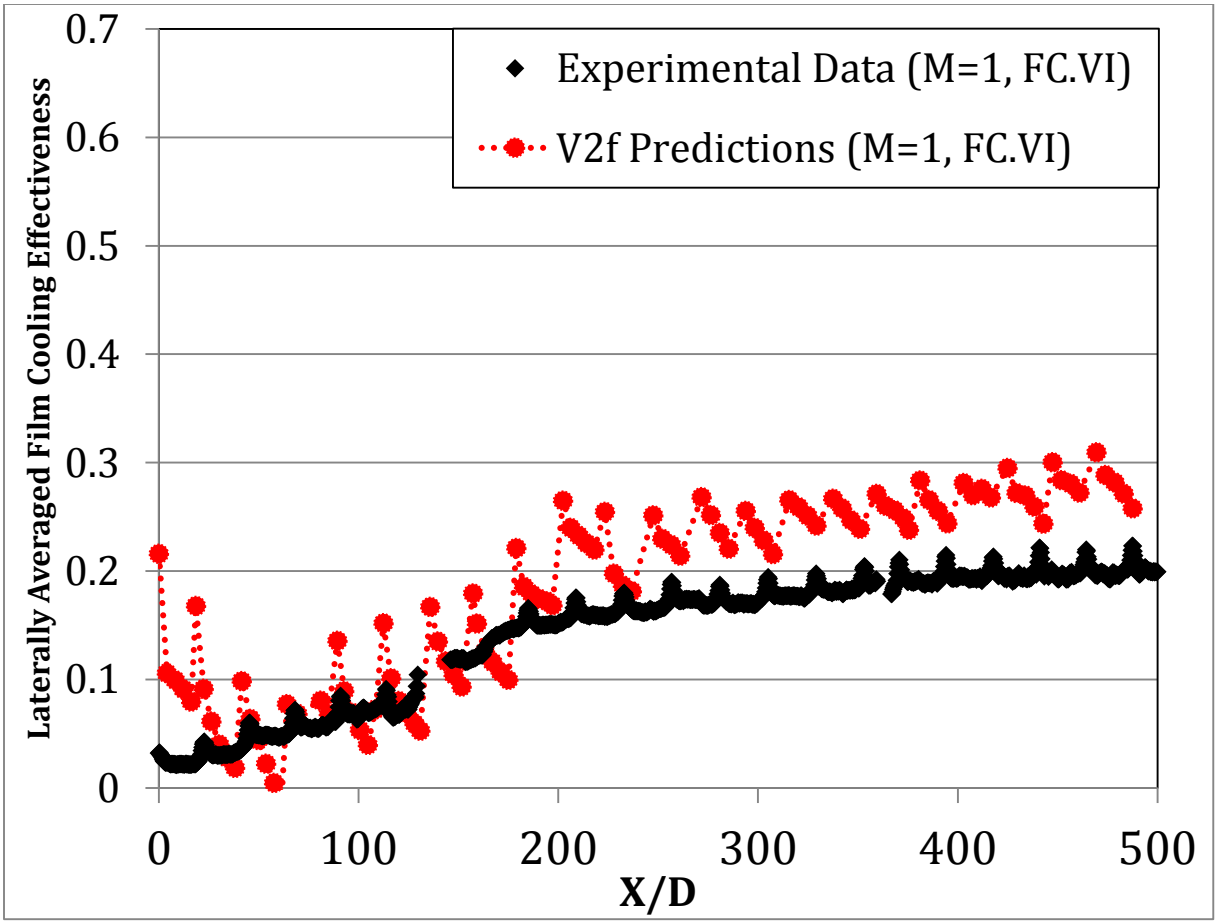

Figure 74: Comparison of experimental data and V2f CFD predictions (FC.VI, M=1)

The second turbulence model which will be compared with experimental data, is the SST model, as seen in Figure 75. Consistent with other computational studies [25], the SST CFD model performs marginally better than the V2f model in heat transfer predictions over the film cooled surface. The SST predictions for laterally averaged effectiveness are within experimental uncertainty at most streamwise positions, where especially good predictions are calculated concerning the highly turbulent flow field surrounding the beginning of the array. The nature of the SST model to blend the k-ω model and the k-ε model based on wall normal position proves ideal for heat transfer predictions throughout this film cooling array. Like the V2f results, the SST model also tends to over predict heat transfer downstream at the end of the array. Care should be

taken in CFD mesh design so that diffusion of scalars are not over predicted, resulting in cases that could resemble this over prediction of heat transfer presented here, although that source of error was mitigated in the mesh generated for this study.

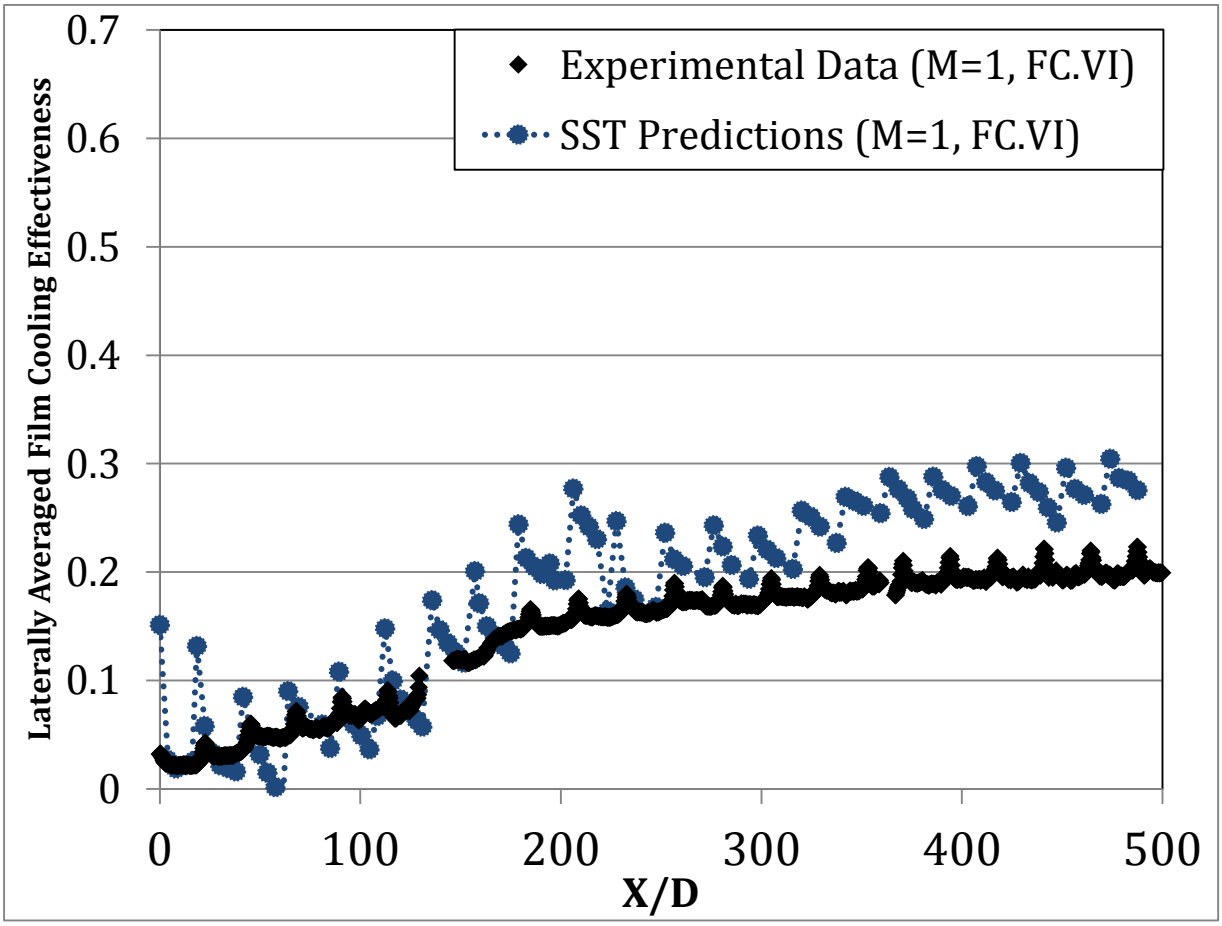

Figure 75: Comparison of experimental data and SST CFD predictions (FC.VI, M=1)

The third turbulence model which will be compared with experimental data, is the EBKE model, as seen in Figure 76. This model performs the worst amongst the three turbulence models utilized in CFD efforts. Heat transfer is marginally over predicted in the immediate vicinity of the start of the array relative to the SST and V2f model predictions, however the EBKE turbulence model severely over predicts heat transfer at downstream (~X/D>250) locations. This model is

not known for its triumphant success in film cooling applications, but is included in this test matrix due to its fundamental development based on the traditional k-ε turbulence model.

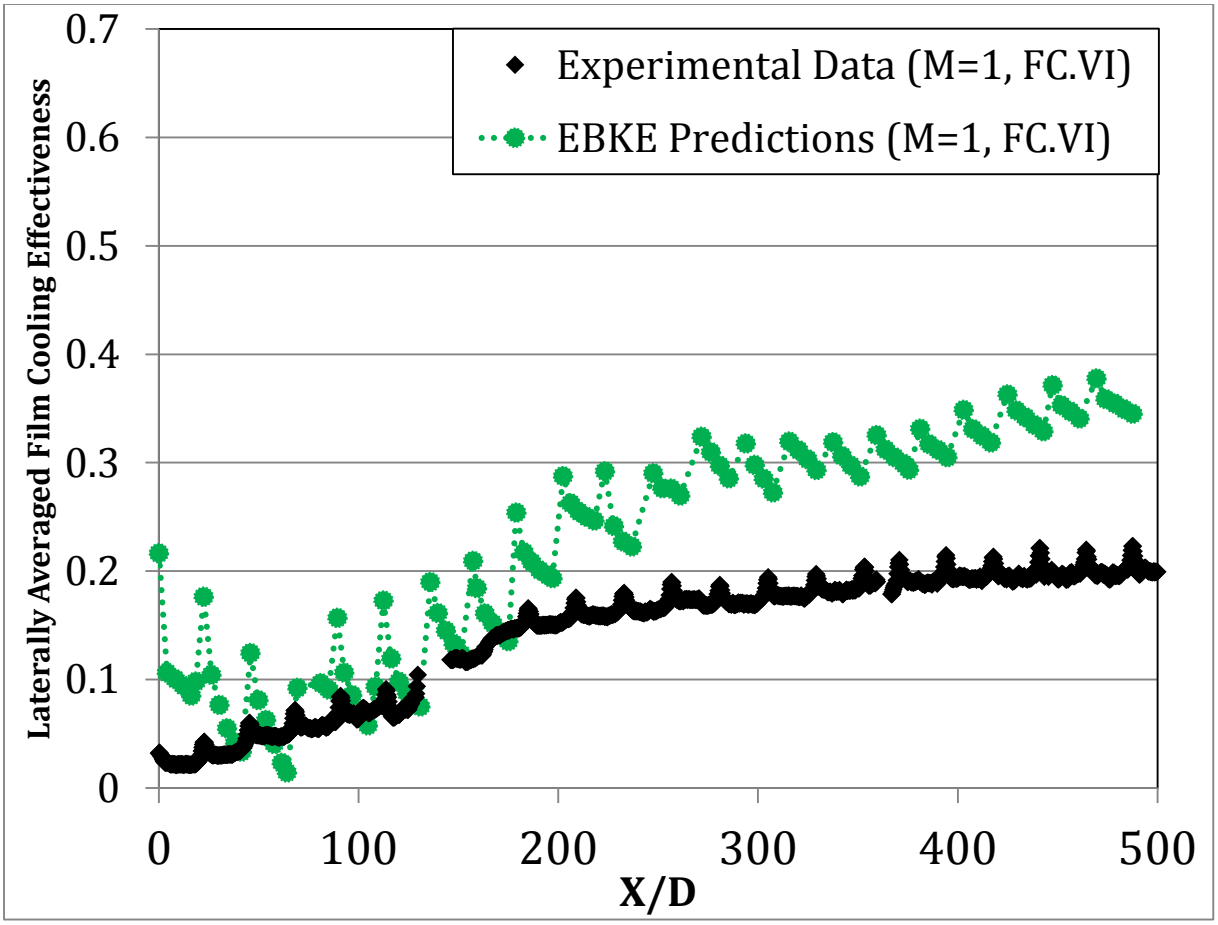

Figure 76: Comparison of experimental data and EBKE CFD predictions (FC.VI, M=1)

For a means of comparison, the resulting predictions in film cooling effectiveness by each turbulence model can be seen in Figure 77. As in Kassab [25], the SST model performs better than the V2f model by a slight margin, where both models are seen to over predict heat transfer. The SST model performs better than the V2f model most noticeably within the region of the end of the array, where the SST model handles the large mixing of the two fluid streams with better accuracy. The

general physical trend captured experimental is captured in all three CFD model predictions. All three turbulence model appear to over predict heat transfer downstream as well.

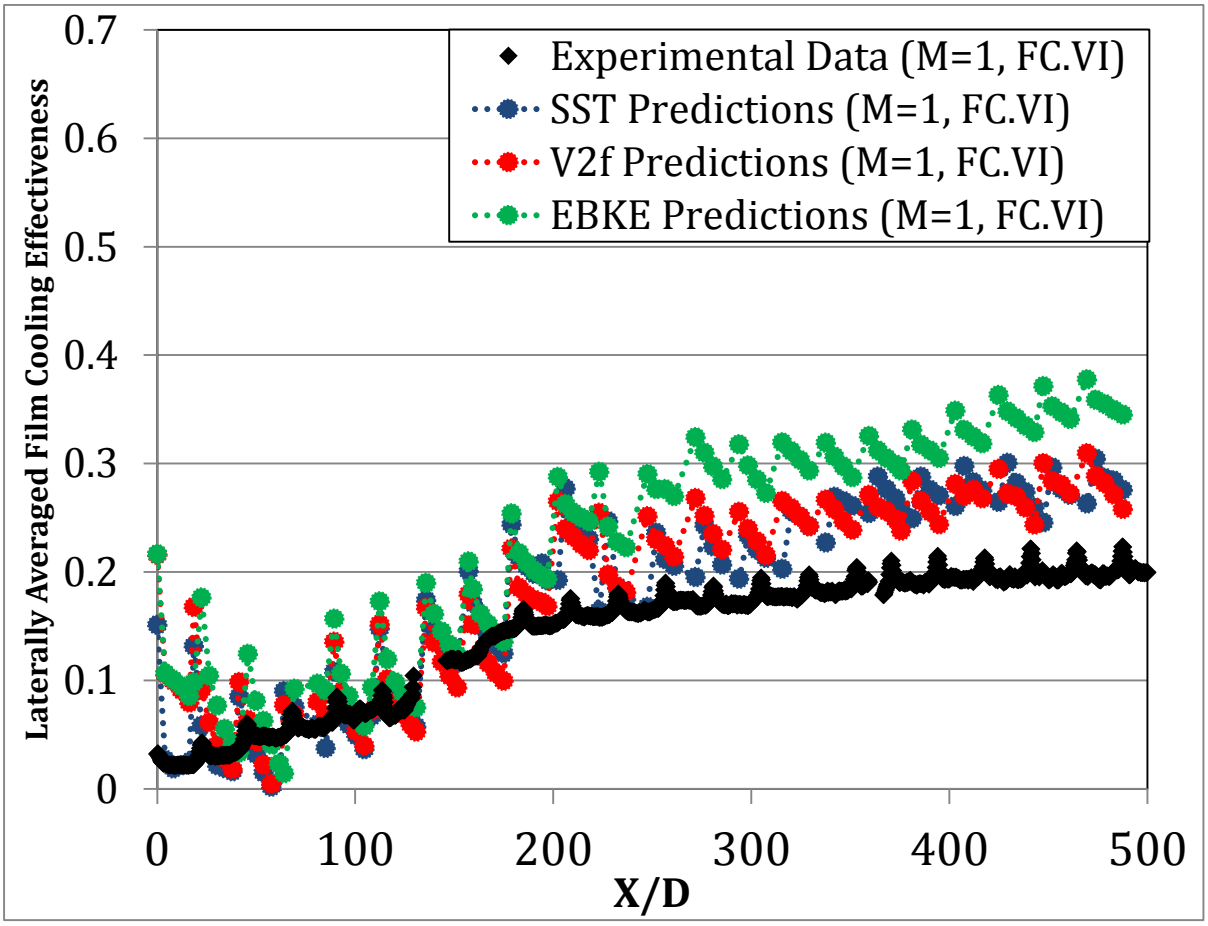

Figure 77: Comparison of 3 turbulence models performance with experimental data

The SST model is based on a combination and joining of the k-ω model and the k-ε model, and thus comparisons of its performance are made against the other two k- ε based models chosen. The distinct characteristics of each model provides non-straightforward conclusions about what features in a turbulence model prove most ideal for film cooling predictions. Some important differences between these turbulence models include, but are not limited to; the differing definitions of eddy viscosity, the use (or lack of) of relaxation functions amongst the transport

equations, wall functions, and adaptation/combination of models used based on wall normal position.

5.8 Convergence Results and Discussion

The last set of results to be shown here are in regards the convergence of the solution. The residual as per iteration can be seen plotted in Figure 78 for one test case which is similar and representative of the other simulations residuals. Residual plots will not presented for all of the simulations ran in this study. This residual type was relative, meaning the residual plotted with each subsequent iteration was relative to the beginning iterations.

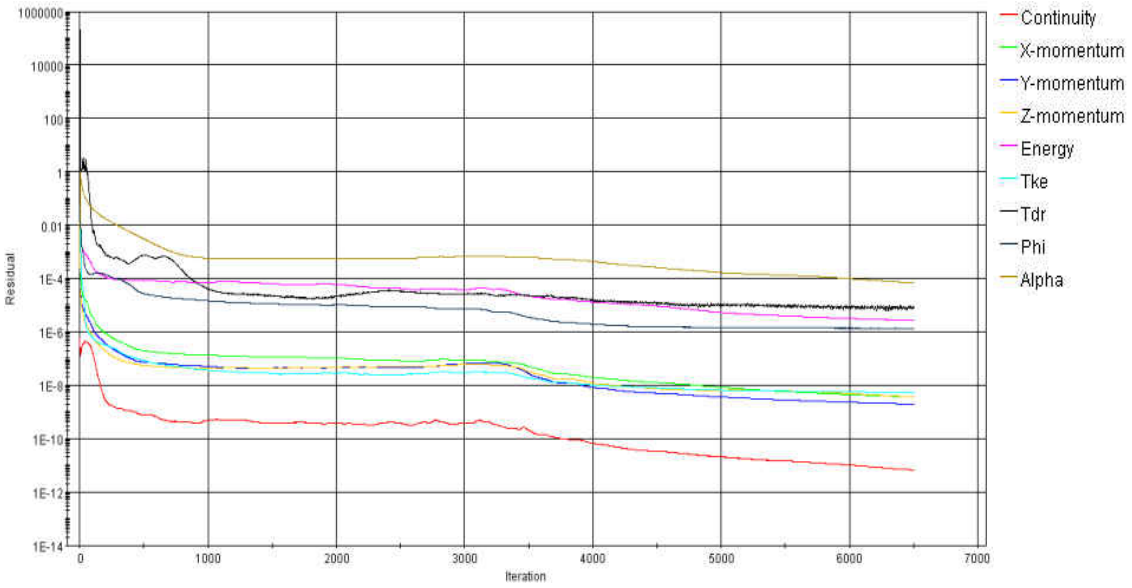

Figure 78: FC.II M=1.0 residual per iteration for the first 7k iterations in the simulation

A more aggressive way to decipher convergence is to track driving potentials in the problem, and ensure that they are steady with respect to further iterations. One example of this is the mass flow throughout the rig. One can track that the solution is no longer predicting any changes of

mass flow calculated at the rig exit, to ensure that this is a steady result. This was tracked at the inlet to the crossflow duct, the outlet to the cross flow duct, and the inlet to the film cooling holes. Plots are not shown here, as the solution quickly converged (after only about 1k iterations). Other variables were also tracked and similarly flat after 1k iterations, such as static temperature mass averaged at the outlet and inlet, static pressure at the inlet/outlet to the crowssflow duct, and also static pressure at the inlet to the film cooling holes. Without changes in these variables, the calculation is very unlikely to change at the heat transfer surface, with driving potentials such as pressure unchanging.

The last major means to justify convergence, was to average the entire static temperature on the heat transfer surface. This value was plotted with every iteration, and can be seen in Figure 34 for one particular simulation, indicative of such behavior present in other simulations. This value converged after about 6k iterations, where the last 500 to 1,000 iterations yielded only an approximate 1 degree change over the entire surface. This is substantially converged. Also, this result was done so in MATLAB on the experimental data, where the average static temperature was calculated over the experimental data images. The values were close between experimental and simulation.

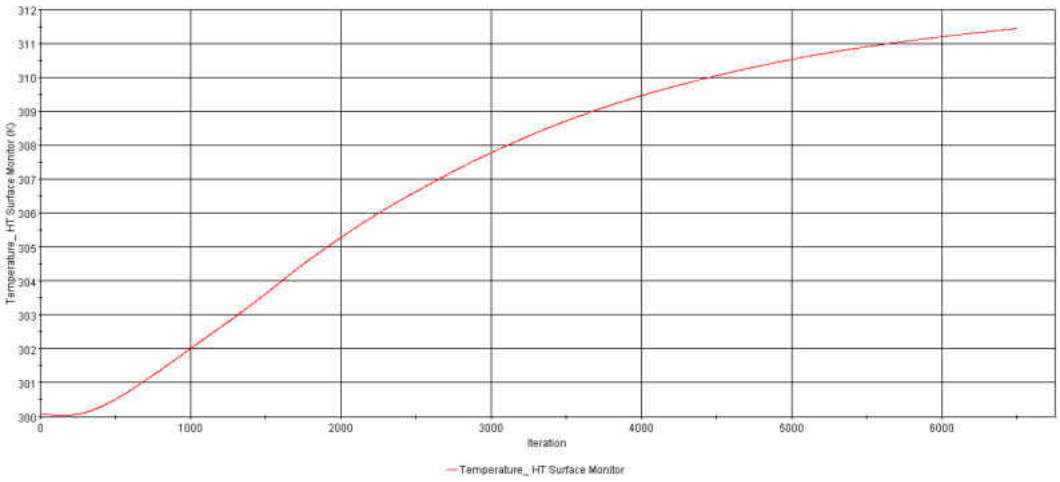

Figure 79: Average static temperature over the heat transfer surface as per iteration

CHAPTER 6: CONCLUDING REMARKS

The objective of this work is quantification of local heat transfer augmentation and adiabatic film cooling effectiveness for two full-coverage film cooling geometries with several operating condition variations. The geometries are distinct from one another by a compound angle shift in the film cooling holes, midway through the streamwise length of the array. Each of the geometries are tested for a range of blowing ratios between 0.5 and 2.0, corresponding to momentum flux ratios as large as 4.5.

Each array is composed of staggered cylindrical holes. The full-coverage array holes have a different hole orientation based on their position within the array (α=45° β=±45°), while the hole-to-hole spacing is significantly larger than often seen in literature (P/D=X/D=23). The effect of a compound angle shift is tested within the array; e.g., the holes are compounded in the positive lateral direction, then after twelve rows, the compounding angle changes sign to direct the coolant in the negative lateral direction.

6.1 Film Cooling Effectiveness

The full-coverage surfaces are composed of cylindrical holes, with and without varying alternating compound angles, tested with a negligible freestream acceleration, for adiabatic film cooling effectiveness. A low conductivity (k=0.029 W/m-K) material is used to imitate an adiabatic wall. Temperature sensitive paint yields local film recovery temperatures throughout the arrays of 24 rows. This spatially resolved data is then average laterally to yield an average film cooling effectiveness, such as that seen in Figure 80, which represents an infinitely wide array of film cooling. Figure 81 shows local data for FC.V, at the compound angle shift.

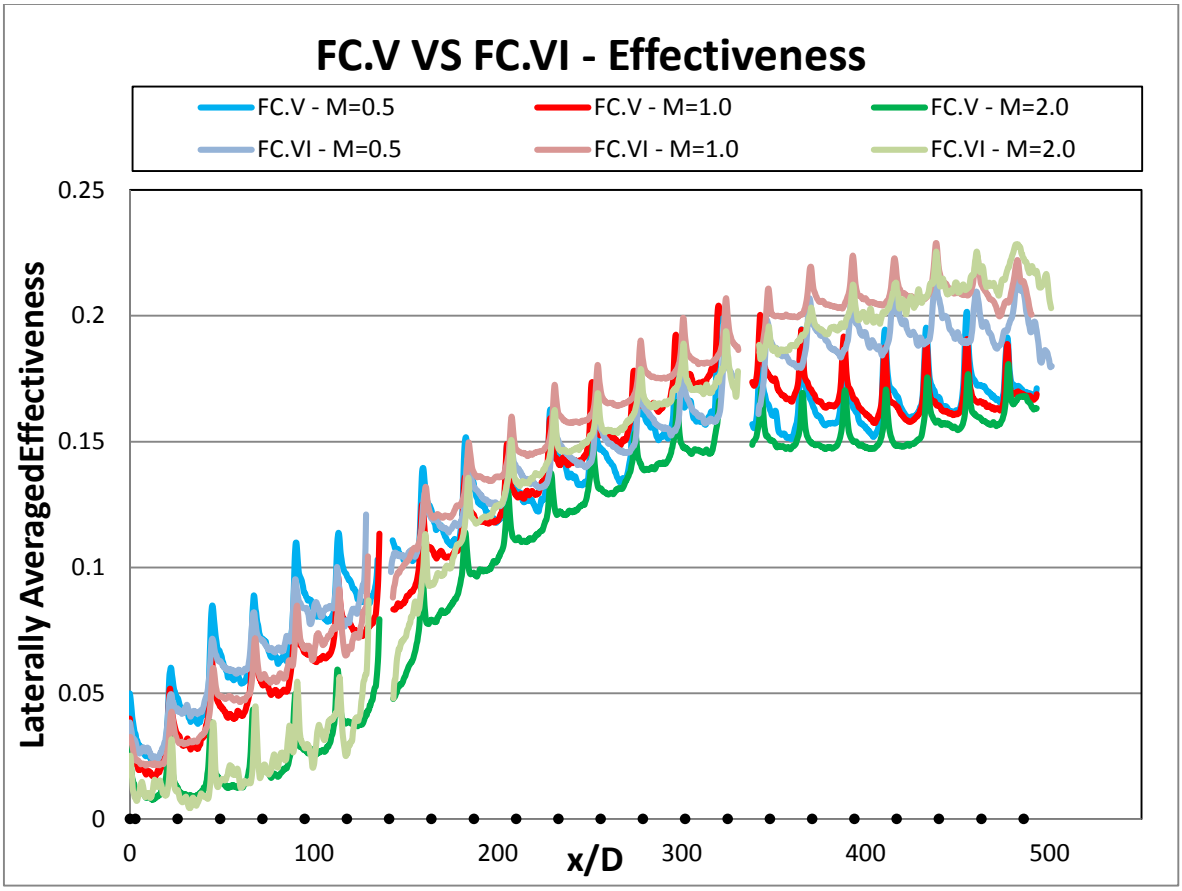

Figure 80: Comparison of laterally averaged effectiveness for several test cases at all blowing ratios

At these very large hole-to-hole spacings, the physics remain the same as has been reported and surveyed in literature. An increase in blowing ratio/momentum flux ratio causes the jets to lift from the surface at a critical momentum flux ratio, which is a function of hole geometry and hole orientation. Over these large streamwise distances tested, these lifted jets inevitably return to cool the wall.

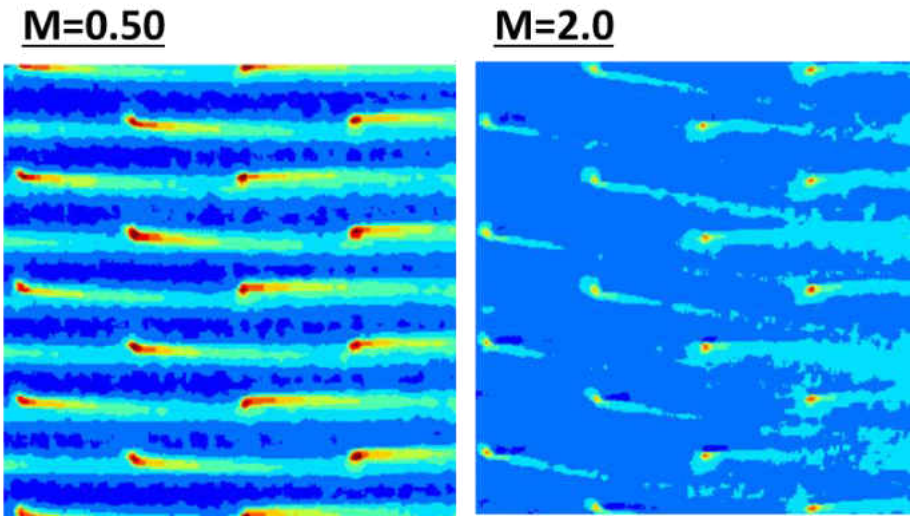

Figure 81: Local film cooling effectiveness at the compound angle shift for FC.V at the high and low blowing ratios

A novel effect studied presently is the effect of changing the compound angle after several rows. Literature has shown a benefit of such a shift, but for geometries composed of only two rows. For these full-coverage arrays it is clear that this compound angle shift has detrimental effects on cooling, and hence, should be avoided in designs if possible. It is this compound angle shift that causes the effectiveness curves in to decrease following x/D=300. Cases without this compound angle shift continue to rise in effectiveness throughout the entire array.

6.2 Heat Transfer Augmentation at Zero Pressure Gradient

Local and averaged heat transfer augmentation of the film cooling surfaces is also measured. Thin foil heaters are adhered to acrylic surfaces in order to impose a constant heat flux boundary condition for steady state measurement of heat transfer. TSP is used to obtain local temperature distribution of the heated surfaces. With heat loss corrections obtained experimentally, the heat transfer coefficient is then calculated. This heat transfer coefficient in the presence of film is then normalized by the heat transfer coefficient without film to yield an augmentation factor. The local heat transfer augmentation data is laterally averaged, then area averaged over a single pitch, which

compares area averaged heat transfer augmentation for each geometry. The area average is taken over a single pitch. A sample of this data can be seen in Figure 82.

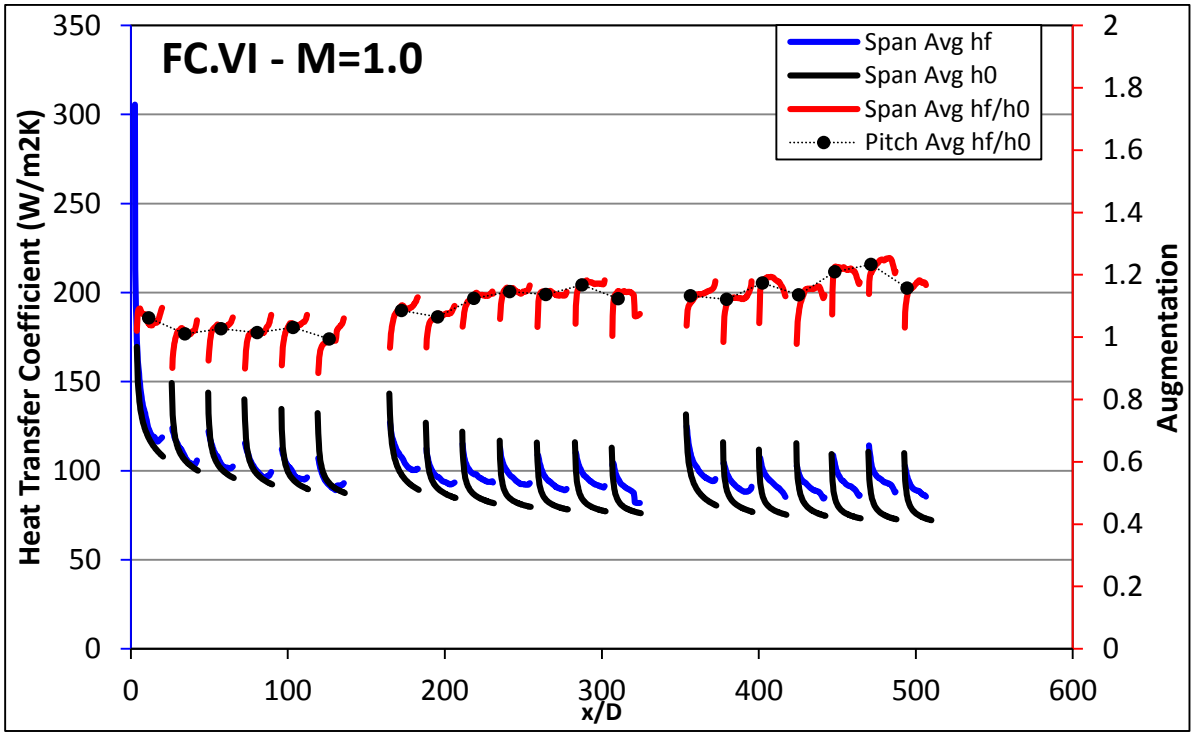

Figure 82: Heat transfer augmentation for FC.VI at M=1.0

LIST OF REFERENCES

[1] Newell, Richard, “Annual Energy Outlook 2011, Reference Case”, Energy Information Administration, December 16, 2011

[2] Boyce, Meherwan P. *Gas turbine engineering handbook*. Elsevier, 2012.

[3] Zuckerman, N., and N. Lior. "Jet impingement heat transfer: Physics, correlations, and numerical modeling." *Advances in heat transfer* 39.06 (2006): 565-631.

[4] Irvine, Thomas Francis. *Advances in heat transfer*. Vol. 23. Academic Press, 1993.

[5] Kohli, A., Bogard, D.G., 1998, “Fluctuating Thermal Field in the Near-Hole Region for Film Cooling Flows,” *J. Turbomach.*, 120, pp. 86-91.

[6] Aga, V., Rose, M., Abhari, R.S., 2008, “Experimental Flow Structure Investigation of Compound Angled Film Cooling,” *ASME J. Turbomach.*, 130, 031005 1-8

[7] Harrington, Mark K., et al. "Full-coverage film cooling with short normal injection holes." *ASME Turbo Expo 2001: Power for Land, Sea, and Air*. American Society of Mechanical Engineers, 2001.

[8] Butkiewicz, J., Walters, D., McGovern, K., and Leylek, J., 1995, “A Systematic Computational Methodology Applied to a Jet-in-Crossflow. Part 1: Structured Grid Approach,” ASME Paper No. 95-WA/HT-2.

[9] Kohli, A., and A. Thole. "A CFD INVESTIGATION ON THE EFFECTS OF ENTRANCE CROSSFLOW DIRECTIONS TO FILM-COOLING HOLES." (1997).

[10] Metzger, D. E., P. A. Kuenstler, and D. I. Takeuchi. "Heat transfer with film cooling within and downstream of one to four rows of normal injection holes."*Gas Turbine Conference and Products Show*. Vol. 1. 1976.

[11] Walters, D. K., and J. H. Leylek. "A detailed analysis of film-cooling physics: part I—streamwise injection with cylindrical holes." *Journal of turbomachinery*122.1 (2000): 102-112.

[12] Bunker, Ronald S. "A review of shaped hole turbine film-cooling technology."*Journal of heat transfer* 127.4 (2005): 441-453.

[13] McGovern, K. T., and J. H. Leylek. "A detailed analysis of film cooling physics: Part II—Compound-angle injection with cylindrical holes." *Journal of Turbomachinery* 122.1 (2000): 113-121.

[14] Lee, Hong-Wook, Jung Joon Park, and Joon Sik Lee. "Flow visualization and film cooling effectiveness measurements around shaped holes with compound angle orientations." International Journal of Heat and Mass Transfer 45.1 (2002): 145-156.

[15] Wright, L. M., Gao, Z., Varvel, T. A., and Han, J. C., 2005, “Assessment of Steady State PSP, TSP, and IR Measurement Techniques for Flat Plate Film Cooling,” ASME paper no. HT2005-72363

[16] R. J. Goldstein, \Film cooling," Advances in Heat Transfer, 1971.

[17] Mayle, R. E., and F. J. Camarata. "Multihole cooling film effectiveness and heat transfer." *Journal of Heat Transfer* 97.4 (1975): 534-538.

[18] Crawford, M. E., Kays, W. M., & Moffat, R. J. (1976). *Heat Transfer to a Full-Coverage Film-Cooled Surface with 30degree Slant-Hole Injection.* NASA CR-2786.

[19] Crawford, M. E., W. M. Kays, and R. J. Moffat. "Full-Coverage Film Cooling—Part I: Comparison of Heat Transfer Data for Three Injection Angles." *Journal of Engineering for Gas Turbines and Power* 102.4 (1980): 1000-1005.

[20] Kelly, Grady B., and David G. Bogard. "An investigation of the heat transfer for full coverage film cooling." *ASME Turbo Expo 2003, collocated with the 2003 International Joint Power Generation Conference*. American Society of Mechanical Engineers, 2003.

[21] Sasaki, M., et al. "Film cooling effectiveness for injection from multirow holes."*Journal of Engineering for Gas Turbines and Power* 101.1 (1979): 101-108.

[22] Al-Hamadi, A. K., B. A. Jubran, and G. Theodoridis. "Turbulence intensity effects on film cooling and heat transfer from compound angle holes with particular application to gas turbine blades." Energy conversion and management 39.14 (1998): 1449-1457.

[23] Ahn, Joon, In Sung Jung, and Joon Sik Lee. "Film cooling from two rows of holes with opposite orientation angles: injectant behavior and adiabatic film cooling effectiveness." *International Journal of Heat and Fluid Flow* 24.1 (2003): 91-99.

[24] Lutum, E., et al. Film cooling on a concave surface: influence of external pressure gradient on film cooling performance. ALSTOM IM SEGELHOF (SWITZERLAND), 2003.

[25] Silieti, Mahmood, Alain J. Kassab, and Eduardo Divo. "Film cooling effectiveness: Comparison of adiabatic and conjugate heat transfer CFD models." International Journal of Thermal Sciences 48.12 (2009): 2237-2248.

[26] Thurman, Douglas R., et al. "Turbulence and Heat Transfer Measurements in an Inclined Large Scale Film Cooling Array: Part II—Temperature and Heat Transfer Measurements." *ASME 2011 Turbo Expo: Turbine Technical Conference and Exposition*. American Society of Mechanical Engineers, 2011.

[27] Maiteh, B. Y., and B. A. Jubran. "Influence of mainstream flow history on film cooling and heat transfer from two rows of simple and compound angle holes in combination." International journal of heat and fluid flow 20.2 (1999): 158-165.

[28] Maiteh, B. Y., and B. A. Jubran. "Effects of pressure gradient on film cooling effectiveness from two rows of simple and compound angle holes in combination." Energy Conversion and Management 45.9 (2004): 1457-1469.

[29] Jessen, Wilhelm, Martin Konopka, and Wolfgang Schroeder. "Particle-Image Velocimetry Measurements of Film Cooling in an Adverse Pressure Gradient Flow." *Journal of Turbomachinery* 134.2 (2012): 021025.

[30] Keller, M., and M. J. Kloker. "Influence of boundary-layer turbulence on effusion cooling at Mach 2.67." Sonderforschungsbereich/Transregio: 1-13.

[31] J. Guo, P. Y. Julienn, and R. N. Meroney, \A modi_ed log-wake law for zero-pressure-gradient turbulent boundary layers," Journal of Hydraulic Research, 2005.

[32] Chu, C. H. (1977). Electrical Resistivity and Thermal Conductivity of nine selected AISI Stainless Steels.

[33] Mayle, M. E., & Camarata, F. J. (1975). Multihole Cooling Film Effectiveness and Heat Transfer. ASME Journal of Heat Transfer.

[34] Metzger, D. E., Kuenstler, P. A., & Takeuchi, D. I. (1976). Heat Transfer with Film Cooling within and Downstream of One to Four Rows of Normal Injection Holes. *ASME Turbo Expo*, (pp. 76-GT-83).

[35] Metzger, D. E., Takeuchi, D. I., & Kuenstler, P. A. (1973). Effectiveness and Heat Transfer with Full-Coverage Film Cooling. *Journal of Engineering for Power*, 180-184.

[36] Zhong, Fengquan, and Garry L. Brown. "A 3-dimensional, coupled, DNS, heat transfer model and solution for multi-hole cooling." *International journal of heat and mass transfer* 50.7 (2007): 1328-1343.

[37] Kasagi, N., Hirata, M., & Kumada, M. (1981). Studies of Full-Coverage Film Cooling Part1: Cooling Effectiveness of Thermally Conductive Wall. *ASME Turbo Expo*, (pp. 81-GT-37).

[38] Kumada, M., M. Hirata, and N. Kasagi. "Studies of full-coverage film cooling part 2: measurement of local heat transfer coefficient." *ASME Paper* 81-GT (1981): 38.

[39] Le Grives, E., Nocolas, J. J., & Genot, J. (1979). Internal Aerodynamics and Heat Transfer Problems Associated to Film Cooling of Gas Turbines. *ASME Turbo Expo*, (pp. 79-GT-57).

[40] Martiny, M., Schulz, A., & Wittig, S. (1995). Full-Coverage Film Coolin gInvestigation: Adiabatic Wall Temperatures and Flow Visualization. (pp. 95-WA/HT-4). ASME.

[41] Ling, J. P., Ireland, P. T., & Turner, L. (2002). Full Coverage Film Cooling for Combustor Transition Sections. *ASME Turbo Expo*, (pp. 2002-GT-30528).

[42] Harrington, M. K., McWaters, M. A., Bogard, D. G., Lemmon, C. A., & Thole, K. A. (2001). Full-Coverage Film Cooling with Short Normal Injection Holes. *ASME Turbo Expo*, (pp. GT2001-0130).

[43] Cho, H. H., & Goldstein, R. J. (1995). Heat (Mass) Transfer and Film Cooling Effectiveness with Injection Through Discrete Holes: PartII - On the Exposed Surface. *Journal of Turbomachinery*, 451-460.

[44] Cho, H. H., & Goldstein, R. J. (1997). Total Coverage Discrete Hole Wall Cooling. *Journal of Turbomachinery*, 320-329.

[45] Crawford, M. E., Kays, W. M., & Moffat, R. J. (1980). Full-Coverage Film Cooling Part II: Heat Transfer Data and Numerical Simulation. *Journal of Engineering for Power*, 1006-1012.

[46] Sasaki, M., Takahara, K., Kumagai, T., & Hamano, M. (1979). Film Cooling Effectiveness for Injection from Multirow Holes. *Journal of Engineering for Power, 101*, 101-108.

[47] Andrews, G. E., Khalifa, I. M., Asere, A. A., & Bazdidi-Tehrani, F. (1995). Full Coverage Effusion Film Cooling with Inclined Holes. *ASME Turbo Expo*, (pp. ASME95-GT-274).

[48] Fric, T. F., and A. Roshko. "Vortical structure in the wake of a transverse jet." Journal of Fluid Mechanics 279 (1994): 1-47.

[49] Claretti, Roberto, et al. "Experimental Evaluation of Large Spacing Compound Angle Full Coverage Film Cooling Arrays: Heat Transfer Augmentation." *ASME 2012 Heat Transfer Summer Conference collocated with the ASME 2012 Fluids Engineering Division Summer Meeting and the ASME 2012 10th International Conference on Nanochannels, Microchannels, and Minichannels*. American Society of Mechanical Engineers, 2012.

[50] Natsui, Greg, et al. "Experimental Evaluation of Large Spacing Compound Angle Full Coverage Film Cooling Arrays: Adiabatic Film-Cooling Effectiveness." *ASME 2012 Heat Transfer Summer Conference collocated with the ASME 2012 Fluids Engineering Division Summer Meeting and the ASME 2012 10th International Conference on Nanochannels, Microchannels, and Minichannels*. American Society of Mechanical Engineers, 2012.